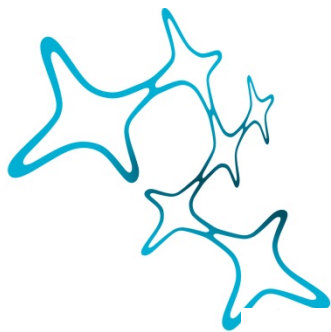
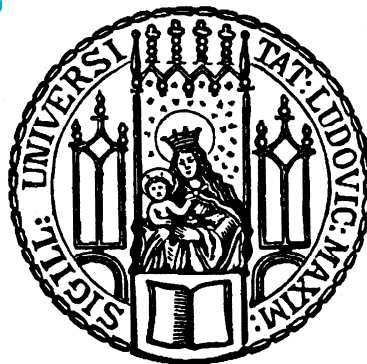

**SPINE DYNAMICS AND CIRCUIT
CONNECTIVITY OF TRANSCALLOSAL
NEURONS IN THE INTACT
CONTRALESIONAL CORTEX AFTER
TRAUMATIC BRAIN INJURY**

Laura Amalia Dorothea Alexandra Empl



Graduate School of
Systemic Neurosciences

LMU Munich



Dissertation der
Graduate School of Systemic Neurosciences der
Ludwig-Maximilians-Universität München

- April 2020 -

Supervisor:

PD Dr. Florence Bareyre

Biomedical Center

Institute of Clinical Neuroimmunology

Ludwig-Maximilians-Universität München

First Reviewer: PD Dr. Florence Bareyre

Second Reviewer: Prof. Dr. Martin Kerschensteiner

External Reviewer: Dr. Radhika Puttagunta

Date of Submission: 19.04.2020

Date of Defense: 24.07.2020

Parts of the present thesis have been published previously in the following peer-reviewed scientific journal:

Chovsepian A.*, Empl L.*, Correa D. and Bareyre F.M.: Heterotopic transcallosal projections are present throughout the mouse cortex. *Front Cell Neurosci*; 11:36, (2017)

(*These authors have contributed equally to this work.)

Therefore parts of this dissertation have been based on and cited from the above publication.

- Table of contents -

LIST OF ABBREVIATIONS	1
ABSTRACT	4
INTRODUCTION	5
1.1 Traumatic brain injury.....	5
1.1.1 Definition & epidemiology.....	5
1.1.2. Pathophysiology of TBI.....	6
1.1.3. Therapy and treatment options for TBI	8
1.2. Modelling traumatic brain injury- The controlled cortical impact model	10
1.3. Dendritic spines: From their structure to being the gateway of synaptic connections	12
1.4. Transcallosal neurons and their corticospinal counterparts:.....	16
1.4.1. Transcallsoal neurons.....	16
1.4.2. Corticospinal tract neurons	19
1.5. How does the brain react to injury? Recovery, remodelling and reorganization after injury- the current state of research	20
1.5.1. The intact parts of the lesioned hemisphere & recovery	21
1.5.2. Effects of TBI in the contralateral intact cortex & recovery.....	22
1.6. Principles of two-photon microscopy and its advantages	25
1.7. Tracing neurons in the brain.....	29
1.7.1. Neuroanatomical tracing using fluorescent dyes and markers	29
1.7.2. Viral tracing techniques	30
1.7.2.1. Adeno-associated viruses	30
1.7.2.2. Mono-synaptic rabies virus tracing techniques for neuronal circuit reconstruction	31
1.8. Aims of this thesis.....	34
MATERIALS & METHODS	36
2.1. Tables of materials and methods.....	36
2.1.1. Disposable materials & tools.....	36
2.1.2. Reagents & chemicals	38
2.1.3. Tracers, viruses, antibodies	39
2.1.4. Medication	39
2.1.5. Technical & imaging devices	40
2.1.6. Software.....	41
2.2. Animals	41
2.3. Surgical procedures – General considerations	43

2.4. Injury paradigm- controlled cortical impact.....	43
2.5. Viral & tracer injections	45
2.5.1 Characterization of transcallosal neurons in the intact mouse brain.....	45
2.5.2. In vivo investigation of transcallosal neurons in the non-injured contralesional cortical hemisphere.....	45
2.5.3. Circuit connectivity of TCN after TBI.....	46
2.6. Chronic cranial window implantation.....	49
2.7. Tissue preparation	51
2.7.1. Characterization of transcallosal neurons in the intact mouse brain.....	51
2.7.2. Determining comparable lesion outcome and volume after controlled cortical impact.....	52
2.7.3. Circuit connectivity of transcallosal neurons after traumatic brain injury.....	52
2.8. Image acquisition and image processing	52
2.8.1 Distribution of transcallosal neurons throughout the mouse cortex.....	52
2.8.2. Characterization of injury outcome after controlled cortical impact.....	53
2.8.3. Investigation of spine dynamics in TCN, CST neurons and a general neuronal population, using in vivo two-photon microscopy.....	53
2.8.4. Circuit connectivity of transcallosal neurons after traumatic brain injury - Starter cells.....	54
2.8.5. Circuit connectivity of neurons after traumatic brain injury - Pre-synaptic cells.....	54
2.9. Data analysis	55
2.9.1. Distribution of transcallosal neurons throughout the mouse cortex.....	55
2.9.2. Analysis of in vivo spine dynamics and counting criteria	56
2.9.3. Circuit connectivity of transcallosal neurons after traumatic brain injury - Starter cell quantification.....	58
2.9.4. Circuit connectivity of transcallosal neurons after traumatic brain injury - Pre-synaptic cell quantification.	59
2.10. Statistical Evaluation	60
RESULTS	61
3.1. Descriptive study of transcallosal neurons in the mouse cortex.	61
3.1.1 Anterograde labelling reveals homotopic and layer-specific organisation of axonal projections of TCN in the contralateral cortex	61
3.1.2 Retrograde labelling of TCN uncovers a comparable homotopic and layer-specific organisation in different cortical areas.....	62
3.2. Determination of lesion volume of our injury parameters by CCI.....	67

3.3. In-vivo imaging and analysis of spine dynamics after TBI in the non-injured contralateral somatosensory cortex.....	67
3.3.1. Observations based on a population level using GFP-M mice.....	68
3.3.2. Observations based on TCN and CST neurons selectively labeled by retrograde viral tracing	72
3.3.2.1. In-depth look into the spine dynamics of contralesional TCN after TBI	74
3.3.2.2. In-depth look at spine dynamics of CST neurons after TBI	78
3.3.3. TCN and CST are inherently different in their spine dynamics	81
3.3.4. Survival and persistence of spines in TCN and CST neurons after injury.....	83
3.4. Alterations of the circuit structure and organization in the non-injured cortex after TBI.....	86
3.4.1. Proof of concept: Mono-synaptic tracing of circuit connectivity with modified-rabies and cre-dependent targeting of TCN.....	87
3.4.2. Starter cell quantification	89
3.4.3. Pre-synaptic cell mapping.....	90
3.4.3.1 Number of starter cells and pre-synaptic cells are correlated	90
3.4.3.2 Connectivity ratio of TCN after injury - Layer and time-point specific changes are detectable	91
DISCUSSION	95
4.1. Descriptive study of the distribution and location of TCN in the intact mouse cortex.....	95
4.1.1. Anterograde tracing of TCN projection patterns.....	95
4.1.2. Retrograde labelling of TCN cell bodies in the intact mouse cortex.....	96
4.2. In-vivo imaging of spine dynamics after TBI in the contralesional intact somatosensory cortex	97
4.2.1. Spine dynamics after TBI in a mixed non-specific neuronal population.....	97
4.2.2. Spine dynamics after TBI in a specific population of TCN and CST neurons	100
4.3. The effects of TBI on intact contralesional TCN network organization.....	107
CONCLUDING REMARKS	111
5.1 Descriptive study of transcallosal neurons in the intact mouse cortex	111
5.2 Spine dynamics and circuit connectivity of the contralesional intact somatosensory cortex after TBI	111
REFERENCES	114
ACKNOWLEDGMENTS.....	128

LIST OF PUBLICATIONS130
EIDESSTÄTTLICHE VERSICHERUNG/AFFIDAVIT132
DECLARATION OF AUTHOR & RESULTS CONTRIBUTIONS133

- LIST OF ABBREVIATIONS -

AAV	Adeno-associated virus
AAV-cre	cre-expressing adeno-associated virus
AAVrg	Retrograde adeno-associated virus
AAV-TVA-G-eGFP	AAV1-synP-DIO-sTpEpB-eGFP
ACA	Anterior cingulate area
AMPA	α -amino-3-hydroxy-5-methyl-4-isoxazolepropionic acid
Amyg	Amygdala
ANOVA	Analysis of variance
ASLV-A	Avian sarcoma/leukosis virus subtype A
AUD	Auditory area
B1	Baseline 1 (first imaging session before injury)
B2	Baseline 2 (second imaging session before injury)
BBB	Blood-brain barrier
BDA	Biotinylated dextran amine
CC	Corpus callosum
CCI	Controlled cortical impact model
CLA	Clastrum
CNS	Central nervous system
CP	Caudate putamen
CST	Corticospinal tract
CTB	Choleratoxin beta subunit b
CTRLS	Control animals
CW	Cranial Window
cCAMP	Cyclic adenosine monophosphate
DAI	Diffuse Axonal Injury
dpi	Days post injury

EGFP	Enhanced green fluorescent protein
ENT	Entorhinal area
EnvA	Avian envelope protein
EPO	Erythropoietin
FG	Fluorogold
FGF2	Basic fibroblast growth factor
fMRI	Functional magnetic resonance imaging
GABA	Gamma-Aminobutyric acid
GCS	Glasgow Coma Scale
GFP	Green fluorescent protein
G-protein	Glycoprotein
HA	Homotopic area
Hypo	Hypothalamus
IC	Internal capsule
ICP	Intracranial pressure
I.p.	Intraperitoneal
IHC	Immunohistochemistry
LAA	Lateral adjacent area
MAA	Medial adjacent area
MCAO	Middle cerebral artery occlusion
MMF	Midazolam, Medetomidin, Fentanyl (Anaesthetic)
MO	Somatomotor area
NBD	Diagonal Band Nucleus
NGF	Nerve growth factor
NMDA	N-methyl-D-aspartate
NT	Neurotrace
Pall	Pallidum
PB	Phosphate buffer

PBS	Phosphate Buffered Saline
PER	Perirhinal area
PFA	Paraformaldehyde
PI	Persistence index
PSD	Post-synaptic density
PTL	Posterior parietal association area
ROI	Region of interest
RM	Repeated measures
RSP	Restrosplenial area
SS	Somatosensory area
SEM	Standard error of the mean
SF	Survival fraction
TBI	Traumatic brain injury
TCN	Transcallosal neurons
TEA	Temporal association area
Thal	Thalamus
TOR	Turnover rate
ViscA	Visceral area
VEGF	Vascular endothelial growth factor
VIS	Visual area
YFP	Yellow fluorescent protein

- ABSTRACT -

Traumatic brain injury (TBI) results in a cascade of pathological mechanisms that ultimately transcend into long-term cognitive, neurological, motor and emotional deficits. It has recently been observed that the brain has a remarkable ability to functionally recover from injuries, especially by recruiting the contralesional intact hemisphere. The inner workings of these processes are still not understood. This dissertation investigates the *in vivo* response of transcallosal neurons (TCN) residing in the contralesional intact hemisphere and their potential for structural spine plasticity after TBI, which may play a role in a mechanism of compensatory recovery after injury. TCN are especially interesting because they are anatomically connected to both the injured and intact hemisphere after TBI.

First, a thorough characterization of TCN distribution, via anterograde and retrograde tracing approaches, throughout different areas of the cortex laid the groundwork to better understand TCN as a neuronal subpopulation. In that respect this work demonstrated that TCN are predominantly distributed in a uniform and layer-specific fashion and broadly project to the contralateral cortical column homotopically. Secondly, using *in vivo* two-photon imaging techniques, the results of this thesis showed that a mixed population of neurons in deeper layers of the contralesional intact hemisphere undergo structural changes and experience an early decrease of spine density following TBI. The same effect of TBI on spine density was visible specifically for TCN in upper layers of the intact contralesional cortex, but only at much later stages after injury. Finally, and with the help of a mono-synaptic rabies virus tracing technique, this thesis also showed changes in pre-synaptic circuit connectivity of TCN after TBI. While pre-synaptic partners to TCN were lost late after TBI in some brain areas, other regions were able to recuperate an initial and early loss of connectivity at 42 days post injury. This recovery was thought to be established by re-connecting to neuronal partners within their initial circuits and brain areas, as opposed to recruiting neuronal partners in completely different brain regions/circuits. In addition, TCN exhibited a considerable amount of newly formed spines after injury that were largely stable in their life-time. As such they could potentially be responsible for compensating the loss of spines observed in this work and play a key role in the compensatory mechanism of re-establishing pre-existing circuits post-TBI.

As a whole, the changes in spine dynamics and circuit connectivity of TCN in the intact contralesional cortex after TBI that were uncovered here, may open up new avenues of treatment options to improve recovery after injury in the future.

- INTRODUCTION -

This thesis presents work on the in vivo spine dynamics and circuit connectivity of transcallosal neurons in the uninjured cortex after traumatic brain injury in the related mouse model of controlled cortical impact using in vivo two-photon microscopy and a special monosynaptic rabies virus tracing technique. The following chapter introduces all the aforementioned and important concepts and mechanisms.

1.1 Traumatic brain injury

1.1.1 Definition & epidemiology

Traumatic brain injury (TBI) is described as “damage to the brain resulting from an external mechanical force” (Xiong et al., 2013, p.128) ¹, caused either by events that lead to rapid acceleration/deceleration or penetration by a projectile ¹. TBI is thought to be one of the most prominent causes of death and disability around the globe ^{1,2}. In fact, its incidence is said to be greater than that of spinal cord injury, some forms of cancer, multiple sclerosis and HIV ². In line with reports from the World Health Organization, TBI will outrank other prevalent diseases as the leading cause of mortality and disease burden by 2020 ³. As much as 69 million people are estimated to endure TBI each year ⁴, with motor vehicle accidents representing the biggest source for TBI globally, followed by falls, violent crimes and sports-related injuries ³. In addition, war-torn regions or areas with elevated crime rates, show a larger fraction of TBIs caused by blast waves, gunshot-injuries or violent assaults ^{3,5}. A recent study estimated that in 2012 over 55.000 deaths occurred in the European Union alone ⁶, showing the effect that TBI-related accidents have on overall mortality. In a recent publication, the highest incidence of reported TBI was found in North America (1299 cases/100.000 people) and Europe (1012 cases/100.000 people) ⁴. Further, more than 5 million people in the United States and over 7 million people in Europe endure short- and long-term TBI-related disabilities ⁵. Generally there is a pattern in which TBI tends to be most common in young children and young adults ⁷, “by the virtue of their activities [...] and risk-taking behaviours [...]” (Najem et al., 2018, p.392) ². However the age at which TBI occurs and thereby the source of injury has shifted in high-income countries ⁸. As such, the predominant notion that young male adults are the most affected demographic still holds true, however the number of elderly people suffering from TBI due to falls is on the rise, especially in developed countries ^{7,8}.

Whether it happens in low- or high-income countries, TBI will often lead to long-term neurological, cognitive and behavioural impairments that typically last beyond the acute injuries to the brain. In that respect, TBI is regularly associated with comorbidities like depression, PTSD ⁹, chronic encephalopathy, seizures, Alzheimer's and Parkinson's disease ¹⁰. It is these chronic and persistent pathologies that require continuous treatment following the acute injury and cause an immense socio-economic burden on the global economy ^{2,11}. This burden and the cost of treatment certainly affects the patients themselves, but also their relatives and care-givers in terms of financial costs, psychological strain and overall reduction in their productivity within society ^{5,11}.

1.1.2. Pathophysiology of TBI

The pathology of TBI involves several complex injury mechanisms and pathways. Principally they can be divided into primary and secondary injury processes. The injury cascades which arise as a direct result of the insult to the brain are called primary injury mechanisms ¹². This type of injury occurs directly at the time of impact ¹³ and results in deformation or contusion of the brain tissue (directly or indirectly through contre-coup movements) and skull fractures which lead to lacerations and tearing or shearing of the brain tissue, the blood vessels and the axonal white matter ^{12,14}. Secondary injury, a complex accumulation of detrimental biochemical and molecular events, is then started through the evolution of primary injury mechanisms ¹⁴. It has been established that the consequences of secondary injury processes can contribute and lead to the long-term neurodegenerative, inflammatory as well as behavioural/cognitive/motor dysfunctions arising in patients and pre-clinical models years after the initial insult ¹⁵. As such, secondary injury can develop and last from minutes to hours to months after injury ^{1,13}. In this respect, if blood vessels tear open or get compressed via primary injury, fluids can accumulate in the brain which in turn results in secondary injury mechanisms like ischemia, oedema, elevated ICP, hypoxia, decrease in cerebral blood flow, as well as brain swelling ^{12,13,16}. These processes further unravel into the breakdown of oxygen and ATP delivery to the brain. As such there is ultimately also decreased glucose uptake and thus less ATP readily available for energy-dependent processes within each cell in the brain ^{10,16}. As a result the normal function of sodium-potassium pumps is perturbed, which in turn can lead to disturbed signal transmission and a massive influx/outflux of calcium, potassium and sodium ions as well as neurotransmitters (in particular glutamate), that in turn starts destructive processes ^{10,16}. In particular, excessive glutamate release can cause overstimulation

of neighbouring post-synaptic neurons and causes over the top calcium influx, starting a process termed excitotoxicity¹⁶. In this respect, the increased levels of calcium create a signal to recruit proteases, phospholipases and lipid peroxidases, which are enzymes that “dismantle” vital cellular components (proteins, lipids, nucleic acids in DNA etc.) and start apoptotic and necrotic pathways^{10,13}. Other consequences of the massive calcium influx and the activation of phospholipases are the increased production of reactive oxygen/nitrogen species that damage cells^{10,13}. During healthy metabolic activities cells normally produce reactive oxygen/nitrogen species. However their damage is kept at bay by our defence/scavenging systems¹⁰. TBI disturbs the normal function of the respiratory electron transport chain, resulting, amongst others, in an overproduction of reactive oxygen/nitrogen species. Thus following TBI, the defence systems are overpowered by the amount of the latter and cannot prevent the damage they cause anymore¹⁰. Furthermore TBI causes mitochondrial dysfunction^{10,13}. Mitochondria, the power house of the cell, are not able to buffer the excessive amount of calcium ions or fend off reactive oxygen/nitrogen species and thus collapse in their function^{10,13}. This again leads to less ATP being produced and thus energetic depletion of the cells down the line, perpetuating the vicious cycle of damage after TBI and ultimately the death of brain cells or the initiation of more apoptotic programs¹⁶. The necrosis and apoptosis can in turn present as degeneration or atrophy of the grey matter and cause a massive loss of neuronal input at the injury site, which in turn may influence overall brain function of other intact areas, such as the contralesional uninjured hemisphere. Hence, both the injured as well as the intact cortex are impacted by the detrimental cellular effects of TBI¹⁷⁻²⁰. In addition TBI triggers neuro-inflammatory responses²¹. In fact, damage within the blood-brain barrier (BBB) can result in cells infiltrating the brain and cause increased inflammatory responses^{13,21}. Microglia and astrocytes are quickly recruited to the site of injury and, or if injured themselves, trigger the release of cytokines/chemokines and other pro-inflammatory factors that attract more immune cells, intensifying the already existing cellular damage^{13,21}. Furthermore TBI can also start the immune response of the complement system²¹.

Finally, and of particular importance for this work, is the damage TBI can cause to the white matter of the brain. Disrupted white matter integrity has been found in several white matter tracts of TBI patients and animal models of TBI, in the form of lesions or atrophy of the internal capsule (IC) and most importantly the corpus callosum (CC)²²⁻²⁴. In effect, white matter tracts are particularly sensitive to

shearing, tearing and stretching forces created during TBI and the subsequent secondary injury processes ²². The resulting damage, if dispersed within the tracts of the brain, is referred to as diffuse axonal injury (DAI) ²³, and is considered defining feature of TBI ²⁵. The forces of TBI causing tissue deformation first interrupt axonal transport, by dismantling and breaking down cytoskeleton components like microtubules and neurofilaments. In addition, excessive calcium influx generated by secondary injury processes proceeds to disassemble these components further and also causes mitochondrial dysfunction, leading to energy depletion of axonal transport processes ²⁶. As a result the cellular debris, such as neurofilament pieces, and other transported proteins, such as amyloid precursor protein, accumulate in the axon ^{26,27}. Consequently axons begin to swell up and disconnection of the axon may follow, as seen by a singular bulb like swelling at the axon terminal ²⁸. Such axonal swelling has also been observed in the CC ¹². Ultimately, the majority of axotomized axons go through Wallerian degeneration and thus disconnection ²⁹. The latter then leads to the loss of input of neurons that are connected to the severed axon and can create network disturbances. However, some axons that do not go through Wallerian degeneration may recover from the damage but still suffer from reduced conduction velocities³⁰. In addition, myelin aberrations, as well as full demyelination of axon stretches, can occur after TBI ^{29,31}, and have been observed regularly in the CC ^{31,32}. Demyelination of axons on the other hand can create a lag in signal transduction and thereby derail communication between neural circuits ^{23,30}.

1.1.3. Therapy and treatment options for TBI

In terms of treatment options primary injury mechanisms have little to no potential to be stopped or manipulated ^{1,16}, unless protective measures like wearing a helmet or a seatbelt are taken ¹. Therefore the majority of therapeutic options following TBI have focussed on confining and attenuating the damage caused by the more long-lasting and delayed secondary injury mechanisms ^{13,16}. Efforts to find viable and effective treatment solutions have been ongoing for many years. However few, if any, preclinical studies have so far turned into successful clinical trials ^{7,13,33}. Thus far treatment options for TBI are limited and have varying degree of success depending on the sustained type of TBI, its severity and the patients features (age, medical history etc.) itself. Nevertheless TBI is routinely managed in a clinical setting by non-pharmacological and pharmacological options: First, patients undergo a neurological examination in which injury severity is assessed. The most commonly

used assessment scale is the so called Glasgow Coma Scale (GCS) ^{7,34}. The GCS evaluates a patient's level of consciousness on a scale from 3-15 and further determines their verbal, motor and visual skills/movements accordingly ^{34,35}. Here, the more severe the injury is, the lower the score and the less conscious and responsive the patient is. Secondly the neurological status of a TBI patient is evaluated by several imaging techniques to assess progression of factors like oedema, haemorrhage, fractures, or BBB problems ^{2,12}. Other early interventions can include elevating the head of patients to reduce ICP ⁷, therapeutic cooling (which albeit controversial, is said to reduce oxidative stress and other secondary injury processes after TBI) ^{7,33}, hyperventilation (to reduce ICP) and osmotherapy ⁷. Osmotherapy represents the administration of hyperosmolar solutions (like mannitol or hyperosmolar saline) into the blood flow and has been shown to reduce ICP and regulate cerebral blood flow ^{2,7}. In severe cases, and also tested in animal models ³⁶, patients undergo brain surgery in which the skull is opened and partly removed and/or cerebrospinal fluid is drained to reduce ICP or they have to be placed in a medically induced coma ⁷.

Furthermore, many pharmacological approaches have been tested with varying success in the clinical routine. Amongst others amantadine, an N-methyl-D-Aspartate (NMDA)-receptor antagonist has been shown to help with improving cognitive and functional recovery ^{7,33,37}. Furthermore erythropoietin (EPO), which plays a role in the production of red blood cells, has been shown to exhibit a neuroprotective effect after TBI, by decreasing excitotoxicity, secretion of reactive oxygen species and inflammatory cell presence ^{7,13}. Other clinical trials have shown that methylphenidate and progesterone had promising treatment effects ³³. On the other hand a great amount of substances have been examined in animal models of TBI and have shown beneficial effects for recovery of brain function and structure. These compounds/molecules include agents that increase the level of cyclic adenosine monophosphate (cAMP; in order to induce axonal outgrowth and compensate for axonal injuries after TBI), growth factors such as vascular endothelial growth factor (VEGF), nerve growth factor (NGF) and basic fibroblast growth factor (FGF2) ¹³. Further, provision of monocarboxylate (lactate, sodium pyruvate etc.; to help overcome metabolic stress/depletion after TBI) ¹⁰, anti-inflammatory agents, such as minocycline, and cell cycle inhibitors (to reduce lesion volume and cell death) have been tested with promising results ¹³. In addition transplantation of mesenchymal, neural and embryonic stem cells have also shown positive effects for a faster recovery in several animal models ^{7,38}. Finally, there also

exist non-pharmacological therapeutic measures that can be applied after initial management of the injury in the acute phase. Here the focus lies on improving the patients arising cognitive, psychological and motor deficits by physical therapy training, cognitive training, psychotherapy³³ and transcranial magnetic stimulation²⁷. A novel point of reference to treat the devastating effects of TBI could be the use of or promotion of possible structural plasticity in the remaining intact brain after injury. Uncovering whether such plasticity in the form of spine and circuit changes in the intact contralesional hemisphere exists, represents a focal point in this dissertation.

1.2. Modelling traumatic brain injury- The controlled cortical impact model

None of the above mentioned findings on the pathology of TBI or the respective therapeutic measures would have been uncovered without experimental models of TBI. While cell culture-based and mathematical models of TBI exist^{35,39}, several animal models of TBI have been brought forward to reproduce the injury mechanisms, as close as can be to the human condition. In fact, replicated consequences of human TBI in animal models include neurological, motor and cognitive deficits lasting up to a year after experimental TBI and extensive axonal degeneration in the CC, striatum and thalamus⁴⁰. Further, substantial tissue loss and cell death, enlarged ventricles and degeneration of the thalamus^{15,34} and atrophy of the cortex and hippocampus have been reported^{41,42}. Brain haemorrhage, swelling of the brain, as seen in humans¹, as well as epileptic seizure activity⁴³, oxidative stress and extensive neuro-inflammation have been detected in several animal models of TBI^{21,34,44}.

The most prevalent animal models of TBI to date are: the weight drop model^{45,46}, the fluid percussion injury model⁴⁷ and lastly the controlled cortical impact model (CCI)¹⁰. In recent years, animal models that mimic injuries caused by blast waves, as experienced during war situations, have further completed the catalogue of available experimental models⁴⁸. In their essence, each of the different animal models relies on the same principle, but all of them exist in different variations and do not represent a defined, singular paradigm. For this thesis the CCI model in particular was sought out as the animal model of TBI of choice for reasons outlined below: The CCI model was first developed in the late 1980s in ferrets⁴⁹. Later it was adjusted to function in rodents like rats and mice⁵⁰⁻⁵² and further scaled to pigs and non-human primates⁵¹. It has become one of the most commonly used and widely validated models for brain injuries⁵¹. In this particular model, following a

craniotomy that leaves the dura mater intact, a pressure-driven metal or steel piston is driven onto the brain. As a result of the metal rod being pneumatically driven into the brain, the tissue within the area of the impact, usually dies off and can create a cavity or “contusion core”, a few days after injury¹⁰. Thus, such an impact produces a mainly focal injury^{1,13} and the experimenter can precisely target the region in which the injury will be inflicted. Nevertheless, diffuse injury effects, such as DAI, have been reported^{17,50,51,53}. Due to the fact, that one integral element in this thesis consists of leaving one hemisphere intact while the other side should sustain a TBI it appeared to be a suitable model for our purposes. In addition CCI is highly reproducible^{1,33}, because almost all injury parameters, such as injury depth, impact velocity, dwell time of the impactor/piston tip on the brain and diameter of the latter can be chosen by the experimenter and can be controlled within different experimental paradigms^{33,37}. This poses another great advantage of CCI, as one can adjust the injury severity to ones experimental needs and may regularly induce a reproducible injury⁵¹. Also, in comparison to other animal models rebound injury does not occur¹. Further, mortality in CCI is rather low and injury mechanisms that occur long after the initial impact may be studied⁵¹. This was also a favourable argument to use CCI for this research work, as one primary interest lied in investigating long-term as well as short-term effects of injury on dendritic spine morphology and possible circuit reorganisation. Moreover CCI has proven to be a good model to study pharmacological interventions⁵¹ (i.e. the use of amantadine^{54,55}, methylphenidate^{56,57}, hypothermia⁵⁸ and effects environmental enrichment on injury outcome after TBI⁵⁹), which once more confirms its importance as a TBI model. Of course every animal model has its advantages and disadvantages, however CCI is reliable, easy to use and its broad validated use made it a great candidate for studying TBI in this thesis. This is especially true, since a plethora of disease mechanisms observed in human TBI patients can also be seen after CCI. Here, such observations include cortical contusion⁶⁰⁻⁶², opening of the BBB and inflammatory cell invasion^{52,63-65}, cortical, hippocampal and thalamic cell loss and degeneration^{17,66-68}, tissue atrophy^{1,69}, apoptosis^{63,70,71}, increased presence of reactive oxygen species⁷²⁻⁷⁴, oedema^{75,76}, altered blood flow and pressure responses^{50,77}, high ICP^{36,60,68}, axonal injury^{53,67,78,79} and in severe cases comatose states⁷⁹. CCI has also been reported to induce changes in dendritic architecture in the ipsilesional cortex⁸⁰⁻⁸², as well as changes in spine density⁸³⁻⁸⁵. Additionally, memory and cognitive impairments have been observed after CCI^{56,69,86}, depending on how severe the injury was^{87,88}. Furthermore chronic behavioural problems have been found, which stemmed from intense tissue degeneration in the cortex,

hippocampus but also in the CC ^{7,17}. Finally, CCI has also been used in the study of co-morbidities that come at later stages after TBI such as epilepsy ^{60,89} and Alzheimer's disease ^{28,90}.

1.3. Dendritic spines: From their structure to being the gateway of synaptic connections

The human brain is a highly complex organ that is generally but not solely comprised of as many as around 100 billion neurons ⁹¹. Neurons are connected to each other, forming cohesive neuronal circuits. Their interplay between each other as well as other cell types, like glial cells, allows us to be a conscious and responsive functional entity. Thus far, several studies have suggested that small protrusions along a neurons dendrite (branches that themselves protrude from the neuronal cell body and are distinct from axons), play an important role in neuronal communication and circuit building. Historically, Ramón y Cajal was the first to discover these small protruding nodules on the dendrites of cerebellar Purkinje cells of chicken, giving them the name of “spines” ⁹². Since then it has been established that spines are a part of all vertebrate brains (and some invertebrates ⁹³) that exist in different shapes and sizes ⁹⁴. In that sense, spines can be described as small protrusions growing out of and residing on the apical, distal or proximal parts of neuronal dendrites respectively. Early reports suggest that there are about 1 trillion spines present in the human brain ⁹³ and as much as 100.000 spines can gather on the dendritic arbour of an individual rodent neuron ⁹⁵.

Morphologically, spines are incredibly multifaceted, but are usually categorized into 3 types: Mushroom, thin and stubby spines ⁹⁶(see Figure 1). Other, more recent, classifications include filopodia ⁹⁷ (see Figure 1). In more detail, mushroom spines are bulky and have a big diameter head, sitting on top of a slender neck ⁹². In contrast thin spines have a much smaller diameter round head, but still possess a thin neck ⁹⁵. Mushroom and thin spines have the commonality of the head and neck feature, which is in fact the most characteristic feature of a mature spine in the adult central nervous system (CNS) ⁹⁵. They are considered to be more stable in their morphology and do not change their shape and size often. However thin spines are reported to be more responsive to and responsible for plastic changes in the brain, because they still have the capacity to become bigger and mature into a more stable mushroom-type-like nature ⁹⁷. On the other hand the third category of spines, namely stubby spines, are mostly sessile and short in length ⁹⁵. They do not have the classic head-plus-neck composition ⁹⁷. Instead they just protrude from the

dendrite like a small bump. Stubby spines are, in contrast to thin and mushroom spines, more prevalent in the immature developing brain ^{93,97}. Finally, filopodia are long slim, worm-like, protrusions ⁹⁷ and can be hard to resolve under a simple light microscope, due to their slim shape ⁹². Filopodia are highly dynamic in their shape and high in occurrence in young, as opposed to an almost complete absence in adult mice ⁹⁸.

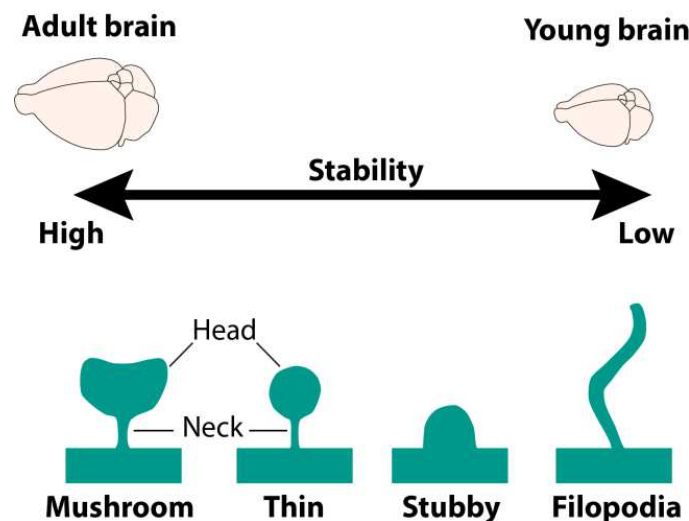


Figure 1. Illustration of spine morphology and characteristics. Mushroom spines are characterized by a big cup-shaped head. Thin spines have a smaller more circular head. Both reside on top of a thin neck and are more prominent in the mature adult CNS. They generally do not change their shape, ensuring a more stable morphology and function. Stubby spines do not have a neck but are bulbous protrusions growing out of the dendrite. Finally filopodia are thin and long protrusions emanating from the dendrite. Both stubby spines and filopodia are most abundant in the developing CNS and more dynamic in their shape, size and lifetime. Modified from Rochefort & Konnerth, 2012 ⁹⁶.

Ramón y Cajal had a hunch about the possible function of spines, as a way to maximize “receptive surface” of contact points for axon terminal fields ^{95,99}, but their function has yet to be fully understood. The smallest entity of each neuronal circuit is the synapse, the physical point of connection between neurons that allows them to operate as processing units for sensory input and subsequent (motor) output ¹⁰⁰. Thus far the function most commonly associated with spines, is that they operate as a proxy for (excitatory) synapse formation and are the stepping stone to creating new connections between neurons ^{97,101}. In that respect, the majority of excitatory axon-to-dendrite synapses reside within spines ⁹⁷. Hence their presence is associated with the presence of excitatory synapses and thus the possibility of synaptic plasticity and changes in circuit connectivity ^{102,103}. In fact, typically one singular mature spine encapsulates one single synapse that can accept input of one axonal synapse, ⁹⁴. Rarely, spines can have two or more heads and facilitate more

than one synaptic input onto it ⁹⁵. Mushroom spines are said to accommodate the biggest and more stable excitatory synapses ⁹⁷. As a result of being a facilitator for synaptic connectivity, bigger and more “mature” spine types contain all the necessary components to build an excitatory synapse. First and foremost they are defined by the presence of a post-synaptic density (PSD), which looks like a dense and dark thickening of the spine membrane under an electron microscope ⁹⁶. The PSD in spines is highly structured in the sense, that it contains an array of specialized molecular systems organized meticulously within itself ¹⁰⁴. Amongst others it contains α -amino-3-hydroxy-5-methyl-4-isoxazolepropionic acid (AMPA)- and NMDA- receptors, metabotropic glutamate receptors, as well as voltage gated potassium, sodium and calcium channels ^{96,105} in order to facilitate neuronal signalling. Polyribosomes (enabling mRNA transcription)⁹², and a special type of smooth endoplasmatic reticulum for the purpose of storing calcium intracellularly are also present in spines ⁹⁴. In addition several proteins involved in crucial molecular signalling pathways or spine structural stability (for example cadherins or receptor tyrosine- kinase and other kinases have been identified within spines ⁹⁵. Especially adhesion molecules like cadherins are important for the formation, maturation and stability of spines and their inherent synapses ¹⁰⁶. Finally, excitatory spines contain typical cytoskeletal proteins, like actin filaments (in the shape of elongated tubes in the spine neck ⁹⁶ and interwoven like a grid in the head ⁹⁴, actin binding proteins (such as myosins) ¹⁰⁵ and coated transport vesicles ⁹⁴. Furthermore the PSD of spines can also contain a specific excitatory synapse scaffold protein, called PSD-95 ⁹⁷. Interestingly, microtubules are rarely part of the spine machinery ⁹⁴. More immature categories of spines, like stubby spines, may display some synaptic structures under an electron microscope, but will have a much different composition of AMPA- and NMDA-receptors, as well as other scaffolding proteins, and no PSD-95 ⁹⁷. In the developing brain filopodia, often do not have a PSD, but still seem to have basic synaptic attributes (like a synaptic cleft or synaptic vesicles) ⁹⁷, thereby having the potential to fully develop into more mature spine types ^{95,96}. As a result, they have been said to function as spatial probes, searching and probing for possible pre-synaptic partners in early development ^{107,108}. In effect, only a small fraction of filopodia become actual spines ^{109,110} and the fleeting contact made usually will result in failed synaptogenesis ¹⁰³. Furthermore, it seems that spines are not an absolute pre-requisite for functional synapse formation, since synapses also exist on the dendritic shaft ¹¹¹. Newer theories support the notion that spines facilitate a higher synapse efficiency (hence the molecular machinery) and broaden the computational power of neurons ⁹⁵.

Lastly it is believed that spines serve to compartmentalize post-synaptic signalling, gene expression and most importantly calcium signals from the rest of the system ^{93,112,113}. Here the spine neck creates a bottleneck/barrier between their head and the rest of the dendrite/neuron. In addition spines can function as a coincidence detector of pre- and post-synaptic activity with their calcium signalling machinery ⁹⁶ and further corroborate that small spine compartments can serve as a location of synaptic circuit strengthening. More recent advances have also shown, that spines need not just be equipped with excitatory synapses ¹¹⁴. In fact, about one third of inhibitory synapses can also lie within dendritic spines ¹¹⁵ and are usually placed next to an excitatory synapse, making them spines with two synaptic outlets ^{114,116}. These inhibitory synapses can halt activation of the excitatory synapse and are also much more dynamic than the latter, since they appear and disappear at the same location, while excitatory synapses tend to remain more stable ^{114,116}.

Finally, one of the hallmarks of spines is that they are highly dynamic structures. As such, they can form but also disappear and even re-appear at any point in time¹⁰³. How malleable spines are, becomes especially clear when spine dynamics are analyzed from early development to their state in the adult brain. As a general rule it has been widely accepted that dendritic spines are more abundant and also more dynamic in the developing brain ^{98,117,118}. That said, spines and filopodia are rapidly formed at a high rate and number but tend to disappear quickly within minutes to hours during early development of the brain ⁹⁹. This excessive formation of spines is suddenly followed by a drastic decline of spines in adolescence ¹¹⁹, in which essentially fewer spines are formed or at least more are eliminated, hinting at a pruning process transitioning from young age to adulthood ^{98,117,120}. Similar pruning processes have been observed in humans and primates ^{121,122} As the CNS matures, spine density declines, their morphology becomes more stable and their lifespan more durable ^{98,99,117,118}. As a result of spine dynamics “calming down” in the adult brain, the overall number of spines remains steady, since the elimination and formation rate balance each other out ⁹⁷. Nevertheless, even in adulthood, spines retain a dynamic capacity and exhibit a certain rate of elimination and formation throughout their lifetime, which made them an especially interesting structure for this thesis. As such the rate of appearance and disappearance can be an indication as to how plastic and adaptable synaptic organization/plasticity is under different conditions. In that respect, spine dynamics and morphology can be heavily influenced by experience-dependent processes, like sensory deprivation, learning or enriched environments ^{109,123-126}. In addition, irregular spine dynamics

have consistently been linked to several neurological, neurodegenerative and psychiatric diseases like fragile X syndrome ¹²⁷⁻¹²⁹, autism spectrum disorder ^{130,131}, Down's syndrome ^{111,132,133}, schizophrenia ^{134,135}, Alzheimer's, Huntington's or Parkinson's disease ¹³⁶⁻¹³⁹. Most importantly though, several studies have indicated that CNS injury caused by stroke/ischemia or TBI may drastically influence spine dynamics as well ¹⁴⁰⁻¹⁴².

As a whole, it becomes clear that spines are enormously versatile structures in the CNS. While their function is not yet entirely understood, their changing morphology and dynamic behaviour throughout their lifetime are inevitably linked to the formation and elimination of functional synapses and thus functional circuit connectivity. An imbalance of the spine system created by TBI can lead to exacerbated long-term cognitive and behavioural deficits ¹⁴³ and thus further corroborates their importance in the normal healthy brain. As a result spine dynamics were chosen to be the main measure of structural plasticity after injury in the present dissertation.

1.4. Transcallosal neurons and their corticospinal counterparts:

1.4.1. Transcallosal neurons

Transcallosal neurons (TCN) or callosal projection neurons, just like spines, are an important contributor to normal brain function. TCN are a specific type of (mainly) pyramidal neurons residing in the cortex ¹⁴⁴. They are predominantly excitatory neurons ^{144,145}. However, some reports suggest that they can also exhibit spiny stellate cell morphology and properties ^{146,147} and can also have an inhibitory character ¹⁴⁸⁻¹⁵⁰ (according to Ramos et al., (2008) ¹⁴⁵ about 1-5% of TCN in rodent brains are GABAergic in nature ¹⁴⁵).

Further, their axons assemble to become the largest fibre tract in the mammalian brain ¹⁵¹, comprised of 200-800 million axon fibers ¹⁵²⁻¹⁵⁴, the CC (see Figure 2, further down in this text). Historically, the CC itself was discovered and described as a unique structure of the brain in placental mammals for the first time in the early 1800s by Owen ^{151,155}. In placental mammals, therefore in humans and rodents alike, there are 3 principal fibre tracts: the anterior commissure, which connects the olfactory to the limbic system, the hippocampal commissure primarily connecting the limbic system and finally the CC, which connects an array of cortical areas and is the biggest axonal commissure in the human brain ^{156,157}. In this respect, TCN are special in that they have one of the most important long-distance

axon fibres in the mammalian brain ¹⁵⁸ that connect both cerebral hemispheres to each other via the CC, passing through the brain from one side to the other ¹⁴⁴.

In turn, they, and thus the CC, play a crucial role in inter-hemispheric communication and coordination of the different brain regions of either hemisphere ¹⁵⁹. Since both hemispheres contain representations for every brain region, callosal axons allow information to travel from one side to the other and each hemisphere to access the information from the opposite representation and/or other brain sections, making it one of their primary functions ¹⁵⁴. Particularly, most somatosensory and motor functions, as well as higher order associative and cognitive tasks necessitate the engagement of both hemispheres and thus the coordination and extensive information processing originating in both sides ^{154,159}. While team-work between the hemispheres is important, and the predominant model of how the CC conveys inter-hemispheric coordination/communication is through excitation, there are also cases in which it is necessary for one hemisphere to act without the intervention of the other hemisphere. In this case, the CC prevents activity in just one hemisphere, without shutting it down completely, thus enabling the other side to act and process information independently and supporting the concept that the CC also acts through inhibition ^{152,154,156}. The importance of functional CC connectivity is underlined by instances in which its function and/or anatomy is perturbed by disease mechanisms. To this date many studies have linked psychiatric disorders (like schizophrenia ^{160,161}), or other illnesses like multiple sclerosis ¹⁶²⁻¹⁶⁴, dementia ¹⁶⁵⁻¹⁶⁷, autism ¹⁶⁸⁻¹⁷⁰, attention deficit hyperactivity disorder ¹⁷¹⁻¹⁷³, and dyslexia ^{174,175} to abnormalities of the CC. Most importantly though the CC, and thus TCN, are particularly affected by TBI. In fact several studies have shown that TBI leads to a range of CC abnormalities (for example changes in functional anisotropy, structural integrity and connectivity as well as axonal swelling, demyelination and metabolic disturbances) and strains axons of long-range projection neurons like TCN ^{31,78,176,177}.

Finally, most of our knowledge on the location and distribution of TCN across the cortex is based on anatomical tracing studies with retrograde and anterograde tracers ¹⁷⁸. From those studies we know that, as pyramidal neurons, TCN predominantly lie in layers II/III and layer V of the cortex ^{144,145,179}, and in accordance with our study also in layer IV and VI but to a lesser degree ¹⁷⁸ (see also Figure 2). In more detail we showed, that this layer distribution is mostly conserved and uniform across the whole cortex in different regions of the brain, namely the

motor and somatosensory cortex (and also in particular the barrel cortex) ¹⁷⁸. Moreover, TCN provide synaptic input to a subset of layer II/III and V pyramidal neurons of the, ipsi- and contralateral, cortex ^{179,180}.

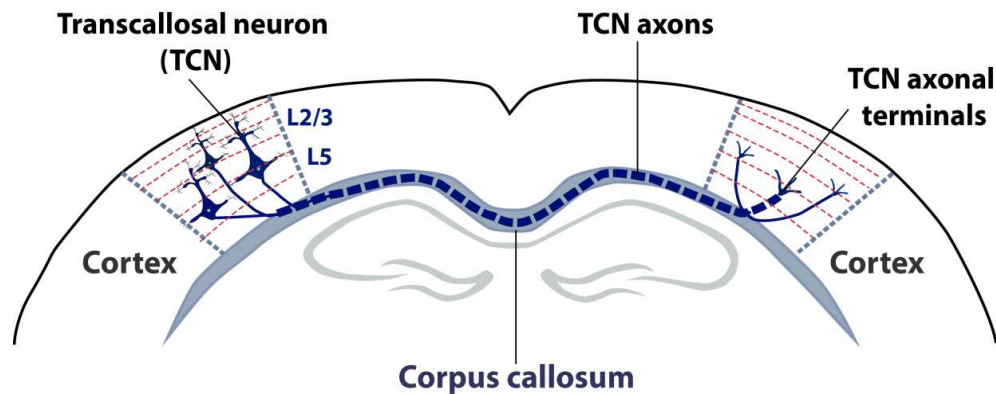


Figure 2. Schematic illustration of transcallosal neurons (TCN) in the mouse cortex. TCN are pyramidal neurons of the cortex, whose axons make up one of the biggest white matter tracts in mammals, the corpus callosum. TCN cell bodies primarily reside in layers II/III and V of the cortex and their axons project homotopically to the contralateral hemisphere, where they terminate in the cortical column. Adapted from Fame et al., 2011 ¹⁴⁴

Also, while some brain regions like the visual cortex have plentiful connections made up of TCN, some only have few ¹⁵⁴. For example it was observed, that in cats 80% of pyramidal neurons in layer II/III of area 17 and 18 of the visual cortex are TCN ^{179,181}. In addition TCN have been reported to project homotopically to the contralateral cortex ^{159,178} in a columnar fashion ^{145,178} (see Figure 2). This means that the location of the cell body on one side of the cortex directly mirrors the projection site on the opposite side. Heterotopic connections also exist ^{159,178,182}.

Last but not least, the CC and TCN fibres can be divided into 6 parts according to which homotopic areas it connects between the hemispheres: Namely the frontal, motor, somatosensory, auditory, temporoparietal, and visual parts of the CC ¹⁴⁴. In this respect TCN within the CC are organised in a topographic fashion, thus the location of the axon within the corpus callosum represents/predicts their anatomical location within the cortical hemisphere they project to. Hence more anterior portions of the CC connect more anterior areas in the brain (i.e. the anterior part of the CC, called the genu in humans, connects prefrontal cortices), central chunks of the CC connect motor and somatosensory cortices, and finally more posterior cortical regions are connected via more posterior parts (i.e. in rodents visual fibres) ^{151,152,154}. This topographical organisation is more pronounced in primates than in rodents ¹⁵¹.

It becomes clear that TCN are a special kind of neuronal population. They are necessary to manage the crucial and complex task of information transfer and processing within and across both brain hemispheres. As an anatomically connected element between the injured and intact hemisphere after unilateral TBI they may play a crucial role in the recovery of sensory and motor processing after TBI. Thus they were chosen to be the focus of this thesis.

1.4.2. Corticospinal tract neurons

On the other hand, corticospinal tract (CST) neurons and their axons make up the CST, which represents the most critical descending motor pathway and facilitates voluntary movement ¹⁸³. In that respect, muscle activity initiated through the spinal cord is controlled from neurons within the cortex, especially for the fine movement of upper extremities like the hands ¹⁸⁴ but also the body ¹⁸⁵. In rodents their cell bodies lie primarily in deeper parts of layer V of the primary motor, but also somatosensory cortex ^{185,186} (see Figure 3). From the brain, CST neurons residing in layer V, send their projections down to the spinal cord through the ipsilateral CC and the IC ¹⁸³. At the level of the midline the majority of CST axons (above 90%) cross said midline, before they traverse the spinal cord further down ¹⁸³ (see Figure 3). As a result, most of the axons project to the side of the spinal cord that is contralateral to the side of the hemisphere in which their cell bodies reside. Furthermore, within the spinal cord itself the majority of CST axons (i.e. 95% of CST fibres) project to the ventral part of the dorsal columns and terminate in the dorsal horn ¹⁸³. A minority of the axons do not cross the midline and pass the spinal cord on the same side of the hemisphere their cell bodies originate from ¹⁸³ (see Figure 3). Two smaller parts of CST axons also project to the lateral and anterior column of the spinal cord (see Figure 3). The specificity with which CST fibres travel through different but defined parts of the spinal cord from different cortical areas, indicates their distinctive functions during complex movements ¹⁸⁵.

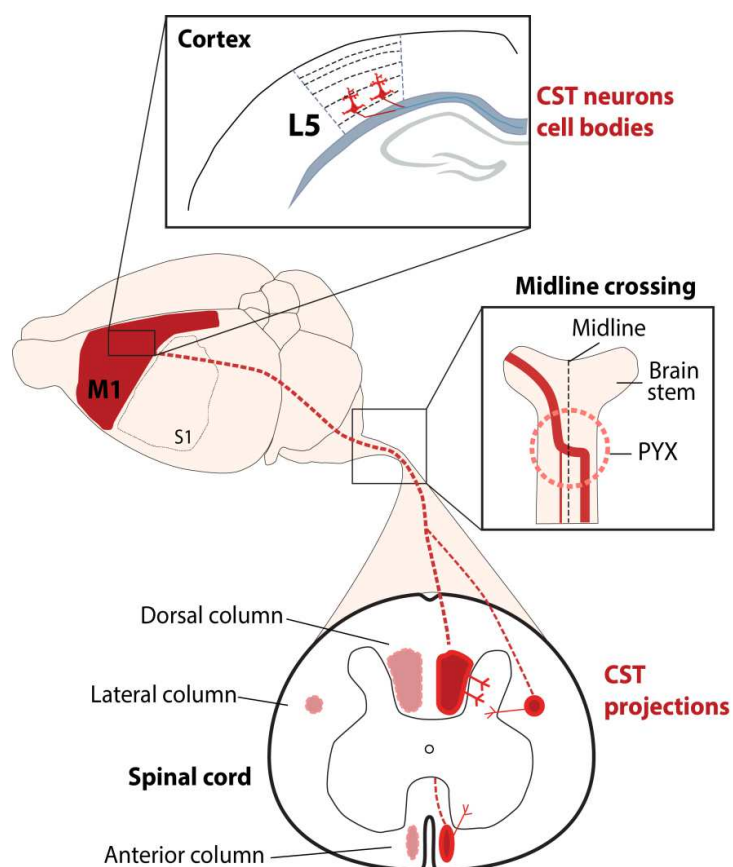


Figure 3. Schematic depiction of corticospinal tract (CST) neurons and their projections within the spinal cord. CST neurons primarily originate in layer V of the cortex. Their axonal fibres make up the CST, which project to the spinal cord, passing through the corpus callosum. At the height of the pyramidal decussation (PYX) the majority of CST fibres cross to the opposite side of the spinal cord to finally terminate in the ventral part of the dorsal or lateral and anterior column of the spinal cord. The dorsal column fibres make up the biggest part of CST projections into the dorsal horns. Adapted from Serradj et al., 2017 and Oudega & Perez, 2012^{183,187}

As a consequence of their anatomical projections and location, CST neurons provide a suitable counterpart to TCN neurons within this thesis, in the sense that they constitute a neuronal population that is not directly anatomically connected to the injured hemisphere following a TBI.

1.5. How does the brain react to injury? Recovery, remodelling and reorganization after injury- the current state of research

As explained in detail above, TBI results in drastic and detrimental consequences for the brain that may seem insurmountable to repair. Nevertheless, reports within the realm of various injury mechanisms (i.e. stroke, TBI, etc.) have suggested that the brain has a remarkable ability for recovery and has the potential to rescue some of its old functions and recuperate from the damage caused by an injury. The exact mechanism with which it does is still elusive and may represent an additional point of reference for the development of treatment/therapeutic options after TBI.

Typically, the brain processes information of a specific purpose in a specific area of the cortex. Therein, motor and sensory cortices for instance, are planned out as functional maps, which in the case of motor function integrate information from the

motor cortex to the musculature ¹⁸⁸. In the case of sensory function, information is integrated in maps that “connect” the sensory cortex and sensations of body parts to each other ¹⁸⁸. After injury or stroke some of these maps can be destroyed, and current research postulates that the brain may try to recover their lost function by either recruiting other areas to carry out the lost function or try to regenerate some of the lost tissue ¹⁸⁸. Interestingly, the brain displays “diffuse and redundant connectivity” (Murphy & Corbett, 2009, p.862)¹⁸⁸ which has been dubbed one of the keys to unlock the mechanism of functional recovery ¹⁸⁸. In theory, recovery can thus be divided into different steps: First, consequent tissue damage, cellular debris, changes in blood flow and inflammation have to subside and be resolved ¹⁸⁹. Then, intrinsic inhibition placed on certain redundant circuits could be removed, other functionally similar maps or pathways engaged, or completely new connections could be made to recover previously lost functions. What is more, is that it is still unclear whether the ipsilesional (or intact peri-lesional) and more importantly the contralesional side of a cortical injury contributes to such a functional recovery, and if so how. Several lines of research studying recovery after stroke and TBI have been brought forward and have contributed to the understanding of this question.

1.5.1. The intact parts of the lesioned hemisphere & recovery

The spared ipsilesional tissue may posit some major benefits for functional recovery, since for example neurons in the peri-infarct area (i.e. in close vicinity but not within the infarct core) after a stroke can usually survive ^{188,190}. Given their placement in a region where perfusion of the tissue is still enough to stay alive and recover from any damage caused, structural changes can still be recovered if reperfused in time ¹⁹¹⁻¹⁹³. Furthermore, the peri-infarct tissue experiences the biggest changes when it comes to growth-related processes or creating a pro-regenerative environment ^{188,190,194,195}. Such expression of growth-inducing factors can be a good substrate for axonal sprouting, regeneration or rewiring either after stroke or TBI. In that sense, previous research has shown an increase of growth-inducing genes and neurotrophic factors or the absence of chondroitin sulphate proteoglycans after TBI, especially in the intact areas of the injured cortex and other regions like the hippocampus ^{25,195-197}. Moreover, axonal sprouting has preferentially been seen in the peri-contused region after TBI ¹⁹⁸⁻²⁰¹ and has been correlated with functional recovery ²⁰². Such axonal sprouting has in fact been observed in the area close to the injury core, 1 and 4 weeks after CCI, indicating a potential of neuronal regeneration post-injury ²⁰³. All in all these findings show that

the injured white matter can somewhat bounce back from injury, making TCN that are anatomically connected to the injury a viable candidate for the promotion of functional recovery.

Reports that further substantiate the claim that the ipsilesional cortex plays a role for recovery are linked to the observation that shortly after stroke, activity of the injured area is greatly reduced and suppressed at first¹⁹⁴. On that note the injured cortex also exhibits activity fluctuations after TBI. Here studies have shown that shortly and up to 2 weeks after TBI responses are suppressed and hypoexcitability ensues in all cortical layers^{204–207}. This initial suppression is followed by attempts of the brain to, amongst others, increasingly activate spared but close-by functional maps¹⁹⁴. These measures are closely linked to the size of the injured area and further to the level of functional recovery outcome^{188,194}. In fact, the bigger the size of spared tissue on the ipsilesional hemisphere, the better the outcome^{188,189,194}. Furthermore, imaging studies visualizing functional brain maps have shown activation of peri-infarct and ipsilesional zones and that better recovery is achieved when initial bilateral overactivation shortly after stroke, shifts towards a more unilateral ipsilesional activation^{188,189,194,208}. In addition, functional maps, mostly in smaller strokes, can shift towards functionally similar but topographically close and spared regions serving as a mechanism for better functional recovery as a whole^{189,209–212}. In addition, studies have shown that dendritic and spine dynamics can be altered in the ipsilesional cortex, suggesting that increased turnover of spines is linked to enhanced functional synaptogenesis and thus better outcome of stroke recovery^{190,191,213,214}.

1.5.2. Effects of TBI in the contralateral intact cortex & recovery

Instinctively one might think that unilateral TBI may only cause substantial damage in the injured hemisphere. However, the contralesional intact cortex can be just as affected^{17,18,83,215}. The importance of these overall changes in the contralateral intact cortex for functional recovery is yet to be understood.

Here, stroke research has introduced many insights on that matter. In that sense, several studies have shown remapping and reorganization of the contralateral intact hemisphere after stroke and consequent functional recovery^{211,216–218}. Of these studies Abo et al., (2001)²¹⁷, for example, showed with functional magnetic resonance imaging (fMRI) that stimulation of the affected hindlimb, resulted in a shift of the sensory map to two previously non-active regions, one of them being the

intact contralateral sensory-motor cortex ²¹⁷. Furthermore, it was observed that receptive fields doubled in size in the contralateral (but also ipsilateral) sensory/motor maps after induction of small cortical infarcts ²¹⁹. Similar to stroke, past research has suggested that one-sided TBI can lead to reorganization of the intact contralesional hemisphere ²²⁰, and that recovery stems from such processes and not just axon or neuronal regeneration ²²¹. An example of such research is a study in which TBI was induced through a weight-drop model in rats and cortical maps of the contralateral intact hemisphere were analyzed via intracortical microstimulation ²²¹. As a result, the motor map representation of the injured limb was enlarged in the contralesional cortex for up to 5 weeks after injury ²²⁰. Therefore it was argued that motor maps must have reorganized in the contralateral healthy hemisphere after injury, in order to elicit such an uncommon response pattern/map representation ²²¹. In another study autoradiography was used to measure cerebral blood flow as a correlate for neuronal activity after CCI in rats ²⁰¹. Here, the affected hindlimb was electrically stimulated 4, 7 and 30 days after CCI and neuronal activity in both hemispheres was measured. Injured animals exhibited an increased activity in the intact cortex in the early time-points, which later subsided to the injured hemisphere after 30 days ²⁰¹. The authors thus concluded that there is a time-dependent process of reorganization happening in the intact cortex ²⁰¹. Furthermore, some evidence suggests that there can be increased synaptogenesis and increased dendritic outgrowth in the intact contralesional cortex. In that respect, electrolytic lesions induced helpful synaptogenesis in the contralateral intact cortex of rats, but appeared only after about 3 weeks post lesion ²²². Similar increases in synaptogenesis were also found after ischemic lesions and could also be experimentally linked with improved use of the affected limb if accompanied by training paradigms ²²³.

Moreover, recent studies demonstrated the importance of inter-hemispheric connections (i.e. TCN) for recovery of function. In more detail, Li et al., (2011)²²⁴ optogenetically controlled transcallosal excitatory layer III and V neurons in the intact somatosensory cortex of injured rats (contralateral to the non-injured paw, but ipsilateral to the injured one) projecting to the deprived cortex, where they recorded functional responses ²²⁴. Silencing these TCN lead to a decrease in dysfunctional inhibitory activity within the deprived cortex, highlighting the importance of TCN during cortical plasticity after injury ²²⁴. Furthermore, cutting off TCN communication in rats with a unilateral cortical infarct helped in making the use of the affected limbs more efficient ^{225,226}. Consequently, it has been suggested

that the inter-hemispheric imbalance after injury/stroke may be beneficial for functional recovery, since the loss of inhibition created by the injury on one side could facilitate modulation and reorganization of cortical maps in the contralateral intact hemisphere ^{227,228}. In an fMRI study, where sensory maps were analyzed after injury and stimulation of the affected forelimb for up to 4 weeks after injury took place, researchers could show that in the first 2 weeks after injury the contralesional cortex was also activated, implying a shift of the sensory map to the contralesional hemisphere ²²⁹. Ipsilesional activation was almost non-existent ²²⁹. What is more, the extent of the shift to the intact hemisphere, was correlated with injury severity (i.e. bigger lesions lead to a larger activation of the intact hemisphere) ²²⁹. A similar shift of the cortical map towards the intact hemisphere has been found by Maggolini et al., (2008)²³⁰. The authors lesioned the motor cortex and found that the contralateral intact cortex showed an increased motor map representation and reorganizes ²³⁰. This reorganization led to “the ability to elicit forelimb movements from cortex sites that would have not previously produced forelimb movements in response to similar stimulation” (Maggolini et al., 2008, p. 2743 ²³⁰). Further, it is, in general, not uncommon that both hemispheres experience a range of hyper- or hypo-activation after stroke and TBI ²³¹. These changes can lead to increased loss of lateralization of functions. In turn, this loss of lateralization and thereby elevated activation in both hemispheres, which is later normalized in favour of either hemisphere, may posit a beneficial environment for recovery. For stroke, it seems that this is dependent on the infarct size. In fact, larger-sized strokes in which both hemispheres are more activated than in small strokes (which usually just activate spared peri-infarct tissue without perturbing lateralization too much) have a lesser chance for a good outcome in functional recovery ¹⁸⁸. However since larger strokes do not have much tissue to rely on in the ipsilesional hemisphere, the brain may be forced to depend more on contralesional changes as a mechanism for beneficial functional recovery ^{232,233}. Finally, results presented in an in vivo imaging study by Takatsuru et al., (2009) ¹⁴² did not only show an increased turnover of mushroom spines in the intact hemisphere after infarct, but also noted an altered and new type of circuit activity had begun to occur at around 1 month after stroke induction ¹⁴². The authors thus linked the change in activity and turnover to improved functional recovery ¹⁴².

All in all it becomes evident that the contralateral intact hemisphere undergoes plastic changes after injury, which could be beneficial in promoting functional recovery. What is more, studies dealing with those plastic changes after TBI have

predominantly been focussed on in vitro or histological findings rather than in vivo experiments. Therefore the work of this thesis focussed on investigating plastic changes in spine dynamics and circuit connectivity of the intact contralesional hemisphere and their connected neurons after TBI in vivo.

1.6. Principles of two-photon microscopy and its advantages

An essential part of this thesis was the use of a cutting-edge imaging technique that goes beyond normal confocal microscopy, namely two-photon microscopy.

In the early 1930's Maria Göppert-Mayer was the first scientist to lay the theoretical groundwork of the two-photon excitation principle ²³⁴. About 30 years later Kaiser and Garrett corroborated the theory by practical experiments ²³⁵, while Sheppard and Kompfner conveyed more arguments for its possible importance in studying biological materials in the late 70s ²³⁶. Finally two-photon microscopy was practically implemented in an experimental setup to visualize, amongst others, chromosomes in live cultured pig kidney cells in 1990 by Denk and colleagues (1990) for the first time ²³⁷. The most significant impact of two-photon microscopy arose within the study of the CNS and its dynamic biological processes in vivo. In combination with the discovery of fluorescent dyes and transgenic animals expressing fluorescent proteins in neurons (see also ²³⁸), as well as the use of lasers as light sources to scan specimens in all 3 dimensions, it has become one of the most powerful techniques to investigate the intact and diseased brain in living animals. Most importantly though, and especially relevant to this thesis, in vivo two-photon microscopy has played a major role in the study of spine dynamics. Here its power essentially lies in the possibility to track the "behaviour" of the same neurons over a certain period of time, i.e. longitudinally, and in real time. While research based on imaging methods that only visualize the state of a cell at the time of fixation can provide valuable information on a general, broader level, in vivo microscopy can help identify how one or more particular neurons evolve and interact with other cells in real-time. As such in vivo two-photon microscopy has helped elucidate the plasticity and stability of spine dynamics in the intact brain ^{117,118,239,240}, after learning or "experience-dependent" tasks ^{124,241-243} and in the injured/diseased CNS ^{136,192,244,245}.

A main requirement to image the brain in vivo using two-photon microscopy, is unobstructed access to its surface (so that the emanating light of the microscope reaches the cell structures of interest, in our case dendritic spines)²⁴⁶. Thus far the

most widely used surgical procedures to access the brain are either the cranial window (CW) implantation or the thinned skull method. The CW implantation is a surgical procedure designed to mount a glass above the craniotomized brain. In the thinned skull preparation the skull bone is carefully milled down to a very thin layer ($\sim 20\mu\text{m}$ ²⁴⁷), so that the light from the microscope can pass through unhampered. It was crucial for this thesis to use the CW- technique, because it not only allows for a much bigger area of the cortex to be imaged ²⁴⁸, but can also enable a much deeper imaging depth, from $\sim 500\mu\text{m}$ depth upwards ^{247,248}, of even sparsely labelled tissue ²⁴⁹. Another major advantage of the CW-implantation is that, technically, an unlimited amount of imaging sessions within random intervals from the day of initial implantation can be completed ²⁴⁷. In this case, it was important to also understand spine dynamics long after the initial injury, which was only feasible with implanting a chronic CW.

Just like confocal microscopy, two-photon microscopy also relies on the principle of fluorescence. Fluorescence describes the ability of a specimen to emit light, at a shorter wavelength, than it previously had absorbed ²⁵⁰. In this respect, fluorophore molecules absorb light energy and are consequently booted up from their low energy ground state to a high energy excited state, usually within a femtosecond range ²⁵⁰. The absorbed energy is eventually exuded in the form of vibrational relaxation (top red squiggly lines Figure 4) and light, namely the fluorescence emission light captured by the microscope detector. The fact that both excitation and emission wavelengths are different, is key to fluorescence microscopy ²⁵⁰. In that sense it facilitates their distinction and allows for both of them to be separated by specific filters (i.e. the light that is used to excite a sample can be separated from the light that is emitted from it). By blocking the exciting light and only allowing the emitted light to come through the binoculars, the specimen is made visible to the eye without any background fluorescence. While confocal microscopy works with single-photon excitation, two-photon microscopy, as the name implies, needs two-photon excitation (see also Jablonski diagram and comparison of both techniques in Figure 4). This means that a fluorescent molecule is excited by absorbing light via 2 photons of the same energy at the same time, instead of just 1 photon (see Figure 4) ^{235,251-253}. Both photons carry less energy than the single photon (and therefore typically come from the near-infrared spectral range ²³⁵), but combined, and being absorbed by the fluorescent molecule (almost) simultaneously, have the same energy it takes to lift up the molecule to its excited state by a single photon (see Figure 4). Consequently, the chance of absorption for both photons is

proportional to the squared intensity of the excitation light, i.e. there is a non-linear dependence between the signal intensity and the intensity of the excitation light. In turn the light shone on the specimen is confined to a single defined and small volume in the focal plane and virtually no other molecules outside of this volume are excited and will create relevant signal (see Figure 4) ²⁵¹.

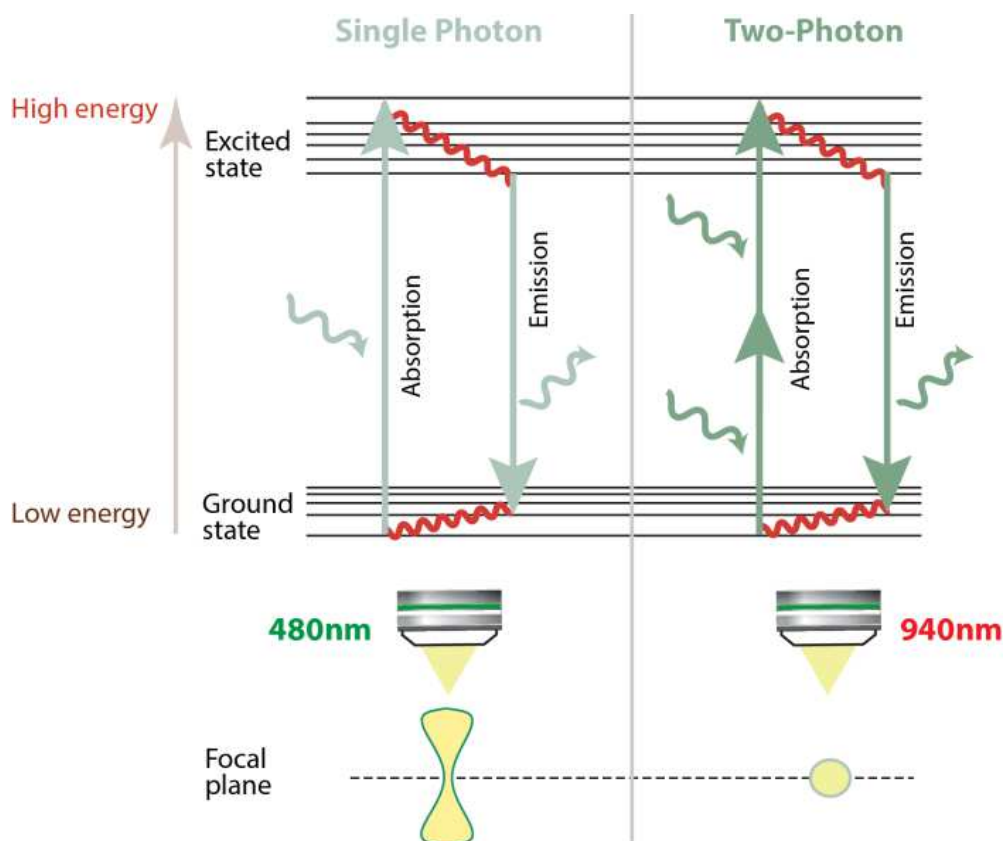


Figure 4. Concept of single and two-photon excitation microscopy illustrated by Jablonski diagrams. Both single and two-photon excitation is based on the concept of fluorescence: A fluorescent molecule hereby absorbs energy in the form of photons and is thus elevated into a high energy “excited” state. The molecule will shed the absorbed energy within a specific time and in the form of a.) vibrational energy (or other forms of energy that are not light; red squiggly lines) and b.) emitted light energy (“emission”). The emitted light is generally of a smaller wavelength than the wavelength of the absorbed light, creating a possibility to separate the two events. In contrast to two-photon excitation, single photon excitation is based on the principle, that the fluorescent molecule absorbs only one single photon in order to be catapulted to the energetically higher excited state. Therefore signal production is linearly dependent on the excitation intensity and shorter but energetically higher wavelengths (ultraviolet/blue/green spectral range) are used for excitation. In addition single photon excitation will produce a big cone of light shining through the whole specimen, which in turn requires a pinhole to filter out light that is out-of-focus. Two-photon excitation on the other hand works by the principle, that two photons of the same energy are absorbed quasi simultaneously to produce the same energy needed to elevate the fluorescent molecule from the ground to the excited state. As a consequence photons can have a lower energy, because they only work in combination to create enough energy, and excitation light is thus usually in the near infrared range. Additionally there is a non-linear dependence between the signal intensity and the intensity of the excitation light and only a small defined volume in the focal plane is excited. This leads to little out-of-focus excitation. Adapted from Helmchen & Denk, 2005 and Mostany et al., 2014 ^{251,254}

Furthermore, almost (near) simultaneous absorption of 2 photons is quite a rare event. In order to create an opportunity of two photons being absorbed, while keeping the intensity at a tolerable level for the specimen, lasers emitting ultra-short (femtosecond range) but intense pulses are used ^{251,252}. Today titanium-sapphire (Ti:sapphire) lasers are mostly used (as was done in this thesis) ²⁵¹. Their excitation wavelength span a significant spectral range (670–1080 nm) and therefore facilitate the imaging of many different fluorophores ^{251,252}. Finally, for two-photon and confocal microscopy, the light emission of the fluorescent molecules follows the same mechanism ^{235,251} (see Figure 4).

In comparison to confocal microscopy, two-photon microscopy harvests many advantages: Firstly, two-photon microscopy allows for a much deeper tissue penetration. Normally, when the excitation light enters tissue, its path out of the tissue will be scattered by heterogeneous refraction indices within the tissue. This can cause a blurry image since the scattered light will not come from the focal plane but may still be detected in the microscope setup ²⁵³. Scattering of light becomes a bigger problem with increasing tissue depth ²⁵¹. Here the fact, that two-photon microscopy normally employs excitation light near the infra-red spectral range (approximately double the single photon excitation wavelength ²³⁵) is advantageous as these wavelengths penetrate tissue with less scattering effects, in parts due to less absorption of endogenous chromophores ^{235,253}. In addition the excitation light from two-photon microscopes is gathered onto a small and confined volume (and therefore presents less risk of more tissue mass causing scattering and visualization of out-of focus scattering). Even if some light were to be scattered in that focal plane, these scattered photons would be too little in number to cause significant fluorescence emission and thus creates less out-of-focus excitation artefacts ²⁵³. This enables the experimenter to sharply image tissue depths between 500-800 μm ^{251,252,255}. Finally, two-photon microscopy is associated with less phototoxicity/photodamage within the imaged tissue. Excitation wavelengths at the near infra-red level have less energy and thus less power to be harmful. Further, the fact that only a small volume is excited at a time, also leads to less tissue damage in total.

Overall, two-photon in vivo microscopy has many assets in comparison to other imaging techniques like confocal microscopy. In addition it readily facilitates the visualization of dynamic processes, like spine formation/elimination in the same neurons in real-time (and not just as fixed snapshots), allowing for the precise

analysis of how the same spines act over time ^{97,103}. Thus this microscopy technique proved the best choice of imaging method for this thesis.

1.7. Tracing neurons in the brain

Throughout the years there have been many techniques to visualize neuronal morphology and neuronal networks within the brain. These techniques range from using molecular tracers to viruses, but generally follow the same principle. In order to function, neurons need to and can take up different molecules from their surroundings and transport them via microtubules to either their soma or axon terminal, depending on the use of the molecule ^{256,257}. Tract tracing, takes advantage of this need and lets neurons take up particles which will then get transported towards their respective target destination. Two forms of tracing exist: Retrograde and anterograde. Retrograde tracing functions through axonal transport from the axon terminal to the soma and thus serves to contextualize where the cell bodies of afferent fibres originate from ^{256,257}. Conversely, anterograde transport is established by transporting particles from the soma to the axon terminal and thus helps identify to which structure particular cells project to ^{256,257}. Both principles were employed in this thesis, in order to visualize the anatomical location and projection patterns of TCN, as well as to elucidate their overall circuit connectivity in the healthy and injured brain.

1.7.1. Neuroanatomical tracing using fluorescent dyes and markers

Early techniques of tracing neuronal circuits and their anatomical origin, usually employed fluorescent substances, like dye particles. One of the first such dyes was Evans Blue dye ²⁵⁶, which was quickly replaced by an array of other useful fluorescent dyes that are just big enough of a molecule to be transported retrogradely to the cell soma. These dyes include Fast Blue, Lucifer Yellow, FluoroEmerald, FluoroRuby, fluorescent beads (RetroBeads), cholera toxin beta subunit b (CTB) and last but not least Fluorogold (FG) ²⁵⁶⁻²⁵⁹. FG, which was used in this dissertation, has been widely employed as a retrograde tracer ^{178,260,261}. It is essentially a weak base that is taken up by the axon through passive uptake ^{256,262} and fluorescently emits light after UV-light excitation ^{258,262}. In this respect FG can for example label the soma, as well as dendrites of the neuron ²⁶⁰, while RetroBeads usually just mark the soma ²⁵⁸. On the other hand, anterograde dye molecules can encompass crystal-like lipophilic carbocyanine dyes, plant lectins, CTB and finally biotinylated dextran amine (BDA) ^{256,257,263}. Of these, BDA has proven to be a

reliable and widely used (mostly) anterograde tracer ^{178,264,265} and was thus also utilized in this dissertation. As the name tells, BDA is a dextran amine molecule that does not disintegrate for up to 4 weeks in the brain, and gets taken up by the cell body by a yet unknown mechanism ²⁵⁷. In contrast to other dextrans it does not have inherent fluorescent properties, and requires immunohistochemical procedures for detection ²⁶³. Each of those tracers is usually inserted into the region of interest by careful injection into the brain with a micropipette ²⁵⁶, or in the case of crystals by depositing them in the tissue ²⁶³. For each experiment, the experimenter has to allow enough time for the marker to be taken up and subsequently be transported to its anatomical target location ²⁵⁸.

1.7.2. Viral tracing techniques

In recent years the above mentioned techniques to trace the origin, projection pattern and distribution of cells have been complemented with viral labelling techniques. Here the ability of viruses to infect and be taken up by neurons (i.e. neurotropism) is exploited to label neurons and their projections. After infection the virus travels to the cell nucleus and starts replicating, thus creating new copies of it to infect other neurons ²⁵⁷. Under experimental conditions injection of viral vectors into CNS tissue leads to the expression of “temporarily and spatially controlled genes of interest” (Aschauer et al., 2013, p.1 ²⁶⁶), which are commonly the genes for the expression of a fluorophore, such as green-fluorescent protein (GFP).

1.7.2.1. Adeno-associated viruses

In that sense (recombinant) viral vectors originating from adeno-associated viruses (AAVs) have been heavily used for neuronal tracing and labelling and/or gene transfer ^{178,267,268}. An AAV is single-strand DNA virus, without an envelope, that is part of the *paroviridae* family ²⁶⁶. One of their greatest advantages is the fact that they highly express desired genes for a long period of time, create only slight inflammation and are considered to be non-pathogenic ²⁶⁶⁻²⁶⁸. Typically AAVs are used for anterograde labelling and tracing of neurons. However, several experiments have demonstrated that they have retrograde transport capacities as well and can be used for retrograde tracing or gene delivery ^{267,269,270}. That said we employed the capacity of AAVs to precisely and retrogradely tag TCN with fluorescent proteins and trace them in the brain to our advantage in this thesis.

1.7.2.2. Mono-synaptic rabies virus tracing techniques for neuronal circuit reconstruction

While all the techniques described above can be used to map projections and label anatomical locations of neurons, not many can actually provide explicit synaptic transfer and tracing between connected neurons, since they do not exclusively spread through single synapses^{271,272}. Hence, labelling of neurons, in the vicinity of two connected cells, that are themselves not synaptically associated with the two latter connected cells, cannot be excluded. On that note, the rabies virus in particular has been shown to overcome some of those limitations and has, over the years, been developed into a powerful and precise tool for actual poly-, and more interestingly, mono-synaptic circuit mapping. Characteristically it spreads only retrogradely between connected neurons and in only one direction^{272,273}. Spread to unconnected neurons is virtually not seen and thus facilitates the stepwise labelling of CNS circuits²⁷².

The rabies virus comes from the family of *rhabdoviridae* and is known to be very well adapted to survive and replicate in the CNS of a wide range of hosts^{271,272}. Once the CNS is infected, the virus is taken up by the axonal terminal and retrogradely transported to the neuronal soma²⁷². Once arrived in the soma, the virus hijacks the neuronal transcription machine and replicates its genome^{272,274}. These viral replicates are then extended to the dendrites and ultimately to the pre-synaptic axonal terminals of the next order neuron²⁷². Repetition of these cycles in each higher order neuron lead to the labelling of synaptically connected neurons in the neuronal circuit at hand²⁷². Further the rabies virus is a negative single-strand RNA virus with an envelope and a rather small genome²⁷¹⁻²⁷³. Its genome is more stable than other RNA viruses and external encoding entities can be added or replaced easily²⁷¹. What is more, the virus does not necessarily integrate into the host genome, which could lead to perturbation of normal transcription processes within the infected cell²⁷¹. As a whole these properties make the rabies virus an excellent candidate for tracing and neuronal labelling studies.

Moreover the kilobyte-sized genome only encodes a handful of proteins²⁷². One of those encoded proteins is the so called glycoprotein (G-protein). The G-protein is a host-cell derived envelope protein²⁷⁵ that is not essential to transcription of the virus genome but rather needed for trans-synaptic spread²⁷⁶. Manipulating the expression of this protein has lead to the improvement of poly-synaptic tracing (that may still be difficult to interpret as to what order labelled neurons have within a

circuit or how strongly connected they are ²⁷⁶), to more precise mono-synaptic tracing. Mono-synaptic tracing hence allows for the restriction of the rabies virus to exactly one synaptic step and thus the identification of two distinct synaptically connected neurons within a circuit (i.e. starting cell and first order pre-synaptic partner) ^{271,276}. To achieve this, Wickerhsam et al., (2007)²⁷⁷ modified the rabies virus genome by deleting the G-protein gene and replacing it with the gene for the expression a fluorescent protein (in this example enhanced green fluorescent protein (EGFP)) ^{276,277}. Such a modified virus is able to enter cells and replicate its genome in initial target cells, thus expressing EGFP and showing green fluorescence under the microscope, but lacks its component to spread to its pre-synaptic partner, because the glycoprotein is missing ^{276,277}; see also Figure 5, A. For further reference this modified virus will be termed RABV-ΔG. In order to promote trans-synaptic spread between two singular neurons, Wickersham and colleagues (2007) then complemented the missing G-protein by “externally” adding it to the initially infected cells ²⁷⁶. As a result the virus in the initial cell can deliver its genome to its first-order synaptic partner, but in turn can not spread to any other synapse down the line because the genes for G-protein expression are missing in the first-order pre-synaptic partner ²⁷⁶; see also Figure 5, B. In addition Wickersham and colleagues (2007) set out to limit initial viral infection to a specific target cell population ²⁷⁶. For this purpose they added another key element to their technique, namely pseudotyping the viruses’ envelope protein for cell selective infection. Instead of coating it with its regular envelope, that allows the rabies virus to infect mammalian neurons, they encased the viral core with the avian envelope protein of the subgroup A avian sarcoma and leukosis virus (ASLV-A), termed EnvA ²⁷⁶. This specific envelope protein can only dock onto an avian viral receptor, termed TVA, which itself is only present in birds but not mammals ²⁷⁶. Hence mammalian neurons that do not express this receptor, but rather still have their intrinsic mammalian virus receptors, will not be able to be infected by the modified pseudo-typed rabies virus ²⁷⁶. As a result experimenters can engineer their desired target cell population to ectopically express TVA and ensure selective infection of a specific cell population ²⁷¹. In combination with G-protein deletion this manipulated rabies virus, lacking G-protein and added exogenous avian envelope is further referred to as RABV-ΔG-EnvA. Thus, only a neuron selectively modified to express TVA and externally complemented with G-protein, will be infected by RABV-ΔG-EnvA. Subsequently the rabies virus will, by G-protein complementation, be able to trans- and mono-synaptically spread to another neuronal partner but not further (see also Figure 5, C).

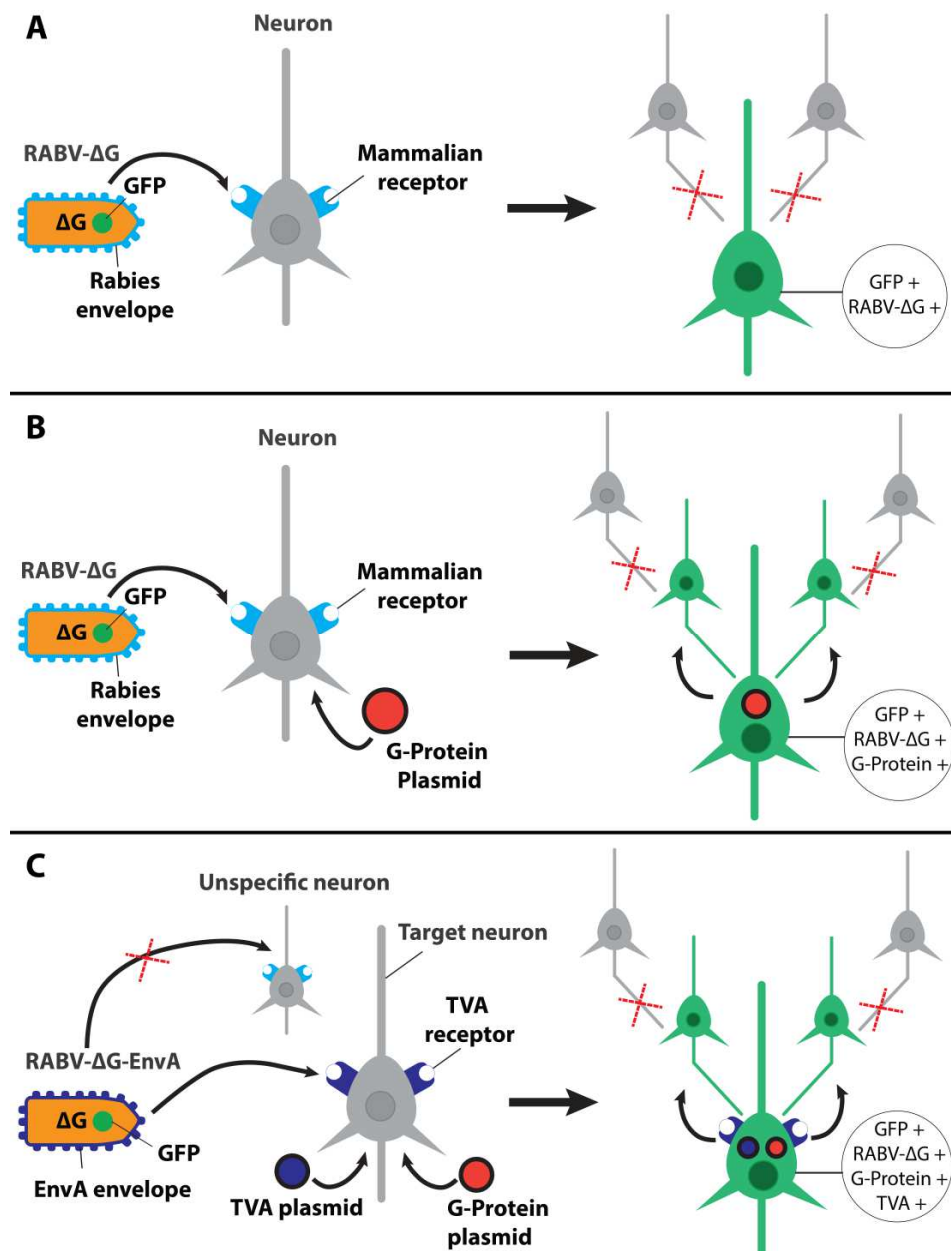


Figure 5. Principles of mono-synaptic rabies virus tracing techniques. A. Modified rabies virus without G-Protein complementation. Deletion of the G-protein in the rabies virus genome (RABV- Δ G) and replacing it with genes for the expression of fluorescent proteins (here GFP) allows the rabies virus to infect neurons, but prohibits it to trans-synaptically spread to connected neurons, since the G-protein is pivotal for this function. Initially infected populations will emit green fluorescence under a microscope. **B. Modified rabies virus with G-Protein complementation.** Deletion of the G-protein in the rabies virus genome (RABV- Δ G) and replacing it with genes for the expression of fluorescent proteins (here GFP) allows the rabies virus to infect neurons. External complementation of the G-protein in the target neuron facilitates trans-synaptic spread to neurons in direct synaptic contact. However, the G-protein is not present in the synaptic partners anymore and thus trans-synaptic spread is stopped at the first order synaptic partner. Infected cells will emit green fluorescence under a microscope, since the G-protein was replaced by GFP-expressing genes. **C. Pseudotyped rabies virus with G-Protein deletion for subtype specific targeting of cells.** In addition to G-Protein deletion, native rabies virus is pseudotyped with an envelope protein (EnvA) that can only bind to an avian receptor type (TVA receptor) that is not present in the mammalian CNS. Additionally neurons of interest are engineered to express only TVA receptors on their surface, thereby hindering pseudotyped rabies virus to infect unspecific neurons without that receptor. Complementation of the G-Protein in the target neuron, promotes trans-synaptic spread to neurons in direct synaptic contact. Nevertheless, the G-protein is not present in the synaptic partners anymore and thus trans-synaptic spread is

(*Figure 5 legend continued*) stopped at the first order synaptic partner. Infected cells will emit green fluorescence under a microscope, since the G-protein was replaced by GFP-expressing genes. Uptake location of the virus at the cell soma is not accurate, but was chosen for easier illustrative purposes. Adapted from Wickersham et al., 2007 ²⁷⁶

This mono-synaptic tracing technique has since then been improved and used multiple times to identify connections to single neurons ^{278–282} and was adjusted for our purposes in this thesis to study circuit connectivity of TCN after TBI (see Materials & Methods for more details).

1.8. Aims of this thesis

Previous research has sought out to elucidate how the brain reacts to TBI and study its ability to recover from the injury by making use of the plasticity in uninjured brain regions. In relation to this, the overall goal of this thesis was to understand how seemingly intact areas of the contralesional cortex react to TBI on a structural level (i.e. their spine dynamics) and find out whether they exhibit circuit changes following TBI. For this purpose TCN were studied in more detail, as they make up the biggest highway of anatomical connection between the two cerebral hemispheres and have thus been of great interest for their potential of mediating functional recovery after injury through structural plasticity.

As a whole this thesis was structured into 3 distinct aims:

1. The first aim constituted in creating a solid characterization of TCN in the intact mouse brain, in order to have a detailed understanding of their distribution and location throughout the cortex. In that sense the primary interest was to examine i.) if TCN are organized homotopically throughout distinct regions in the cortex, ii.) in which cortical layers TCN cell bodies and their projections are located within the contralateral cortical column and iii.) whether their distribution pattern varies depending on which brain area they reside ¹⁷⁸ (see also Figure 6, A).
2. The second goal of this thesis was to investigate if and how TCN in the spared hemisphere structurally change following TBI. In more detail, the objective lied in investigating the spine dynamics of a general neuronal population and later specifically TCN, in the contralateral (intact) hemisphere of the mouse cortex after TBI using longitudinal in vivo two-photon microscopy (see Figure 6, B). To complete the purpose, TCN spine dynamics

were further compared to spine behaviour in a population of neurons that is not directly connected to the injured cortex, namely CST neurons.

3. The third and final aim of this thesis was to determine whether TCN in the contralateral (non-injured) cortex undergo circuit changes or circuit remodelling following TBI, by making use of the above mentioned mono-synaptic rabies virus tracing technique (see Figure 6, C).

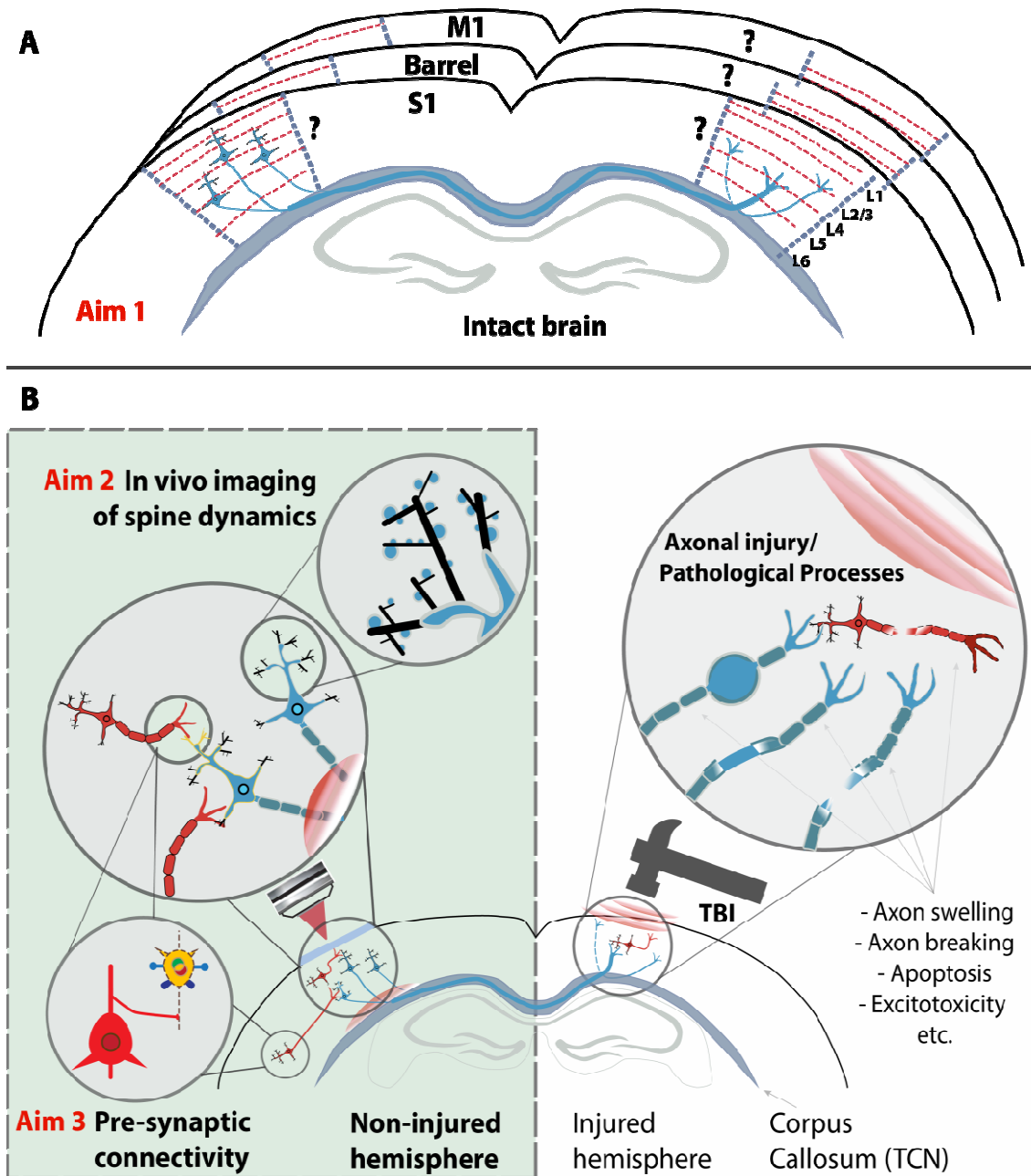


Figure 6. Illustration of thesis aims. A. Aim 1. Descriptive study of layer specific distribution and homotopic location of TCN somata and projections throughout distinct regions of the intact mouse brain (published in Chovsepian*,Empl* et al., (2017) ¹⁷⁸. **B. Aim 2 and 3.** Investigation of the influence of TBI on spine dynamics and circuit connectivity of TCN in the intact contralesional hemisphere following TBI using two-photon in vivo microscopy and mono-synaptic rabies virus tracing.

- MATERIALS & METHODS -

2.1. Tables of materials and methods

2.1.1. Disposable materials & tools

Syringes & needles	BD Plastipak™ hypodermic slip syringe 1ml (syringe for injections of anaesthetic and saline) Injekt® 5 ml Luer, non-sterile syringe (syringe to spread ringer lactate solution on sugi swabs or skull/brain) Sterican 30G (0.3×12) (needles, for injections of anaesthetic/antagonist and saline)	Becton Dickinson & Co., New Jersey, USA Braun Medical Inc. Bethlehem, Pennsylvania, USA B. Braun Melsungen AG, Melsungen Germany
Surgery materials & tools	Vannas-Tübingen spring scissors Vannas spring scissors - microserrated Vannas spring scissors - 2mm Cutting Edge Noyes spring scissors Dumont #5 forceps Dumont #3 forceps Feather stainless steel blade (disposable surgical blade) Sugi (absorbent triangle swabs) Ethicon Spongostan (hemostatic swabs) Ethicon Ethilon™ monofil 6-0 size (skin suture) NaCl 0.9% (sterile saline solution, for subcutaneous injection for hydration of animals after surgeries) Ringer lactate solution Cover glass 4mm diameter (CS-4R) 3M™ Vetbond™ (tissue adhesive) Histoacryl® (cyano-acrylate tissue adhesive) Paladur® (dental cement) Metal head bar (for fixation of mouse under two-photon microscope)	Fine Science Tools GmbH, Heidelberg, Germany Fine Science Tools GmbH, Heidelberg, Germany PFM Medical AG, Cologne, Germany Kettenbach GmbH & Co. KG, Eschenburg, Germany Johnson & Johnson Medical GmbH, Norderstedt, Germany Johnson & Johnson Medical GmbH, Norderstedt, Germany B. Braun Melsungen AG, Melsungen Germany B. Braun Melsungen AG, Melsungen Germany Warner Instruments, Connecticut, USA 3M, Minnesota, USA B. Braun Melsungen AG, Melsungen Germany Kulzer GmbH (Heraeus), Hanau, Germany Custom-Made, Biomedical Center workshop, LMU, Munich, Germany

	<p>Diamond drill burs 801, 008 (injection surgery)</p> <p>Stainless steel drill burs HM1 005 (cranial window surgery)</p> <p>Imaging head-fixation device</p> <p>Blaubrand intraMark micropipettes 5µl (Pulled glass pipette)</p> <p>Bepanthen Augen- und Nasensalbe 5g (eye cream)</p>	<p>Hager & Meisinger GmbH, Neuss, Germany</p> <p>Hager & Meisinger GmbH, Neuss, Germany</p> <p>Custom-made, Biomedical Center workshop, LMU, Munich, Germany</p> <p>Brand GmbH & Co KG, Wertheim, Germany</p> <p>Bayer, Leverkusen, Germany</p>
Immunohistochemistry (IHC), microdissection, cutting & mounting of brain tissue	<p>Standard round paint brush (4 and 6mm diameter; for mounting of brain sections on slides)</p> <p>Precision brain slicer (adult mouse 30gm, coronal)</p> <p>Tissue-Tek® O.C.T. Compound (optimal cutting temperature freezing medium, to embed brain tissue before cutting on cryostat)</p> <p>Tissue-Tek® Cryomold® intermediate mold (Tissue mold, acting as a receptacle for brain tissue before cutting on either the cryostat or vibratome)</p> <p>Loctite 408 glue (used to glue and stabilise agarose embedded brain tissue on vibratome fixture)</p> <p>Cell culture well plates Costar® (for free floating staining procedure)</p> <p>Menzel™ microscope slide 76x26mm,</p> <p>Menzel™ microscope cover slips 24x60mm</p> <p>VectaShield® mounting medium</p> <p>Standard clear nail polish (to seal of mounted and coverslipped brain sections)</p> <p>Pipettes, pipette tips and tubes/receptacles</p>	<p>Art supply store</p> <p>Braintree Scientific, Inc., Massachusetts, USA</p> <p>Sakura® Finetek Europe B.V., Netherlands</p> <p>Sakura® Finetek Europe B.V., Netherlands</p> <p>Henkel Corporation, Düsseldorf, Germany</p> <p>Corning Incorporated, ME, SA</p> <p>Fisher Scientific as part of Thermo Fisher Scientific, Massachusetts, USA</p> <p>Fisher Scientific as part of Thermo Fisher Scientific, Massachusetts, USA</p> <p>Vector Laboratories, Inc., Burlingame, California, USA</p> <p>DM Drogerie Markt, Munich, Germany</p> <p>Eppendorf AG, Hamburg, Germany</p>

2.1.2. Reagents & chemicals

General	80% ethanol (disinfectant)	CLN GmbH, Niederhummel, Germany
Perfusion, post-fixation, IHC, cutting & mounting of brain tissue	Paraformaldehyde (PFA) powder	Sigma Aldrich, Chemie GmbH, Taufkirchen, Germany
	1M NaOH (pH-adjustment during PFA preparation)	Sigma Aldrich, Chemie GmbH, Taufkirchen, Germany
	1M HCL (pH-adjustment during PFA preparation)	Sigma Aldrich, Chemie GmbH, Taufkirchen, Germany
	0.2 M phosphate buffer (PB; for PFA preparation)	27.5 g Na ₂ HPO ₄ ·H ₂ O 35.5 g Na ₂ HPO ₄ ·2H ₂ O dH ₂ O ad 1L
	Heparin-Natrium 25.000IE (Heparin sodium) for perfusion	Ratiopharm GmbH, Ulm, Germany
	Sucrose (pre-treatment before cutting on cryostat)	Sigma Aldrich, Chemie GmbH, Taufkirchen, Germany
	Phosphate buffered saline (PBS) stock solution 10x, pH 7.4)	2.6 g Na ₂ HPO ₄ (M=137.99g/mol) 14.4g Na ₂ HPO ₄ ·2H ₂ O (M=177.99g/mol) 87,5 g NaCl (Merck, Sigma-Aldrich) dH ₂ O ad 1L
	Triton X-100	Sigma Aldrich, Chemie GmbH, Taufkirchen, Germany
	Sodium azide (NaN ₃)	Sigma Aldrich, Chemie GmbH, Taufkirchen, Germany
	Gelatine (for subbing slides)	Sigma Aldrich, Chemie GmbH, Taufkirchen, Germany
Agarose (to embed brain before cutting on vibratome)	Sigma Aldrich, Chemie GmbH, Taufkirchen, Germany	
Goat serum (ICH)	Invitrogen GmbH, Darmstadt, Germany	
Dye buffer	Cacodylate buffer stock solution 1 L (arsenate buffer, pH 5-7.4)	0.2M Sodium Cacodylate (Na(CH ₃) ₂ AsO ₂ · 3H ₂ O): 42.8mg (Na(CH ₃) ₂ AsO ₂ · 3H ₂ O; Sigma) + ddH ₂ O ad 1L 0.2M Hydrochloride (HCl; for pH adjustment): 10ml HCl (Conc. 36-38%; Sigma) + 603ml H ₂ O

2.1.3. Tracers, viruses, antibodies

Tracers	Fluorogold	Fluorochrome LLC, Colorado, USA
	Biotinylated Dextran Amine (BDA) 10,000 MW	Thermo Fisher Scientific, Massachusetts, USA
Antibodies	Polyclonal chicken anti-GFP (ab13970)	Abcam, Cambridge, UK
	Goat Anti-Chicken Alexa Fluor® 488	Abcam, Cambridge, UK
Nissl stain	NeuroTrace 435/455 (Blue fluorescent Nissl stain)	Invitrogen GmbH, Darmstadt, Germany
Viruses	Retrograde AAV, AVV-CAG-GFP (37825-AAVrg; Titer $\geq 5 \times 10^{12}$ vg/mL)	Addgene, Massachusetts, USA
	AAV1.hSyn.Cre.WPRE.hGH (AV-1- PV2676; titre: 5.048×10^{13} vg/ml)	Penn Vector Core, Gene Therapy Program, University of Pennsylvania, USA
	AAV1- synP-DIO-sTpEpB-eGFP (AV6118CD; titre: 3.9×10^{12} GC/ml)	Gene Therapy Center Vector Core, University of North Carolina, USA
	Rabies virus, SAD- Δ G-mcherry (EnvA); (titre: 3×10^8 ffu/ml); dilution 1:1 in 1x PBS)	Gene Center of the LMU, Laboratory of Prof- Karl-Klaus Conzelmann, Munich, Germany

2.1.4. Medication

Analgesics	Metacam (1.5 mg/ml oral suspension)	Boehringer Ingelheim Intl. GmbH, Ingelheim am Rhein, Germany
	Temgesic 0.324mg (Buprenorphine hydrochloride)	Reckitt Benckiser GmbH, Heidelberg, Germany
MMF	Midazolam 5mg	Ratiopharm GmbH, Ulm, Germany
	Cepetor 1mg (Medetomidine hydrochloride)	CP-pharma GmbH, Burgdorf, Germany
	Fentanyl 0.05mg	B.Braun AG, Melsungen, Germany
Antagonist	Revertor 5mg (Atipamezole hydrochloride)	CP-pharma GmbH, Burgdorf, Germany
	Flumazenil 0.1mg	Hameln GmbH, Hameln, Germany
	Naloxon 0.4mg (Naloxone hydrochloride)	B.Braun AG, Melsungen, Germany
Other	Isofluran CP (Isoflurane, anaesthesia perfusion)	CP-pharma GmbH, Burgdorf, Germany

2.1.5. Technical & imaging devices

Surgery devices	K.1070 High Speed Rotary Micromotor Kit (drill Kit)	Foredom, Blackstone Industries Inc., Connecticut, USA
	T/Pump System Localized Warming and Cooling Therapy (heating pad)	Gaymar Industries, New York, USA
	P-30 Vertical Micropipette Puller	Sutter Instruments, Science Products GmbH, Hofheim, Germany
	TBI-0310 impactor & stereotactic frame	Precision Systems & Instrumentation, LLC, Virginia, USA
	Just for Mouse™ stereotactic instrument & Lab Standard™ stereotactic mouse frame	Stoelting, Illinois, USA
	Wella Contura W7807 (hair trimmer)	Wella, Darmstadt, Germany
Perfusion	Ismatec IP high precision multichannel pump (perfusion pump)	ISMATEC SA, Labortechnik-Analytik, Glattbrugg, Switzerland
IHC, cutting devices	Vortex-Genie 2 (vortex)	Scientific Industries Inc, Bohemia, USA
	Polymax 1040 (shaker)	Heidolph Instruments GmbH, Schwabach, Germany
	Vibratome (Leica VT 1000S vibratome)	Leica Microsystems GmbH, Wetzlar, Germany
	Cryostat (Leica CM1850)	Leica Microsystems GmbH, Wetzlar, Germany
Microscopes & objectives	Olympus Stereo Microscope SZ51	Olympus GmbH, Hamburg, Germany
	Olympus FV1000 confocal microscope	Olympus GmbH, Hamburg, Germany
	Leica SP8 confocal microscope	Leica Microsystems GmbH, Wetzlar, Germany
	Leica DM4 B upright light microscope	Leica Microsystems GmbH, Wetzlar, Germany
	Olympus FV1000 MPE two-photon microscope with Mai Tai DeepSee femto-second pulsed Ti:Sapphire laser (SpectraPhysics)	Olympus GmbH, Hamburg, Germany
	Olympus, 10x/0.4, air immersion objective/ x20/0.85 oil immersion objective (for Olympus FV1000 confocal microscope)	Olympus GmbH, Hamburg, Germany
	Leica 10x/.45 HC PL APO, 20x/0.75 Imm Corr CS2, 40x/1.30 HC PL APO (for Leica SP8 confocal)	Leica Microsystems GmbH, Wetzlar, Germany
	Leica 2.5x/0.07 HC PL Fluotar (for DM4 microscope)	Leica Microsystems GmbH, Wetzlar, Germany
	Olympus XLPlan N 25X/1.05 W MP objective (for Olympus FV1000 MPE)	Olympus GmbH, Hamburg, Germany

2.1.6. Software

Fiji (ImageJ)	General Public License, https://imagej.nih.gov/ij/download.html
Adobe Creative Suite CS6 (Photoshop, Illustrator)	Adobe Systems, Inc., San Jose, California, USA
MBF Stereo Investigator software (stereology software)	MBF Bioscience, Vermont, USA
Olympus software FluoView FV10- ASW 4.0	Olympus GmbH, Hamburg, Germany
GraphPad Prism 7.01 for Windows,	GraphPad Software, La Jolla, California, USA

2.2. Animals

A total of 76 mice, both C57/Bl6 and transgenic Thy1-GFP-M mice, aged between 6 and 12 weeks were used for this study. All animals were housed under controlled standard housing conditions and each animal experiment was carried out in accordance with German animal welfare guidelines and previously authorized by the local regulatory committees under the protocol number AZ:55.2.1.54-2532.135-15.

Of those 76 mice, 32 C57/Bl6 mice were analyzed, to characterize the distribution of TCN throughout the intact murine cortex¹⁷⁸, while a total of 35 C57/Bl6 and 4 Thy1-GFP-M mice²³⁸ were used to characterize the spine plasticity and circuit connectivity of neurons in the injured brain. In the initial phase of the study, we also performed our injury paradigm on 5 C57/Bl6 mice, in order to establish injury parameters that create a reproducible and comparable lesion volume for all the animals throughout the whole study. More precisely, for in vivo experiments, which were carried out to determine whether spine density and turnover change in the non-injured cortical hemisphere, a total of 13 mice were used. In particular, we analyzed 4 Thy1-GFP-M mice²³⁸, in order to elucidate possible changes in spine plasticity after TBI, based on a population analysis. GFP-M mice have sparse labelling, with few cells expressing green-fluorescent protein (GFP) in the cortex, mostly in layer V²³⁸. To analyze to what extent spine dynamics and turnover may change after TBI in the non-injured cortex, *specifically* in a transcallosal population of neurons, a total of 3 C57/Bl6 mice was used. In addition spine dynamics were investigated in a “control” population of corticospinal tract (CST) neurons in 6 C57/Bl6.

Lastly, we set out to investigate circuit connectivity of TCN in the contralateral hemisphere of the injury site. Here, a total of 26 C57/Bl6 mice were divided into 3 different groups: While two groups were created to investigate the status of the TCN circuit at 7 and 42 days following TBI (early time-point group: 7 days post injury (dpi), n= 6; late time-point group: 42dpi, n=8), a control group of 12 mice without injury was established (pooled animals under control conditions, for early (7dCTRL, n= 6) and late time-points 42dCTRL, n=6).

For a detailed description of the number of animals used in each experimental paradigm, see Table1 below.

Experiment	Number of animals	Genotype
Descriptive study of TCN ¹⁷⁸	32	C57/Bl6
Lesion reproducibility	5	C57/Bl6
In vivo two-photon imaging of spine dynamics of the non-injured cortex (population based analysis)	4	Thy1-GFP-M mice ²³⁸
In vivo two-photon imaging of spine dynamics of TCN in the non-injured cortex	3	C57/Bl6
In vivo two-photon imaging of spine dynamics of CST in the non-injured cortex	6	C57/Bl6
Circuit connectivity of TCN in the non-injured cortex	26 (7dpi: n=6; 42dpi: n=8; Controls: n=12)	C57/Bl6
Total	76	C57/Bl6 (n=72)/ Thy1-GFP-M mice(n=4)

Table 1: Summary of the number of animals and genotypes used in each experimental paradigm.

It should be noted, that we also employed 2 more C57Bl/6 mice to test the efficiency and specificity of our viral tracing technique (not shown in Table 1 and not counted in the total number of experimental animals).

2.3. Surgical procedures – General considerations

All surgical procedures began with induction of anaesthesia via an intraperitoneal (i.p.) injection of a mixture of Midazolam (5mg/kg bodyweight), Medetomidin (0.5mg/kg bodyweight) and Fentanyl (0.05mg/kg bodyweight), referred to as MMF hereafter. After checking for absence of a pedal reflex and confirming successful anaesthesia, hair on the head (or back/shoulder region for spinal cord injections) of the mouse was trimmed, in order to facilitate unobstructed access to the skull. Animals were fixed in their respective stereotactic frame (Stoelting Stereotactic Instruments, USA, unless otherwise specified) and their eyes kept moist throughout the surgery with eye cream (Bepanthen Augen- und Nasensalbe 5g, Bayer). Further the exposed area was disinfected and cleared of excessive hair with 80% ethanol on cotton pads. Thereafter surgical procedure varied depending on its aim. However, after completion of surgery all animals were injected with ~1ml of sterile saline solution (NaCl 0.9%, B. Braun Melsungen AG), to avoid fluid and electrolyte loss during surgery. Finally mice were antagonized (Antagonist-Mix: Atipamezol (2.5mg/kg); Flumazenil (0.5mg/kg); Naloxon (1.2mg/kg)) and left to wake up and recover from anaesthesia on a heating pad (38°C). Later they were treated with analgesic medication (Metacam 1.5 mg/ml oral suspension, Boehringer Ingelheim or an i.p. injection of Temgesic 0.1 mg/kg for surgeries that included TBI) for up to 2 days after surgery, unless otherwise stated.

2.4. Injury paradigm- controlled cortical impact

All TBIs were induced by CCI. After induction of anaesthesia animals were fixed in a specialized stereotactic frame (Precision Systems & Instrumentation, LLC). The skin on the skull was incised with a disposable surgical blade at the level of the sagittal suture and the resulting skin flap was pulled aside to expose one hemisphere of the skull completely. Thereafter the exposed skull was dried with a sugi swab (Kettenbach GmbH & Co. KG) and a rectangular craniotomy, between both the coronal sutures (and Lambda/Bregma, respectively) as well as the sagittal suture and the skull right above the temporal muscle, was generated under repeated cooling with saline (see Figure 7). The resulting bone piece was removed, exposing the brain. The injury to the brain was induced using the TBI-0310 impactor (Precision Systems & Instrumentation, LLC), in the area of the somatosensory cortex. Here, a pneumatically controlled rod of 3mm diameter was driven onto the brain at a velocity of 6m/s, a dwell time of 150ms and a depth of 0.3-0.5mm.

Directly after the impact, possible bleeding was cleared using sugi and spongostan haemostatic swabs (Johnson & Johnson Medical GmbH). The previously removed rectangular bone piece was re-positioned to its previous location and glued back to the skull with tissue adhesive (3M™ Vetbond™, 3M United States). The skin was sutured back together with Ethilon™ skin sutures. The above mentioned injury parameters (velocity: 6m/s, dwell time: 150ms, injury depth: 0.3-0.5mm) were carefully chosen for further experiments, in order to establish an injury that will create damage to the corpus callosum and its passing axonal fibres, but not advance into subcortical areas like the hippocampus. Thus, we created an “injury series” of our chosen parameters (n=5) to ensure that we could form a reproducible injury in depth and severity. For this purpose animals were sacrificed 3 days after injury and the lesion volume further characterized (for more details see later sections of Materials & Methods).

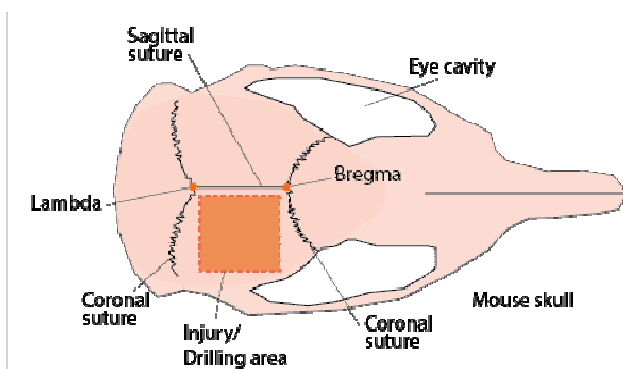


Figure 7. Illustration of mouse skull and area of craniotomy for CCI. A rectangular craniotomy (dashed orange rectangle) within the sagittal and the two coronal sutures, using Lambda and Bregma as two additional points of anatomical reference, was generated. CCI occurred within this rectangular area within the somatosensory cortex.

For animals that were already implanted with a CW (for more details see later sections of Materials & Methods), the skin tucked under the previously placed dental cement (Paladur®, Kulzer GmbH (Heraeus), Germany) was gently pulled out and incised perpendicular but central to the sagittal suture extending to the temporal muscle, prior to the craniotomy. In addition, remaining skin or tissue underneath the dental cement was cleaned and the entire skull dried with sugi swabs. To secure the CW, before induction of TBI, small amounts of tissue glue (3M™ Vetbond™, 3M United States) were distributed between skull and dental cement. After injury induction the skin was sutured back together and glued onto the skull closest to the dental cement of the CW, thus covering and sealing off the injured brain.

2.5. Viral & tracer injections

2.5.1 Characterization of transcallosal neurons in the intact mouse brain

In order to discern the distribution of TCN throughout the mouse cortex, we injected different retrograde and anterograde tracers into the cortex of uninjured mice. The retrograde tracer Fluorogold (FG; 1% in 0.1 M Cacodylate buffer, Fluorochrome LLC) was injected to describe the location and distribution of transcallosal projection neurons in the primary motor cortex, the primary somatosensory cortex, outside and inside of the barrel cortex area ¹⁷⁸. In contrast, we used biotinylated dextran amine (BDA 10,000 MW; Life Technologies; ^{265,283,284}) to characterize the axonal terminal fields of TCN in the primary somatosensory cortex ¹⁷⁸. After exposing the skull and cleaning it with sugi swabs, a small hole was gently drilled into the mouse skull and a thinly pulled glass micropipette was inserted at specific stereotactic coordinates. For each experimental question, either 1.5µl of BDA (coordinates from Bregma: -1.5 mm; 1.7 mm lateral; 0.3 mm depth to target layers II/ III and 0.6 mm depth to target layer V) ¹⁷⁸ or 0.5µl of FG (coordinates with respect to Bregma: rostro-caudal +0.3 mm and -1.5 mm, lateral 1.3 mm, depth 0.3 mm; rostro-caudal +0.3 mm and -1.5 mm lateral 1.7 mm, depth 0.3 mm and rostro-caudal, +0.3 mm and -1.5 mm, lateral 3.5 mm, depth 0.3 mm), were slowly injected through the micropipette into the brain tissue. All animals were sacrificed 10 days post-surgery, in order to ensure that the tracer has enough time to travel efficiently to its target location ¹⁷⁸.

2.5.2. In vivo investigation of transcallosal neurons in the non-injured contralesional cortical hemisphere

For in vivo experiments employing two-photon microscopy, TCN and CST neurons were also selectively traced and labelled through viral vectors. In particular, we first injected mice with a retrograde adeno-associated virus (AAVrg; namely AVV-CAG-GFP, commercially available at Addgene, 37825-AAVrg; Titer $\geq 5 \times 10^{12}$ vg/mL) to retrogradely trace TCN and CST neurons respectively. In principle, viral injections for labelling of TCN were performed according to previously described protocols ¹⁷⁸ and above. In brief, animals were anaesthetized and placed in a stereotactic frame (Stoelting, USA). Their skull was uncovered and injected with 0.3-0.4µl of the AAVrg (AAV-CAG-GFP; 1:50 dilution in 1x phosphate buffered saline (PBS)), using a glass capillary micropipette. The injection coordinates were determined relative to Bregma (rostro-caudal of Bregma: -1.8; lateral of Bregma 2.0; 0.3mm depth), and corresponded to TCN in parts of the right somatosensory cortex. In addition, these

coordinates were selected to ensure that the centre of GFP-expression in TCN falls approximately in the middle of the CW. Thus, it would be located in the imaging area of the CW that would retain the most optimal imaging quality for a long period of time (less surgery induced inflammation; less bone re-growth). Four to 5 days later, CW implantation took place (for more details see Figure 9 in section 2.6. of Materials & Methods).

In the case of CST neurons, we selectively and retrogradely traced cortical neurons, by stereotactically injecting AVV-CAG-GFP into the ventral part of the dorsal columns of the spinal cord, as previously described in Jacobi et al., (2015) and Jacobi et al., (2014) ^{286,287}. Briefly, the skin above the spinal cord, a little under the shoulder bones, was cut open with a surgical blade. Muscle tissue was gently and carefully pulled aside to reveal the vertebrae. Consequently, a laminectomy was performed with fine scissors at thoracic level 8 of the spinal cord and 0.3-0.4 μ l AVV-CAG-GFP (1:5 dilution in 1x phosphate buffered saline (PBS)) was injected with the help of a thinly pulled glass micropipette located \pm 0,2 mm lateral from the spinal midline (and a depth 0.3 mm). Thus, CST neurons lying in layer 5 of the mouse cortex were retrogradely labelled. Only the side of the spinal cord which was opposite to the cortical hemisphere on which CWs were implanted, was injected. The virus was left to express and travel to the cortex for 17-18 days before CWs were implanted (for more details see Figure 9 in section 2.6. of Materials & Methods). All animals were sacrificed after the last imaging session.

2.5.3. Circuit connectivity of TCN after TBI

By using the mono-synaptic rabies virus tracing technique, we set out to elucidate whether TBI could elicit changes in the existing circuit of TCN in the contra- as well as ipsilesional side of the cortex. For this purpose, TCN axons on the ipsilateral side of the injury were first selectively infected with a cre-expressing AAV (termed AAV-cre from this point forward) and their cell bodies thereby retrogradely traced to the opposite hemisphere (see Figure 8, A and B). To this end 0.5 μ l of the AAV-cre (AAV1.hSyn.Cre.WPRE.hGH; titre: 5.048e¹³ vg/ml supplied by the Penn Vector Core; dilution 1:6 in 1x PBS) were injected, as described above. The injection coordinates were assigned relative to Bregma (rostral-caudal -1.5 mm, lateral 1.7 mm, depth 0.3 mm) and represent TCN in the somatosensory cortex. For early time-point groups (7dpi) 0.5 μ l of the helper virus AAV1-synP-DIO-sTpEpB-eGFP (shortened to AAV-TVA-G-eGFP; titre: 3.9x10e¹² GC/ml supplied by Gene Therapy Vector Core, University of North Carolina; dilution 1:4 in 1x PBS) was injected on

the same day, using the same coordinates as for AAV-cre, only in the opposite hemisphere. Thereby, axonal endings of cells would take up AAV-cre, which then travels homotopically and retrogradely to the opposite hemisphere. At the same time AAV-TVA-G-eGFP would infect TCN in the same hemisphere as its injection site. However, as AAV-TVA-G-eGFP is a cre-inducible virus, it would only exclusively infect TCN that also contain AAV-cre. In contrast, late time-point groups (42dpi) were injected with AAV-TVA-G-eGFP, in the same way as described above, only 35 days after AAV-cre injection (see Figure 8, A).

In a final step, pre-synaptic partners of TCN were visualized by injecting 1 μ l of a rabies virus (SAD- Δ G-mcherry (EnvA); titre: 3×10^8 ffu/ml supplied by Prof- Karl-Klaus Conzelmann from the Gene Center of the LMU; dilution 1:1 in 1x PBS) as described before (see Figure 8, A and B). The coordinates corresponded to the same injection site as the AAV-TVA-G-eGFP (relative to Bregma: rostro-caudal -1.5 mm, lateral 1.7 mm, depth 0.3 mm). This modified rabies-virus lacks its glycoprotein (G-protein). The latter however is necessary for the rabies virus to infect cells and jump one synapse to enter pre-synaptic partners of the initially infected cell. In this case, the missing G-protein is complemented in cells encompassing the AAV-TVA-G-eGFP, as the “G” in the name implies. Therefore the red m-Cherry-expressing rabies virus will only be able to enter cells that have also been infected by AAV-TVA-G-eGFP, as they are expressing the G-protein. In turn, TCN that contain AAV-cre, as well as both AAV-TVA-G-eGFP and the m-Cherry rabies virus will appear yellow under a fluorescence microscope and constitute the so-called starter cells (see Figure 8, A and B). Further, the rabies virus will only be able to mono- and trans-synaptically infect their pre-synaptic partners. These pre-synaptic partners will then only appear in red, as the only viral particles they can express come from the mCherry fluorophore in the rabies virus (see Figure 8, A and B). Furthermore, for early time-points, TBI was induced on the same day as AAV-TVA-G-eGFP injection, while animals in the late time-point group were injured two weeks after AAV-cre injection. In contrast early and late time-points in the control groups followed the same timeline, solely without TBI. Lastly, the rabies virus was always injected a week before sacrifice of the mice to decrease possible viral toxicity to an absolute minimum. In any case, animals for early time-points were sacrificed 21 days after the first surgery, while animals assigned to late time-points were sacrificed 56 days after the first surgery (see Figure 8, A).

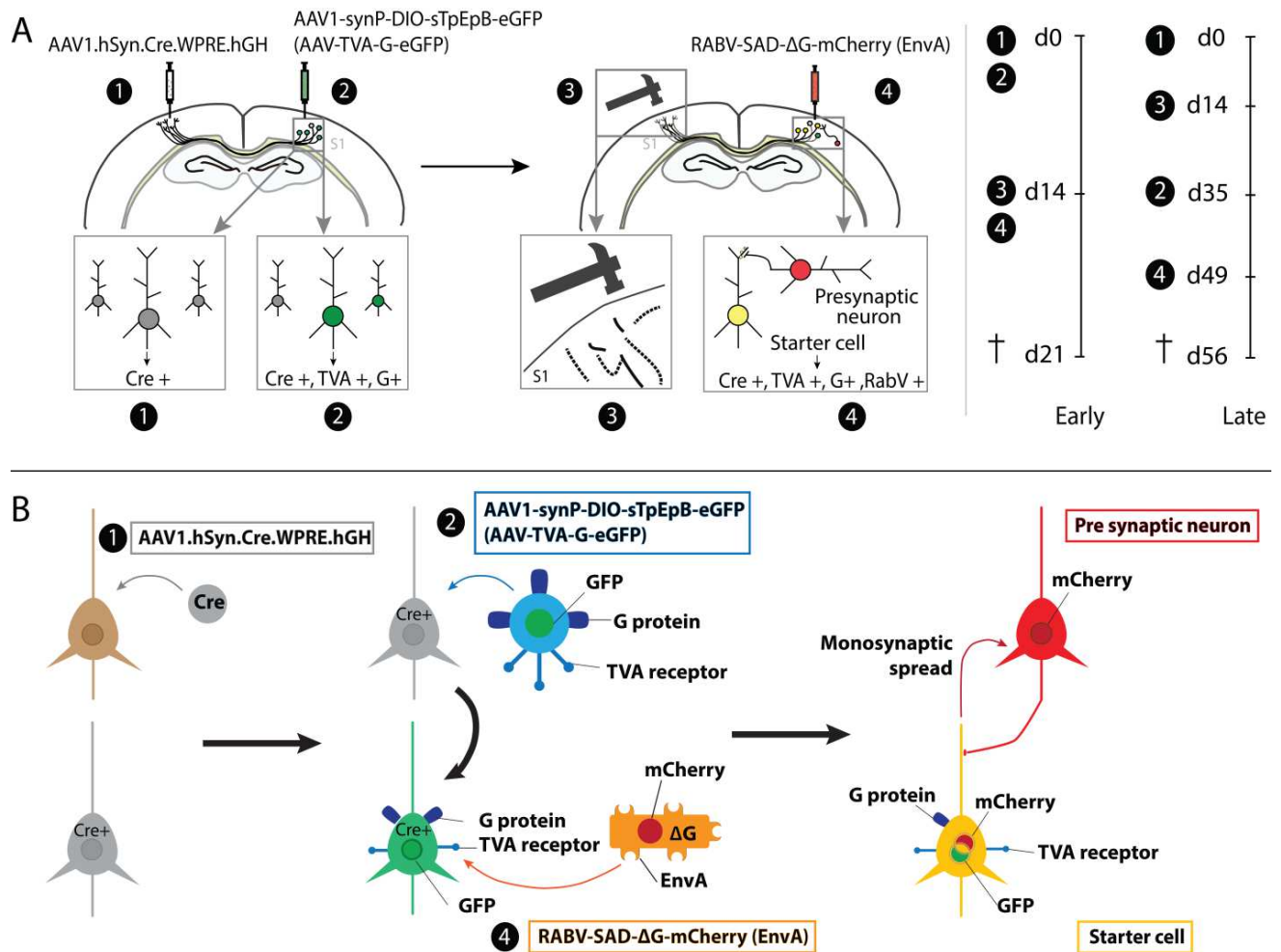


Figure 8. A. Schematic depiction of trans-synaptic circuit tracing and experimental timeline.

Animals were first injected with an AAV-cre virus (1: AAV1.hSyn.Cre.WPRE.hGH; grey cells = retrogradely labelled TCN). In order to facilitate monosynaptic tracing animals were also injected with a cre-dependent helper virus (AAV1-synP-DIO-sTpEpB-eGFP) in the opposite hemisphere of the AAV-cre injection (2: green cells = TCN, positive for the avian envelope protein TVA, the G-protein, cre and eGFP). For early time-points AAV-cre and AAV-TVA-G-eGFP injections were performed on the same day. In contrast for late time-points AAV-TVA-G-eGFP injection was performed 35 days after AAV-cre injection, in order to ensure comparable virus incubation times with animals in the early time-point group. While animals under control conditions did not undergo CCI, animals assigned to early and late time-points were injured two weeks after AAV-cre injection on the ipsilateral hemisphere of the AAV-cre injection site (3: dashed lines depict possible axonal damage resulting from the trauma). Finally, animals were also injected with the pseudotyped SAD- Δ G-mcherry (EnvA; RABV- Δ G-EnvA) rabies virus. The modified rabies virus can only infect TVA-positive cells and creates the so called starter cells (4: yellow cells). Through G-protein complementation it can then only spread across one synapse labelling the pre-synaptic partner of the starter cell (4: red cells). Animals were always sacrificed 7 days after injection of rabies virus (illustrated by a cross at d21 and d56 respectively).

B. Detailed illustration of mono-synaptic rabies virus tracing technique employed in this thesis.

A cre-expressing virus, which has the efficiency to retrogradely label TCN in the somatosensory cortex of the contralateral hemisphere to the injection site, was injected into the brain to selectively label TCN (1: brown neuron: non-labelled TCN; grey neuron: cre+-neuron after infection with the cre virus AAV1.hSyn.Cre.WPRE.hGH). Only the selected cre-positive TCN can in turn be infected by a cre-dependent helper virus (2: blue circular shape; virus name: AAV1- synP-DIO-sTpEpB-eGFP). The helper virus expresses the avian cell surface receptor TVA, as well as the G-protein and a green fluorescent protein (eGFP). Thus, cells positive for both AAV cre and AAV-TVA-G-eGFP will appear green under a fluorescent microscope (green neuron: expressing EGFP, G-protein and the TVA-receptor on its surface after infection with helper virus). Finally a specific modified rabies virus is

(*Figure 8 legend continued*) added (4: orange stick like figure; RABV-SAD-ΔG-mcherry (EnvA; RABV-ΔG-EnvA). This rabies virus is pseudotyped with the avian envelope protein (EnvA) and can only infect cells with its corresponding avian cell surface receptor TVA (see green cells). As a result the g-deleted, mCherry-attached and pseudotyped rabies virus will only selectively infect “green” cells and will create the so called starter cells (last step: yellow cells = starter cells). In addition, the pseudotyped rabies virus is complemented with its missing G-protein, through the presence of the helper virus. The G-protein is required for trans- and more importantly mono-synaptic spread and thus allows visualization of the first order pre-synaptic partners (see last step: red cells = pre-synaptic neurons of TCN starter cells). The first order pre-synaptic partner will in turn emit a red fluorescence since it has only internalized RABV-SAD-ΔG-mcherry (EnvA; RABV- ΔG-EnvA) particles, but lacks the G-protein to further infect other partners. Uptake location of the virus at the cell soma is not accurate, but was chosen for easier illustrative purposes. Modified from Callaway & Luo, 2015 ²⁷⁵

2.6. Chronic cranial window implantation

Before in vivo two-photon imaging, all animals were implanted with a chronic CW, following a slightly modified protocol by Holtmaat et al. (2012,2009) ^{248,249}. In more detail, mice were anaesthetized and fixed into a stereotactic frame and their eyes kept moist with eye cream (Bepanthen Augen- und Nasensalbe 5g, Bayer). Then, the skin above half of the skull was permanently removed with scissors. The exposed skull was gently cleaned and dried off with sugi swabs. The remaining skin, surrounding the exposed skull was glued to the sides of the skull with tissue adhesive (3M™ Vetbond™ tissue adhesive, 3M United States), in order to prevent fluid to exude from the covered part of the skull onto the uncovered part. In addition, a small amount of glue was spread on the uncovered skull, in order to keep it dry. After a short drying period, a scalpel was used to carefully scrape chequered ridges into the skull surface, in order to help stabilize the CW, as dental cement applied later adheres more easily to the ridges. Next, a circular shape in the size of a glass coverslip (4 mm diameter) was gently scratched into the skull, using the tip of a syringe. The location of the window was determined to be above the somatosensory cortex, in between both coronal sutures and lambda and bregma, respectively. Following this round “drawn template” a drill was used to carefully thin the bone until it was possible to remove the bone flap from the skull with forceps. The sagittal suture was kept intact by drilling approximately 1 mm away from it. Drilling was performed with regular breaks, little pressure and cooling of the area with saline or lactated ringer solution, so that damage or overheating of the brain underneath was minimized. After removing the bone flap the brain was kept moist by applying lactated ringer solution. In addition possible bleeding was stopped by placing a small gelfoam pad (Ethicon Spongostan, Johnson & Johnson), previously soaked in lactated ringer solution, on top of the exposed brain. When all bleeding subsided a 4 mm diameter glass coverslip was positioned on top of the

exposed skull and kept in place by applying gentle pressure on it with a toothpick fixed in the stereotactic frame. The glass coverslip was then glued and fixed onto to remaining skull, by applying another cyanoacrylate tissue adhesive (Histoacryl[®], B.Braun) on the edges of the glass. Special care was taken to prevent glue to leak onto brain tissue. Once the adhesive had dried, dental cement was placed on the remaining skull, as well as at the edges of the glass coverslip, thereby securing the coverslip further. The dental cement around the coverslip was applied in the form of a raised circle, thus creating a small reservoir to accommodate the water for immersion of the microscope objective later. The remaining skin on the side that was unaffected by CW surgery, was glued close to the edge of the dental cement, and slightly covered by dental cement as well. After the surgery, a resting period of at least 2 to 3 weeks before starting the imaging procedure was respected (see Figure 9). Hence, possible inflammation caused by the surgical procedure could subside. Further, two baselines measurements (i.e. without TBI) of spine dynamics parameters for each experimental condition were performed (TCN and CST neurons respectively; see Figure 9).

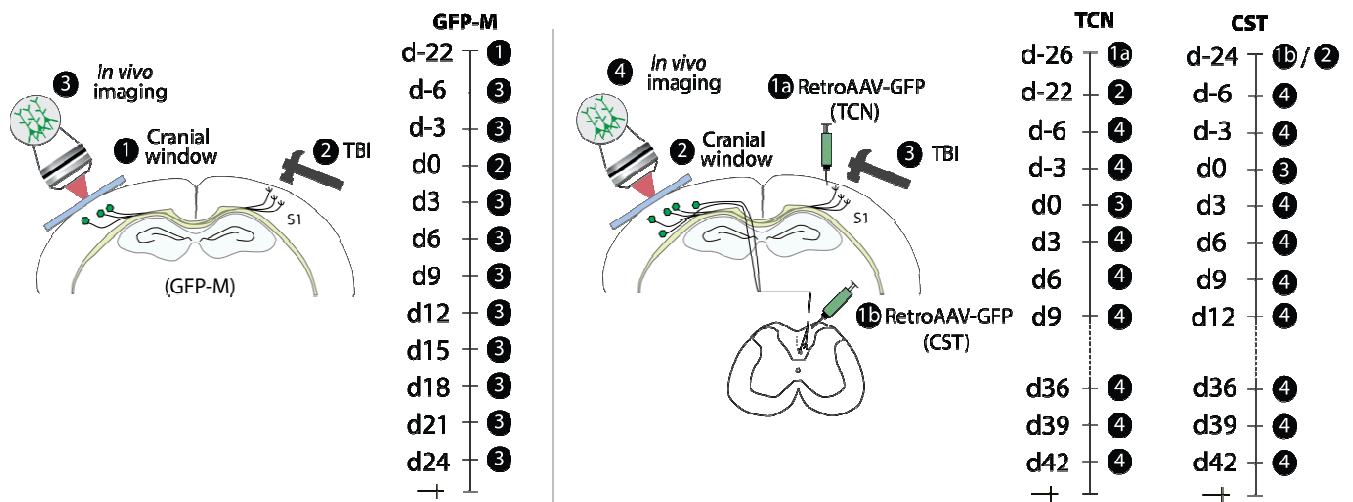


Figure 9. Experimental outline and timeline of in vivo two-photon imaging experiments to investigate spine dynamics after TBI. **Left:** Imaging of a general neuronal population was carried out in GFP-M mice. Here, animals were first implanted with a chronic cranial window. After 2-3 weeks 2 baseline measurements were done, each 3 days apart, before animals were finally injured with our CCI paradigm and imaged every 3 days and up to 24 days after TBI. **Right:** Imaging of the specific cell population of TCN and CST neurons was carried out as follows: For TCN we first injected the somatosensory cortex with a retrograde AAV (RetroAAV-GFP) and then implanted a cranial window about 4 days later. In contrast, to image CST neurons, we injected the spinal cord and implanted the cranial window on the same day. Either way a resting period of 2 to 3 weeks between cranial window implantation and the first imaging session was respected for all imaging groups, thus allowing possible inflammation from the implantation surgery to subside. As with GFP-M animals 2 baseline measurements were done each 3 days apart before injury induction with CCI. Thereafter animals were imaged every 3 days and up to 42 days after TBI. After the last imaging session all animals were sacrificed as illustrated by a cross (left and right panel).

Lastly, on the day of the first imaging session, a custom-made metal head bar was embedded into the pre-existing dental cement (see Figure 10). The metal bar is later used to fix the mouse in an imaging head-fixation device (custom made) and is kept at the same degree as the glass coverslip, in order to make sure that the window lies “horizontally under the microscope and perpendicular to the optical axis of the microscope” (Holtmaat et al., (2009), p. 1137) ²⁴⁹.

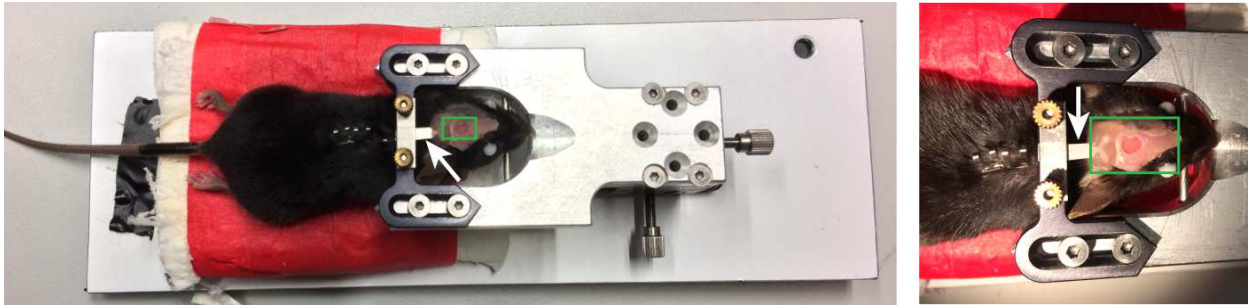


Figure 10. Images of whole head-fixation device prior to being imaged (left) and a closer look at the head-fixation device (right). Note that part of the metal head bar is visible (white arrow), as well as the cranial window surrounded by dental cement (green square).

2.7. Tissue preparation

After completion of experiments all mice were transcardially perfused first with a solution of phosphate buffered saline (PBS), mixed with Heparin (PBS-Heparin; 1:500) and then fixated with 4% paraformaldehyde (PFA). Post-fixation in 4% PFA lasted for 24 hours. Afterwards brains were micro-dissected and kept in 0.1% PBS-azide until further use.

2.7.1. Characterization of transcallosal neurons in the intact mouse brain

For the characterization of TCN across the intact cortex, tissue sections of 100 μ m thickness were cut on a vibratome (Leica) and stained free-floating with NeuroTrace 435 (Invitrogen; 1:500 in 0.1% Triton PBS ¹⁷⁸. Prior to being able to cut the tissue on the vibratome, microdissected brains were embedded in 3% agarose in special tissue moulds (Tissue-Tek® Cryomold® Intermediate, Sakura® Finetek Europe B.V.). The free-floating staining included washing sections 3 times with 1xPBS à 10 minutes, before incubating them in Neurotrace at 4°C overnight. Finally, sections were again washed 3 times with 1xPBS à 10 minutes before being mounted, coverslipped on gelatine subbed slides, embedded in VectaShield (Vector Laboratories) and sealed with transparent nail polish.

2.7.2. Determining comparable lesion outcome and volume after controlled cortical impact

The same staining procedure with NeuroTrace 435 (Invitrogen; 1:500 in 0.1% Triton PBS) as described above in section 2.7.1., was employed to characterize our injury parameters and show a reproducible lesion volume that also fits our experimental aim.

2.7.3. Circuit connectivity of transcallosal neurons after traumatic brain injury

Tissue preparation after experiments related to circuit connectivity went as follows: Mice were transcardially perfused either 7 or 42 days after TBI, as described above. Control mice were sacrificed on the same day as TBI-mice. After the 24-hour period of post-fixation in 4% PFA, brains were microdissected and kept in eppendorf receptacles with 30% sucrose until sinking to the bottom. They were sectioned coronally with a cryostat (Leica CM1850) at a thickness of 60 μm . Next, a GFP-amplification-protocol combined with a NeuroTrace (NT) staining was performed on free-floating sections. To this end, sections were first washed 3 times with 1xPBS à 10 minutes. In the final washing step, 1 x PBS was replaced by blocking buffer (1 x PBS with 0,5% Triton and 10% goat serum) and sections were incubated in it for one hour at room temperature. After removing the blocking buffer, primary antibody solution (1x PBS containing 0.1% Triton, 1% goat serum and 1:500 chicken anti-GFP Ab (Abcam)) was added. Overnight incubation at 4°C ensued. The following day, sections were washed 3 times for 10 minutes with 1x PBS/0.1% Triton and later incubated with the secondary antibody solution (1x PBS -0.1% Triton, 1% goat serum and 1:500, Goat Anti-Chicken Alexa Fluor® 488 Ab (Abcam); 1:500 NT435 (Invitrogen)) overnight at 4°C. After a last washing step, 3 times à 10 minutes with 1xPBS, sections were mounted on gelatine subbed slides with VectaShield (Vector Laboratories) and finally coverslipped as described above.

2.8. Image acquisition and image processing

2.8.1 Distribution of transcallosal neurons throughout the mouse cortex

Images of retrogradely labelled TCN were taken with an Olympus FV1000 confocal microscope equipped with standard filter sets ¹⁷⁸. Images were taken at a 10x magnification, zoom 1 and at a resolution of 1024x1024, using Kalman filtering. Fixed sections of 10 μm thickness were scanned using a z-step size of 1 μm ¹⁷⁸. In contrast, pictures of anterogradely labelled TCN axons were taken with a Leica SP8

confocal microscope and a 20x objective (zoom 1; resolution 1024x1024; step size: 1.04 μ m) ¹⁷⁸. Finally images were processed with Fiji (ImageJ) software to generate maximum intensity projections. Maximum intensity projections were further refined in Adobe Photoshop using gamma adjustments to augment discernability of intermediate gray values and median filtering to subdue noise when necessary ¹⁷⁸.

2.8.2. Characterization of injury outcome after controlled cortical impact

Starting from the first visibly “damaged” section to the last, we imaged 11-17 consecutive sections, always spaced apart at an equal distance, using an Olympus FV1000 confocal microscope (4X objective; resolution 1024 x 1024 pixel; zoom 1). Then the lesion area was manually delineated in each acquired image using the ImageJ (Fiji) measuring tool. Finally the lesion volume was calculated as previously outlined by Yu et al., (2013) ²⁸⁸ (respective formula: Lesion volume= $\{0.5A_1 + 0.5(A_1 + A_2) + \dots + 0.5(A_{n-1} + A_n) + 0.5A_n\} * X$; A= lesion area section n; X= distance between two sequential sections ²⁸⁸).

2.8.3. Investigation of spine dynamics in TCN, CST neurons and a general neuronal population, using in vivo two-photon microscopy

All animals were imaged using a two-photon microscope (Olympus FV1000 MPE), equipped with a Mai Tai DeepSee femto-second pulsed Ti:Sapphire laser (SpectraPhysics). In more detail, the apical dendritic tufts of GFP-labelled neurons of the somatosensory cortex were imaged. Before every imaging session animals were deeply anaesthetized with an i.p. injection of MMF. After ensuring stable anaesthesia mice were fixed by their previously installed head-bar unto a head-fixing device (see section CW implantation, Figure 10) and placed under the two-photon microscope objective (Olympus XLPlan N 25X W MP). To visualize GFP-fluorescence, a green/red Olympus filter cube (FV10-MRVGR/XR; BA595-540, BA575) was used. The mice were typically imaged at a wavelength of 940nm. Usually fluorophores tend to have a broad excitation range and EGFP can for example be imaged with a good efficiency from 830-1020nm ²⁴⁹. During the initial baseline imaging session, possible regions of interests (ROIs) were examined with a low resolution using the Olympus software FluoView FV10-ASW 4.0. A suitable imaging spot constituted an imaging area, in which apical dendrites and spines were clearly and intensely labelled and could be followed up to several 100 micrometers and branching points in depth, ideally even all the way to their cell body. However this was not always possible, especially in animals where TCN and CST neurons were traced via viral injections. Once a good imaging spot was

detected, a low resolution overview stack was taken (resolution: 640 x 640 pixels; Zoom: 1; step 3 or 5 μ m). This overview stack was later used to find back the same ROIs and dendrites each subsequent imaging session. In cases where the dendrites could be followed back to their cell body, layer-origin of the imaged neuron could be verified, by estimating the tissue depth, in which cell bodies were first visible, based on the z-step acquired and the number of sections acquired to “build” the whole stack. In addition, the unique vascular arrangement, visible in superficial layers of the brain through the fluorescence lamp of the microscope, helped locate the same dendrites each following imaging period. For a detailed stack of individual dendrites and their spines, which were later used for spine analysis, a higher resolution image was acquired (resolution: 2048 x 2048 pixels; Zoom: 2; step 1 μ m). In general, at least two detailed images with a varying number of analyzable dendrites (ranging from 3-20) were imaged per animal. Particular care was taken to keep a similar fluorescence intensity and laser power for each ROI, but also in between animals. Image acquisition was performed for baseline measurements and every 3 days after the induction of TBI (see Figure 9). In total 2 baselines were acquired, baseline 1 (B1) and baseline 2 (B2), with 3 days in between each other.

2.8.4. Circuit connectivity of transcallosal neurons after traumatic brain injury - Starter cells

A total of six sections per brain, beginning from slides with the first detectable starter cells to slides with the last detectable starter cells, were scanned using a Leica SP8 confocal microscope. Each section was imaged to an extent of 40 μ m (magnification: 20x; Zoom 1; step; 1 μ m; resolution: 512 x 512 pixels) using a Kalman filter.

2.8.5. Circuit connectivity of neurons after traumatic brain injury - Pre-synaptic cells

To evaluate whether the number or origin of pre-synaptic partners of TCN changes after TBI, m-Cherry positive cells in distinct brain regions were quantified. Here, 20 sections per brain were selected according to the Allen Mouse Brain Atlas (<http://mouse.brain-map.org/>; ²⁸⁹, always corresponding to a rostro-caudal extent from ~1.15 to ~2.85 mm relative to Bregma. Also, each section represented the same level in the Allen Mouse Brain Atlas for each mouse. Hence, the distance between each section was always ~200 μ m for all animals. All sections were imaged consecutively with a Leica DM4 B microscope (Leica Microsystems), using the MBF

Stereo Investigator software and a 2.5X objective. In cases where cell labelling was too dense we opted for a higher 10X objective, to be able to discern cell bodies from each other better. All image stacks were further processed and stitched with the Fiji Pairwise Stitching Plugin.

2.9. Data analysis

2.9.1. Distribution of transcallosal neurons throughout the mouse cortex

TCN axons were anterogradely traced with BDA 10,000 MW in order to visualize in which layers of the contralateral homotopic cortical column they project to. For this purpose we quantified their distribution in 3-5 sections per animal using Fiji (ImageJ)²⁹⁰ and defined cortical layers based on the NeuroTrace staining. The sections spanned from the centre of injection (-1.5 mm from Bregma) to the 2 immediate sections rostrally and caudally of the injection site¹⁷⁸. Further, the area in which terminal fields were detected was delineated per layer and throughout the entire depth of the cortical column. Based on this, the integrated density for each layer and the whole cortical column (“total integrated density”) was calculated using the “Measure tool” in Fiji (ImageJ)¹⁷⁸. Integrated density was “defined as the product of the area analyzed by the mean intensity in this area (the sum of the intensity values of all the pixels in the selection divided by the number of pixels” (Chovsepian*, Empl* et al., (2017), p.3)¹⁷⁸. Proportion of terminal fields in specific layers were calculated by dividing the integrated fluorescence intensities of this layer by the total integrated fluorescence intensity measured within the cortical column¹⁷⁸.

In addition we also quantified the number of TCN retrogradely traced with FG. To this end we analyzed 5 sections per animal. Here we defined the centre of injection as the section (section 0) which had the most intense labelling for each rostro-caudal injection coordinate (corresponding to -1.5 mm from Bregma the group injected caudal Bregma +0.3 mm for the group injected rostral to Bregma)¹⁷⁸. From this reference point onwards we imaged the following coordinates: -2.1 mm, -1.8 mm, -1.5 mm, -1.2 mm, -0.9 mm from Bregma (for the injections caudal to Bregma) and -0.7 mm, 0 mm, +0.3 mm, +0.6 mm, +0.9 mm from Bregma (for the injections rostral to Bregma), respectively¹⁷⁸.

After image acquisition, FG-positive cells were counted manually on maximum intensity projections (z-stacks) using the Fiji Cell Counter Plugin. In more detail, FG-positive cell bodies were counted in 3 specific areas: the homotopic area (HA),

the middle of which was situated at the same distance from the midline as the centre of the injection site, the lateral adjacent area (LAA) and medial adjacent area (MAA) ¹⁷⁸, which lied directly next to HA but on opposite sides. Each area had the same size of 1226mm². Transcallosal projection neurons were counted separately for each area and layer within that area. The layers were again defined with the help of the existing NeuroTrace staining. Finally, a ratio between the cells in a given cortical layer of a given area (HA, MAA or LAA) and the total number of FG positive cells present in the entire area (HA, MAA or LAA) was calculated ¹⁷⁸. Further, an overview of the general distribution of TCN throughout the entire cortex was acquired, by pooling the quantification of TCN for all the injection coordinates present ¹⁷⁸. As a second point, we set out to investigate the distribution of TCN in more detail, and as such analyzed their distribution for all injection coordinates separately ¹⁷⁸. These corresponded to the primary motor cortex and primary, the somatosensory cortex (outside and within the barrel cortex) ¹⁷⁸.

2.9.2. Analysis of in vivo spine dynamics and counting criteria

Image analysis was performed only in the high resolution stacks with Fiji (ImageJ) software. Once salt and pepper noise was reduced by image processing (“Despeckle”), suitable dendrites for counting were determined. Generally spines were preferably counted on brightly labelled dendrites that could also be followed over the entire imaging period. The length of each dendrite was traced and measured with Fiji at baseline. Dendritic spines were counted using the Fiji Cell Counter Plugin at each time-point, by going through stacks manually and looking at each plane individually. Here, we mainly adhered to previously described counting criteria for dendritic spines ^{117,248,249}. In short, only structures clearly protruding laterally from the dendritic shaft, with a minimum protrusion length of 0.4 μm , were defined and counted as spines. Structures, however, that fulfilled these criteria but coincided with another crossing dendrite and could not be distinctly attributed to the chosen dendrite were not included in the analysis. For each imaging time-point the total spine number, number of eliminated and formed spines, as well as the stable number of spines from one time-point to the next were determined. Elimination, formation and number of stable spines were concluded by comparing dendrites and their spines from one time-point to the next. A spine was defined as eliminated, if it was not visible anymore in the next time-point or as formed, if a new structure appeared, at the same location or where no spine had been counted before. Spines that were visible in both time-points at the same

location were considered as stable. In addition, an elimination and formation rate was calculated by dividing the number of eliminated or formed spines at one time-point by the number of total spines in the previous time-point and multiplied by 100 (thus, rates were expressed as percentages). Spine density in turn was calculated relative to the length of the dendrite (number of spines/ μm). Finally, the spine turnover rate (TOR) was determined according to previous publications²⁴⁹ ($\text{TOR}(t_1, t_2) = (N_{\text{formed}} + N_{\text{eliminated}}) / (N(t_1) + N(t_2))$), “where $N(t_1)$ and $N(t_2)$ are the total number of structures at the first and second time point, respectively” (Holtmaat et al., 2009, p.1132²⁴⁹). The spine TOR is an indication as to how dynamic a system can be and characterizes the rate at which spines come and go from one time-point to the next²⁴⁹.

Finally, the survival and persistence/life-time of spines was evaluated. For this purpose, a distinction between a spine that was present at both baseline measurements (i.e. “initial spines”) and a spine that was newly formed after injury was made on a primary level. In addition, as has been described by Holtmaat et al., (2009)²⁴⁹, the survival fraction (SF) of spines was calculated. The SF describes the survival of spines present at baseline (i.e. initial spines) over the course of the whole experiment. It is calculated by dividing the number of spines that are still present at time-point t (i.e. $N(t)$), by the number of spines present at baseline (N_0), i.e. $\text{SF} = N(t) / N_0$.

Moreover spine persistence, or lack thereof, after injury was assessed and the so called “persistence index” (PI), of both initial spines and those that were newly formed after injury, was calculated. The PI was chosen as a measure of longevity/stability of a spine, giving an indication on how long a spine was present throughout all imaging sessions after injury. Thus for initial spines, single spines on dendrite stretches were followed at each imaging time-point and attributed to a binary code of either “1” for being present or “0” for having been eliminated at every time-point individually. Then, the number of days they were present was divided by the number of all subsequent imaging time-points, which also corresponds to the mean of binary numbers at each time-point after injury. As a result, a spine that, for example, was present throughout the whole experiment, from baseline to 42dpi, would thus have a PI of 1. A spine that was only of a transient nature, for example only present at one single imaging time-point and then was permanently eliminated for the all other imaging sessions, would have a PI close to zero. For spines that were not present at baseline, but were formed after injury (i.e. from 3dpi onwards), the same PI was calculated, from the time-point they were formed onwards.

Furthermore we classified spines into two categories, following a categorization previously established by Liebscher et al., (2014)¹³⁷, but with slight modifications: Those that were present at baseline, and persisted throughout the whole imaging sessions were classified into the category ‘persistent initial spines’. Spines that appeared after injury and survived for at least 3 imaging sessions and up until the very last imaging time-point were considered to be “persistently gained” or ‘PGI’. From these categories a percentage of how many spines correspond to each category, in relation to the total number of either initial or newly formed spines on each dendrite, was calculated.

2.9.3. Circuit connectivity of transcallosal neurons after traumatic brain injury - Starter cell quantification

Using the ImageJ (Fiji) Cell Counter Plugin, starter cells were counted in 4 individual levels of the acquired image stacks, each level 13 μm apart. Cells were identified and counted as starter cells, if they were found to be double-positive for m-Cherry and GFP. It should also be noted, that viral injections yielded a certain range of variability in the starter cell labelling across the brain. Thus, although the expression pattern usually roughly followed a bell curve, the centre of injection could vary in its location from mouse to mouse. In addition, the 6 sections did not always correspond to the same distance from Bregma for each animal and thus represented different rostro-caudal coordinates relative to Bregma depending on the mouse. As a consequence we could not infer that the number of cells in between the 6 sections was comparable in between animals. Therefore we chose to estimate the cell number in sections that were not counted, through interpolation of cell numbers in between the 6 sections that were in fact quantified. Interpolation constitutes a mathematical method by which one can compute reasonable estimates of data points between actually measured data points²⁹¹. The interpolation curve goes through all the data points²⁹¹. In our case, we had starter cell counts for 6 distinct, but variable in between animals, rostro-caudal levels relative to Bregma. We therefore interpolated starter cell number counts for each missing coordinate in each animal and essentially created a full data set for each coordinate recognized in the Paxinos Mouse Atlas²⁹², comprising estimated and quantified values. Due to the fact that originally counted sections were unevenly spaced, and the original data did not follow a linear function, we applied cubic spline interpolation in Python (Cubic spline function: $S_i(x) = a_i(x-x_i)^3 + b_i(x-x_i)^2 + c_i(x-x_i) + d_i$, where x ranges from x_i to x_{i+1}). Furthermore, interpolation was done

under the general assumption that the number of starter cells, beyond the first and last section counted, was zero. Finally, the total number of starter cells in each mouse brain was calculated by summing up all individual cell counts at each coordinate.

2.9.4. Circuit connectivity of transcallosal neurons after traumatic brain injury - Pre-synaptic cell quantification

For quantification, each imaged section was subdivided into different brain areas, as defined by the Allen Mouse Brain Atlas (see Figure 11) how regions were matched). In total we chose 20 different brain regions, ranging from cortical to subcortical regions as well as white matter tract structures. Within those, pre-synaptic cells (m-Cherry positive) were manually counted with the Fiji Cell Counter Plugin. For areas in which cell aggregation was too dense and manual counting was not accurate enough we employed Fiji's Particle Analyzer Plugin for automatic quantification. Our final measure to quantify how "well" TCN are connected to their pre-synaptic partners in specific brain regions after injury was the ratio between the total number of pre-synaptic neurons in that specific area to the total number of starter cells in the whole brain. This ratio was termed connectivity ratio, as previously described by Falkner et al., (2016)²⁹³.

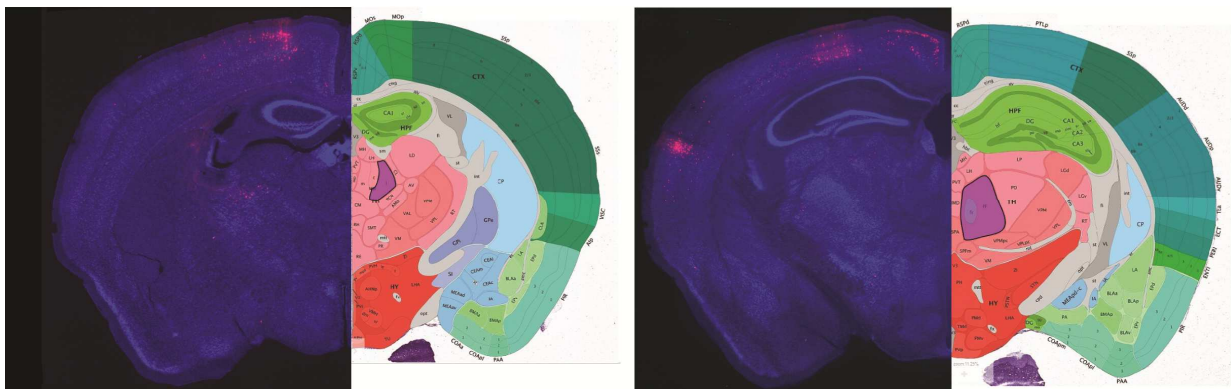


Figure 11. Representative images of how areas of quantification for pre-synaptic cells in specific brain regions were matched to the Allen Brain Atlas. Every chosen brain section was matched to the individual coordinate/level it was assigned to in the Allen Brain Atlas. Based on this alignment, sections were compartmentalized in their individual brain regions, as illustrated in the Allen Brain Atlas, and the pre-synaptic cells were counted within these defined areas. Red dots in the fixed tissue section represent pre-synaptic cells. In the left panel, for instance, pre-synaptic partners were, amongst other areas, found in the cortex close to the midline. Hence these cells would be characterized as pre-synaptic cells in the motor cortex as observed in the Allen Brain Atlas (see the bright green compartment close to the midline, representing areas of the motor cortex). Image source for Allen Brain Atlas: <http://atlas.brain-map.org/>, from the adult mouse 3D coronal reference atlas.

2.10. Statistical Evaluation

All results are given as mean +/- standard error of the mean (SEM), unless otherwise stated. Statistical analysis, as well as graphs illustrating data, was carried out with GraphPad Prism 7.01 for Windows (GraphPad Software). For the majority of experiments involving in vivo two-photon imaging one-way repeated measures (RM) analysis of variance (ANOVA) followed by a Bonferroni's post hoc test was performed. In case data were not normally distributed, we performed a non-parametric test (Friedman test). In experiments without data of a "repeated-measures-type" an ordinary one or two-way ANOVA, followed by a Bonferroni post hoc test, was carried out. Assessment of data and if they follow a normal distribution was achieved through a Shapiro-Wilk Normality test. In-vivo imaging data were tested for statistical outliers using the ROUT-method (Q=1) (see ²⁹⁴ for more details). In addition, paired two-tailed t-tests were carried out for in vivo imaging experiments (unless otherwise stated), while an unpaired two-tailed t-test was performed for mono-synaptic rabies tracing of circuit connectivity after injury. In cases where data were not normally distributed non-parametric t-tests were performed (Mann-Whitney test). In addition statistical significance levels are indicated as follows: $p < 0.05$; $**p < 0.01$; $***p < 0.001$; $****p < 0.0001$. Illustrations and schemes were created in Illustrator (Adobe Creative Suite CS6).

- RESULTS -

3.1. Descriptive study of transcallosal neurons in the mouse cortex

In order to broaden the knowledge on the organisation and distribution of TCN in different anatomically and functionally distinct regions of the mouse cortex, we used anterograde and retrograde tracing techniques to visualize the projection pattern of TCN and the location of their cell bodies throughout the mouse cortex.

3.1.1 Anterograde labelling reveals homotopic and layer-specific organisation of axonal projections of TCN in the contralateral cortex

Anterograde tracing with BDA revealed that terminal fields of TCN in either layer II/III or V project to a homotopic cortical column (i.e. mirrored location) in the cortical hemisphere contralateral to the injection site (see Figure 12). We verified that injections with BDA were indeed layer-specific, by quantifying the percentage of BDA-positive neurons in animals injected in either layer II/III or V. Indeed, our quantification showed that animals injected in the upper layers of the cortex predominantly showed BDA-positive cells in layer II/III. More precisely over 40% of all TCN resided in layer II/III (see Figure 12, A; $p < 0.001$). Similarly, injections exclusively in layer V resulted in labelling of about half of TCN in the corresponding layer V (see Figure 12, A; $p < 0.001$). Further, as Figure 12 B and C reveal, projections of TCN in layer II/III and V were visible in the entire homotopic cortical column, for both injection conditions. Interestingly, we also observed terminal fields outside of the usual and predominantly labelled homotopic area of the cortical column (see white arrows in Figure 12, B). These ectopic projections were more frequent in animals initially injected with BDA in layer V. In addition, both TCN in layer II/III and V seem to project to their corresponding layer and contralateral column in a similar way (see Figure 12, D). Hence, both upper and deeper layers equally have around 40-50% of their projections in layers II-IV and around 35% in layer V (as revealed by determining the integrated fluorescence intensities of terminal fields in the homotopic cortical columns, see Figure 12, D). That said, it should be noted that a smaller percentage of projections were also found in layer VI. This indicates that TCN projections are not entirely restricted to the origin of their cell bodies, but in fact span all the layers in the contralateral side. Between both injection depths no statistical difference was found. As such, both cell bodies of TCN layer II/III and V have a comparable projection pattern to the contralateral hemisphere: Mostly homotopic and throughout all the layers of the respective cortical column.

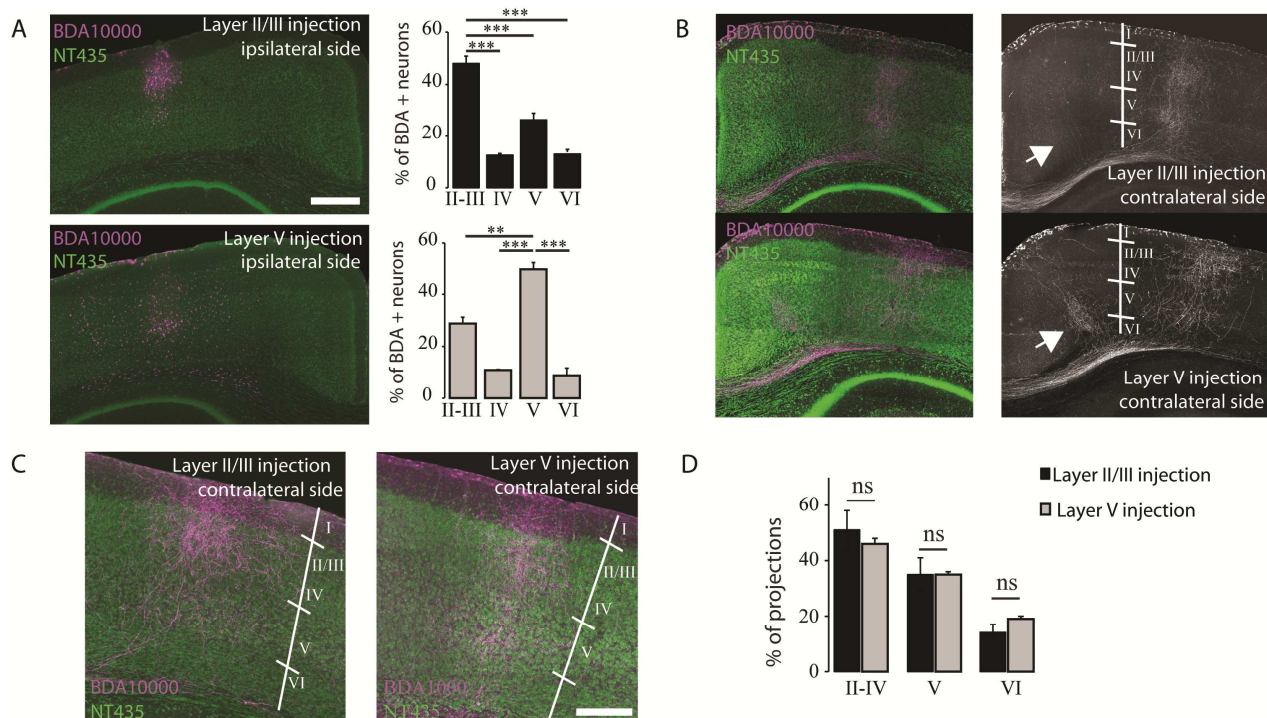


Figure 12. Transcallosal projections reside in homotopic cortical columns and specific layers.

A. Left: Confocal images of TCN on the ipsilateral side of injection with biotinylated dextran amine (BDA) 10.000 MW in either layer II/III or V (Neurotrace: green; BDA: magenta). **Right:** Quantification of BDA-positive TCN in different cortical layers, for either injections in layer II/III (black) or V (grey). **B.** Confocal images of transcallosal projections in the hemisphere contralateral to the injection site in either layer II/III or V. White arrows indicate terminal fields projecting outside of the regular homotopic cortical column. **C.** Higher magnification of projections to the contralateral cortex. **D.** Quantification of integrated fluorescence intensities of terminal fields in the homotopic and contralateral cortical columns, separated by layers. Scale bars: 500 μ m in **(A,B)** and 200 μ m in **(C)**; Neurotrace: green, BDA: magenta. One-way analysis of Variance (ANOVA) with Tukey post-hoc testing: *** $p < 0.001$; ** $p < 0.01$. Figure adapted from Chovespian*, Empl* et al., 2017¹⁷⁸.

3.1.2 Retrograde labelling of TCN uncovers a comparable homotopic and layer-specific organisation in different cortical areas

A retrograde tracing technique was used to investigate how TCN are organised and distributed throughout the entire mouse cortex. To this end, we injected three different cortical areas (motor, somatosensory and barrel cortex respectively) at three different medio-lateral coordinates with the retrograde tracer FG. Firstly, we determined a so-called homotopic area (HA) representing the mirrored location of the tracer injection site in the contralateral hemisphere (i.e. both areas have same distance from the midline). Further, we designated two adjacent areas, that represent regions of the same size right next to the HA. The area more lateral to the midline was titled lateral adjacent area (LAA), while the area more medial to HA and the midline medial adjacent area (MAA). As seen in Figure 13 most retrogradely labelled TCN fall within HA. In more detail, over 60% of cells lie within HA (see

Figure 13, C). A smaller amount of cells were found in the LAA (around 20%) and MAA (around 15%). Strikingly, we also observed TCN much further away from the designated areas (see white arrows in Figure 13, A and B)

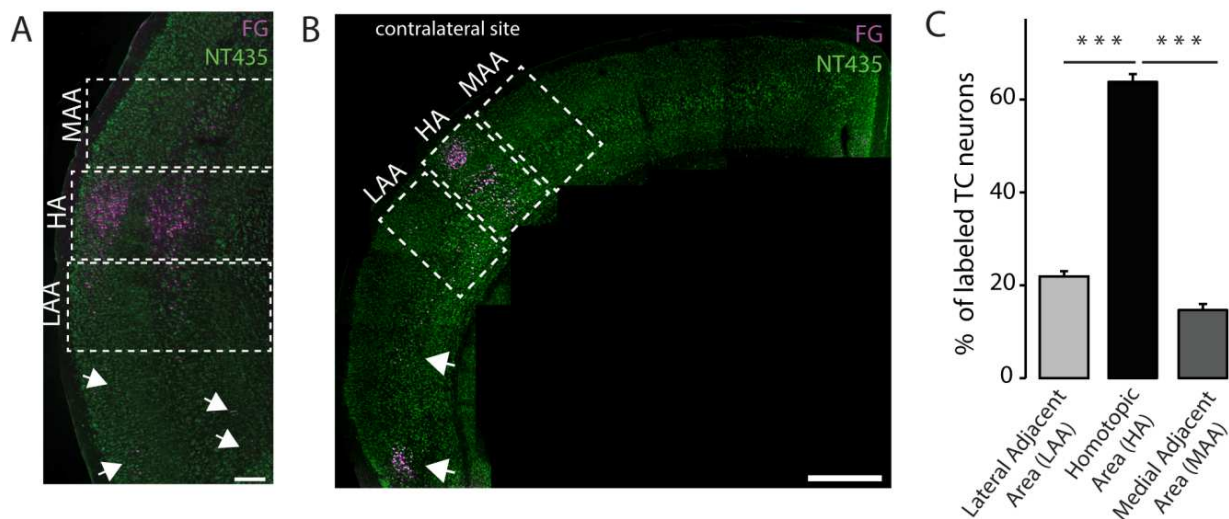


Figure 13. Retrogradely labelled transcallosal projection neurons are homotopically organized
A,B. Confocal example images of TCN on the contralateral side of the injection site with Fluorogold (Neurotrace: green; Fluorogold: magenta). White arrows indicate ectopic location of projection neurons. Scale bar 200 μ m in **(A)** and 500 μ m in **(B)**; HA= homotopic area, LAA= lateral adjacent area, MAA= medial adjacent area. **C.** Quantification of the percentage of Fluorogold-positive cells within the designated areas. One-way ANOVA with Tukey post-hoc testing: *** $p < 0.001$. Figure adapted from Chovespian*, Empl* et al., 2017¹⁷⁸

This mostly homotopic organisation remained comparable in all other cortical areas and medio-lateral injection coordinates (see Figure 14). Regardless of location, be it in a more rostral (with regards to Bregma) part of the motor, somatosensory or barrel cortex the majority of TCN still resided predominantly and to a similar proportion in the HA (see Figure 14, full bars). Similar results apply to injection sites in all three anatomically distinct regions of the cortex that are more caudal with respect to Bregma (see Figure 14, striped bars).

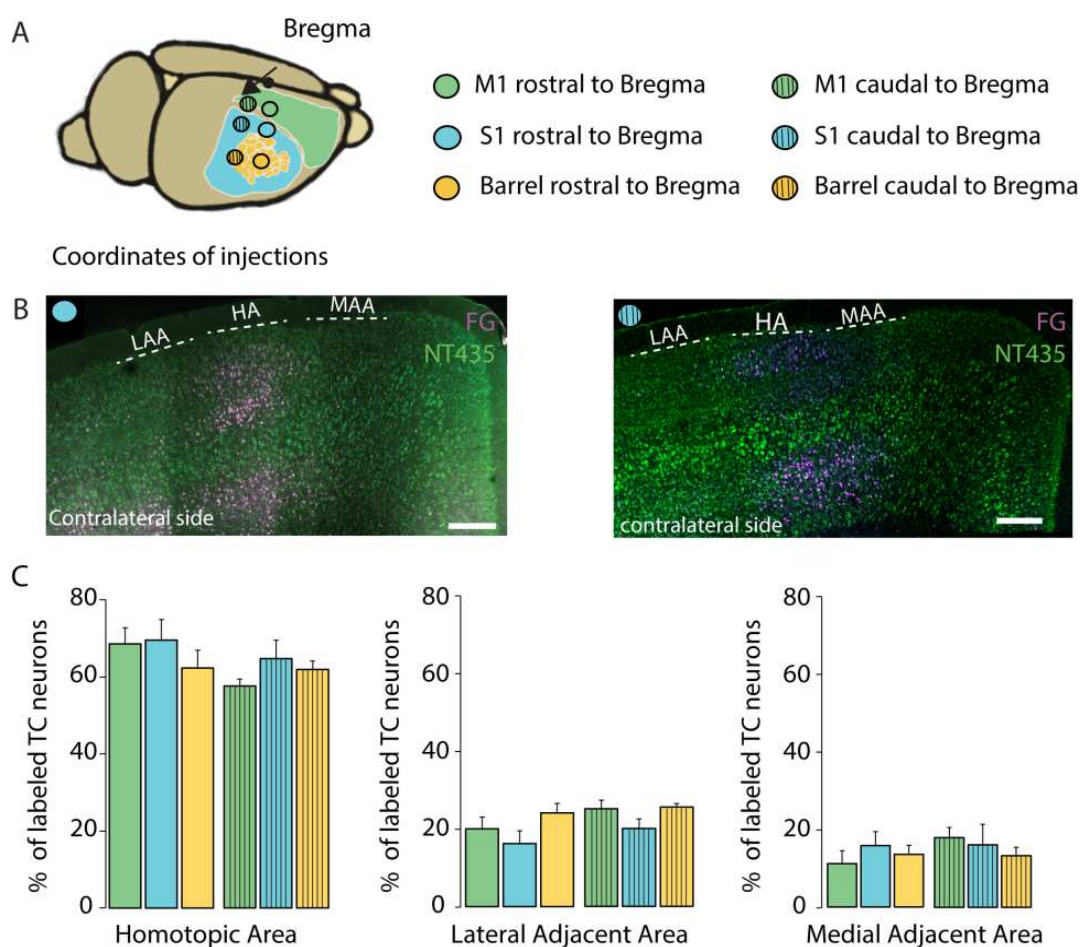


Figure 14. Transcallosal projection neurons remain homotopically organized in different cortical areas. **A.** Schematic depiction of injection coordinates for retrograde labelling of TCN. **B.** Representative confocal example images of retrograde labelling. The particular image depicts injection in a rostral (full circle) and caudal (striped circle) part of the barrel cortex. Neurotrace: green; Fluorogold: magenta; HA= homotopic area, LAA= lateral adjacent area, MAA= medial adjacent area. Scale bars 250 μ m. **C.** Quantification of the percentage of Fluorogold-positive cells within the designated areas for all the different cortical regions and areas HA, LAA and MAA. Full bars: labelling rostral to Bregma; Striped bars: Caudal labelling. Green: Motor cortex, blue: Somatosensory cortex, yellow: barrel cortex. One-way ANOVA with Tukey post-hoc testing for each area. Figure adapted from Chovespian*, Empl* et al., 2017¹⁷⁸.

We further analyzed whether TCN are organized in a layer-specific manner. For this purpose we quantified the percentage of labelled TCN in each layer of the cortex and found that TCN are primarily located in layer II/III and V (see Figure 15). As such, a simple Neurotrace staining again served as an orientation to distinguish layers. For the HA the majority of cells (close to 45%) were located in layer II/III, while a little over 30% were found in layer V. This layer-specific organization was seen in all areas, i.e. HA, LAA and MAA respectively. Furthermore, we found that TCN were not solely distributed in layer II/III and V. Interestingly they were also, albeit to a lesser extent, seen in layer IV (a little over 10%) and VI (a little over 14%) of the cortex.

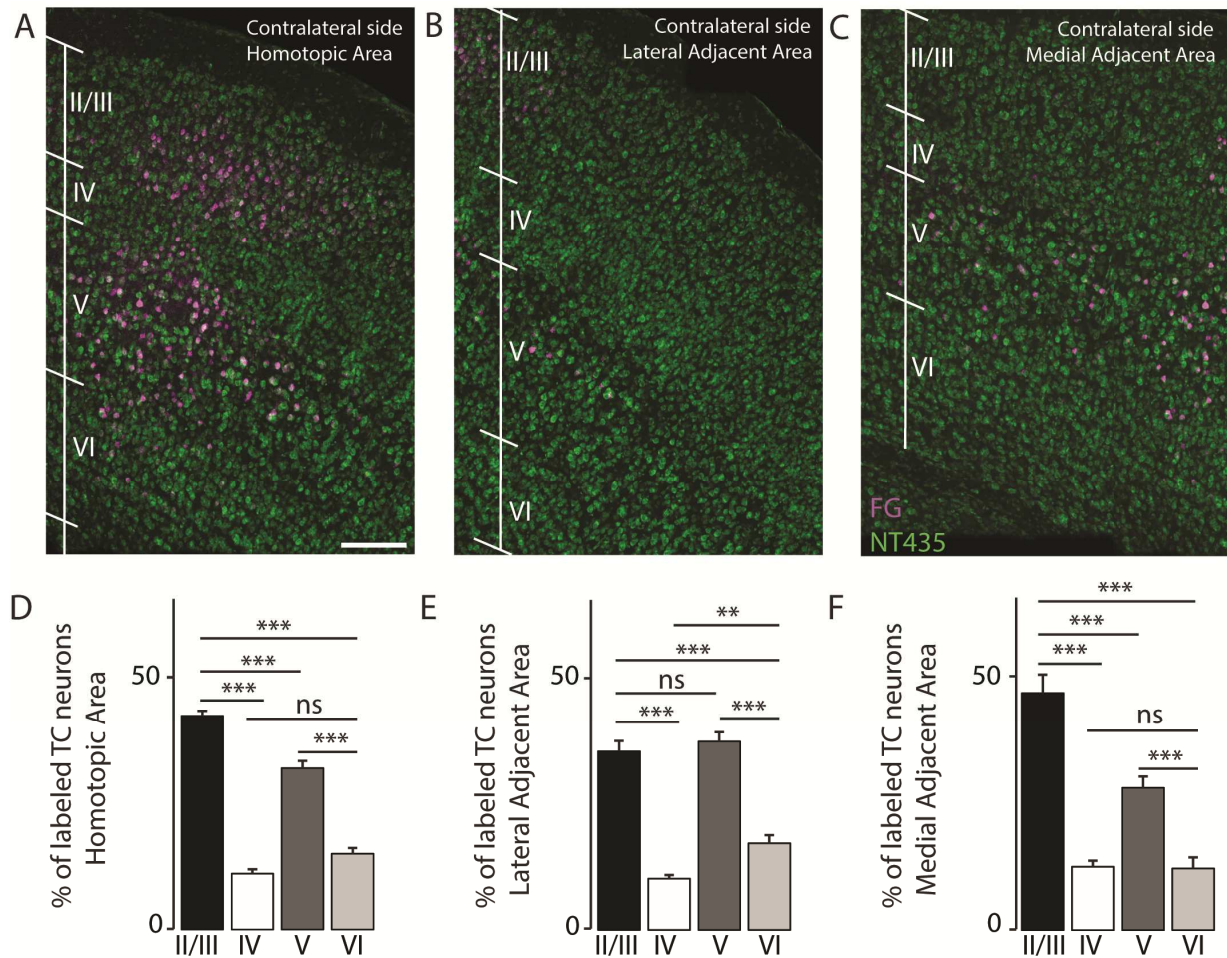


Figure 15. Transcallosal neurons are organized in a layer-specific way throughout cortical columns. (A,B,C) Representative confocal example image of retrograde labelling in different cortical layers (from left to right: HA, LAA, MAA). Scale bar: 200 μ m. **(D,E,F)** Quantification of the percentage of Fluorogold-positive cells within the designated areas for different cortical layers (from left to right: HA, LAA, MAA). One-way ANOVA with Tukey post-hoc testing for each area: *** $p < 0.001$; ** $p < 0.01$. Figure as published in Chovespian*, Empl* et al., 2017¹⁷⁸.

Finally, we also analyzed whether the layer-specificity of TCN could be seen in and/or is dependent on the particular cortical area they originate from (see Figure 16). Here we observed that, when looking at the HA, in principle the majority of cells resided in layer II/III and V irrespective of the cortical regions. This observation was a little less well-defined for the adjacent areas. In this respect, the LAA displayed a higher number of cells in layer V than in layer II/III when looking at the barrel cortex specifically (see Figure 16, C), while in the MAA cells were found more abundantly in layer VI, compared to LAA and HA, in the injection coordinate of the barrel cortex located more caudal to Bregma (see Figure 16, D).

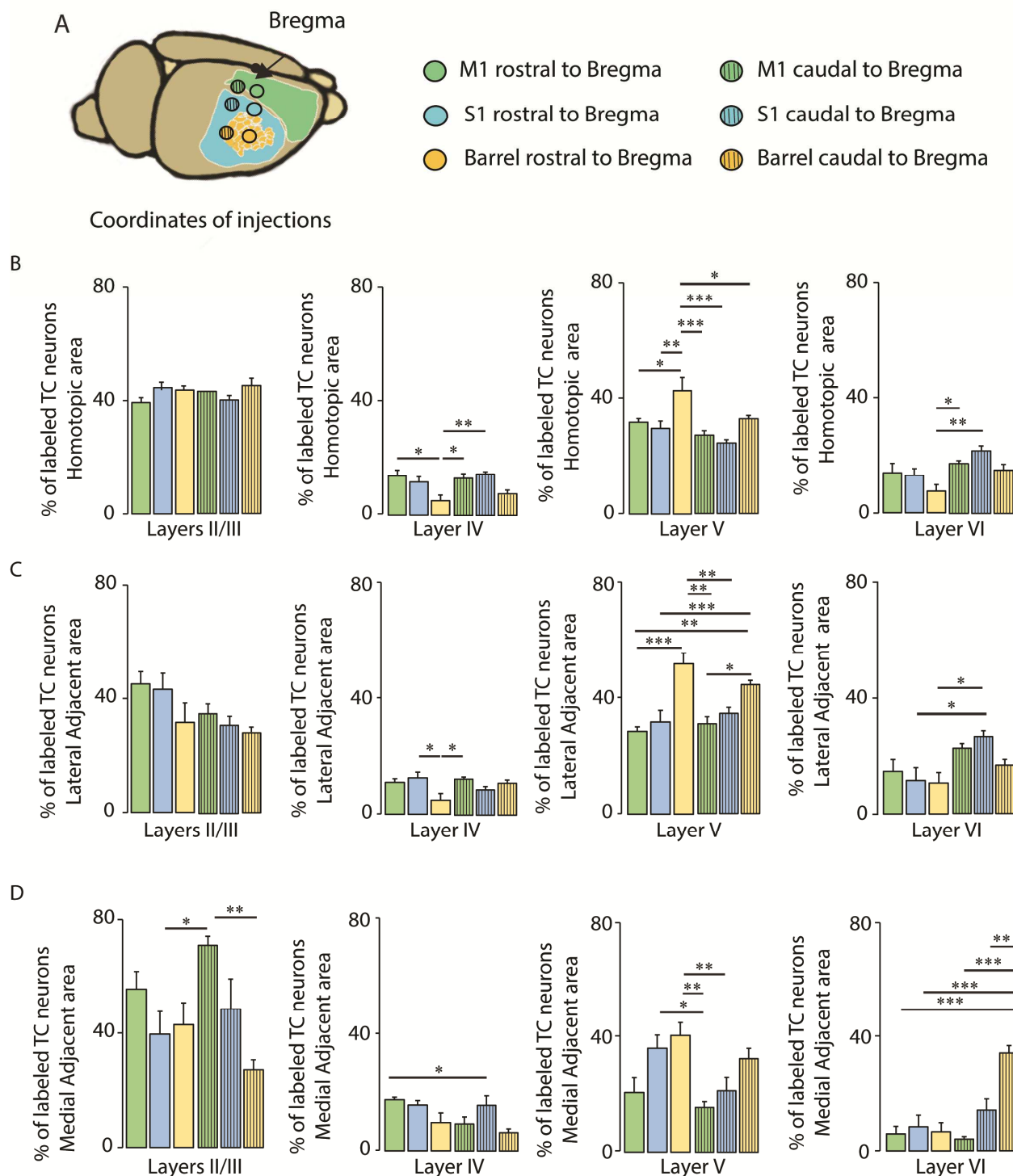


Figure 16. Transcallosal projection neurons are organized in a layer-specific way with slight differences in different cortical regions. **A.** Schematic depiction of injection coordinates for retrograde labelling of TCN. **B.** Quantification of percentage of Fluorogold-positive cells found in different layers and cortical regions in HA. Full bars: labelling rostral to Bregma; Striped bars: Caudal labelling. **C.** Quantification of the percentage of Fluorogold-positive cells within different cortical layers in LAA. Full bars: labelling rostral to Bregma; Striped bars: Caudal labelling. **D.** Quantification of the percentage of Fluorogold-positive cells within different cortical layers in MAA. Full bars: labelling rostral to Bregma; Striped bars: Caudal labelling. Green: Motor cortex, blue: Somatosensory cortex, yellow: barrel cortex. Two-way ANOVA (variable one: areas of labelling; variable two: injection sites, with Bonferroni post-hoc testing for each independent data set: *** $p < 0.001$; ** $p < 0.01$; * $p < 0.05$. Figure taken from Chovespian*, Empl* et al., 2017¹⁷⁸.

3.2. Determination of lesion volume of our injury parameters by CCI

To characterize the injury outcome of our TBI paradigm, we calculated the lesion volume of 5 individual mouse brains. To this end, we manually delineated the lesion area of 10-17 sequential sections, beginning from the first visibly “damaged” section to the last (see Figure 17). Finally the lesion volume was calculated as previously outlined by Yu et al., (2013) ²⁸⁸. As seen in Figure 17 all 5 animals show a comparable lesion volume, solidifying a reliable reproduction of lesion outcome for our subsequent experiments. The mean lesion volume of all animals was $12.5\text{mm}^3 \pm 0.58 \text{mm}^3$. In addition, we observed that the lesion extent did indeed affect the corpus callosum, representing the main building block of TCN, but did not go deeper than any subcortical areas such as the hippocampus, considerably.

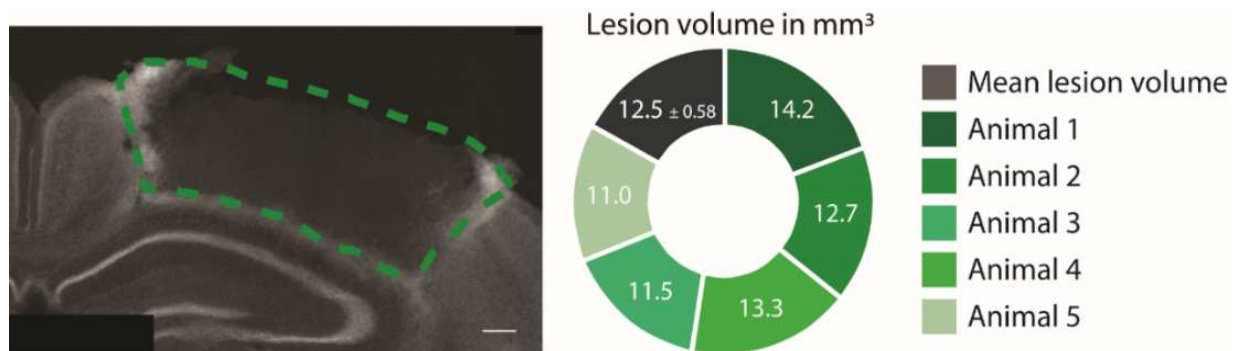


Figure 17. CCI injury paradigm creates reproducible lesion outcome. Left: Schematic depiction of manual lesion outline procedure; Green line depicts outlined lesion area for an example section. **Right:** Quantification of lesion volume as previously described by Yu et al., 2013 ²⁸⁸; n= 5. Scale bar: 100µm

3.3. In-vivo imaging and analysis of spine dynamics after TBI in the non-injured contralateral somatosensory cortex

To investigate the effect of TBI on the spine dynamics of neurons in the non-injured hemisphere, we imaged the apical dendrites of neurons, either on a general population level or specifically in TCN and CST neurons respectively, with in vivo two-photon microscopy. Pre-injury levels of spine dynamics were acquired by imaging animals two times within the same interval before injury, thus generating two baselines, B1 and B2.

3.3.1. Observations based on a population level using GFP-M mice

In order to get a general idea on the effect of TBI on the spine dynamics of a broader neuronal population, the apical dendrites of layer V neurons in GFP-M mice of the intact contralesional hemisphere were imaged *in vivo* over a span of 24 days after injury. As previously reported in GFP-M mice^{238,295}, the complete neuron was fully labelled, from cell body to axon onto the dendritic arbours and their spines, in this study as well. Thus GFP-M mice proved suitable for *in vivo* two-photon microscopy (see Figure 18). The layer specificity of the imaged neurons was determined by following the dendrite to its cell body and estimating the tissue depth based on the thickness of the z-stack acquired and the number of sections acquired to build the whole stack, using the low resolution overview image collected beforehand (see also Materials & Methods, section 2.8.3.). As a whole, 81 dendrite stretches (sum of the number of all spines counted throughout the whole imaging experiment: $n=10191$) of *only* layer V neurons in 4 GFP-M mice were analyzed. The average length of the dendrite stretches counted was $63.31\mu\text{m} \pm 1.54\mu\text{m}$.

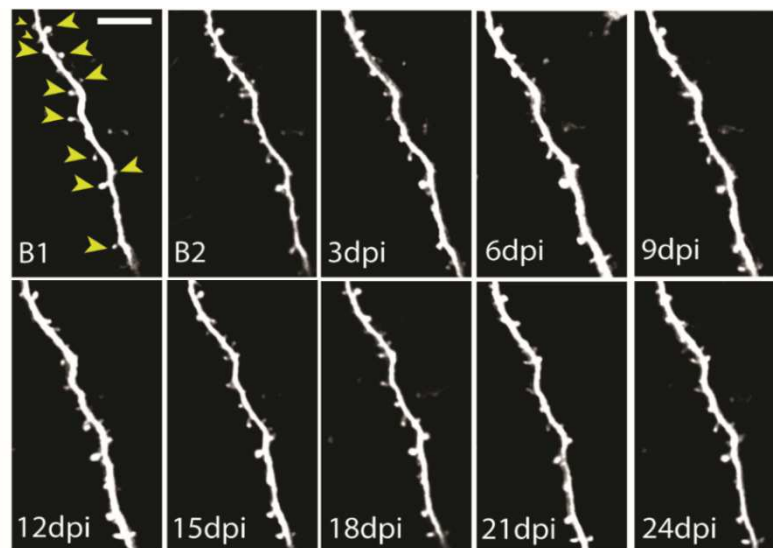


Figure 18. Two-photon microscopy images showing a representative time lapse series of an apical dendrite from a layer V neuron in a GFP-M mouse. Each square represents a snapshot of the same dendrite stretch of a layer V neuron imaged at a specific experimental time-point, and followed up to 24 days post TBI. Arrowheads illustrate examples of spines on dendrite stretch. B1: Baseline 1, B2: Baseline 2; Scale bar: $10\mu\text{m}$.

As mentioned before, spine density (as a ratio of the total spine number to the length of the dendrite stretch counted), turnover and elimination/formation/stable rate of spines represented the measures of spine dynamics that were analyzed within this thesis. The turnover indicates how dynamic (“flexible”) a system is, by

representing the sum of eliminated and formed spines at time-point X divided by the sum of total spines at time-point X and its respective previous time-point. Finally, the rates of elimination, formation and stability of spines are represented by a percentage, as calculated by the number of eliminated, formed and stable spines divided by the number of total spines in the previous time-point. Figure 19 shows what represented a stable, eliminated and newly formed spine in GFP-M mice.

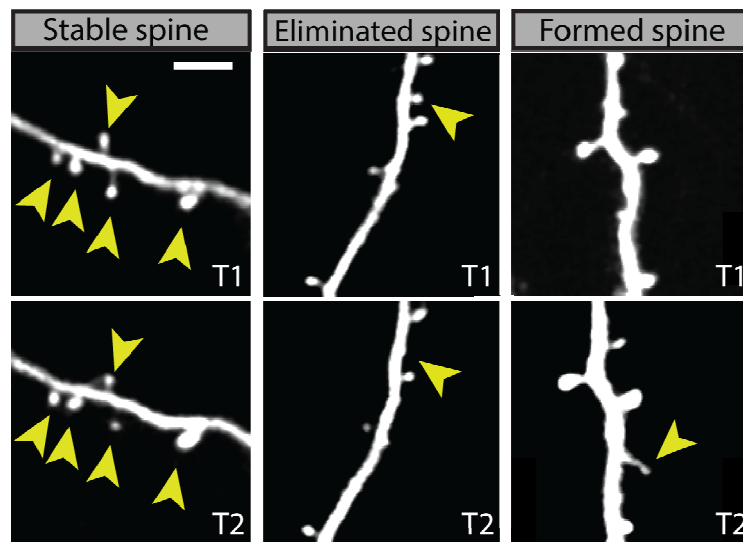


Figure 19. Representative two-photon microscopy pictures of stable, eliminated and formed spines in GFP-M mice. Only structures clearly protruding from the dendrite shaft were counted as spines (see yellow arrowheads). A spine was considered stable when it was identified at the same location from one time-point (T1) to the next (T2; left panel). Further a spine was considered as eliminated, when the clear protrusion in one time-point could not be found back in the next time-point, having completely disappeared into the dendritic shaft (middle). Finally a spine was considered to be newly formed, if it was only visible as a novel protrusion from the dendritic shaft at a specific time-point (T2), at a location that previously (T1) did not show any signs of a spine before. Scale bar: 5 μ m.

As a result this thesis shows that, in an unspecific neuronal population of layer V pyramidal neurons in the contralesional somatosensory cortex of GFP-M mice, spine density significantly decreased after 3 and 6 days post injury (dpi), when compared to spine densities before injury (baseline measurements B1 and B2; see Figure 20). This decrease did not significantly recover even after 24dpi.

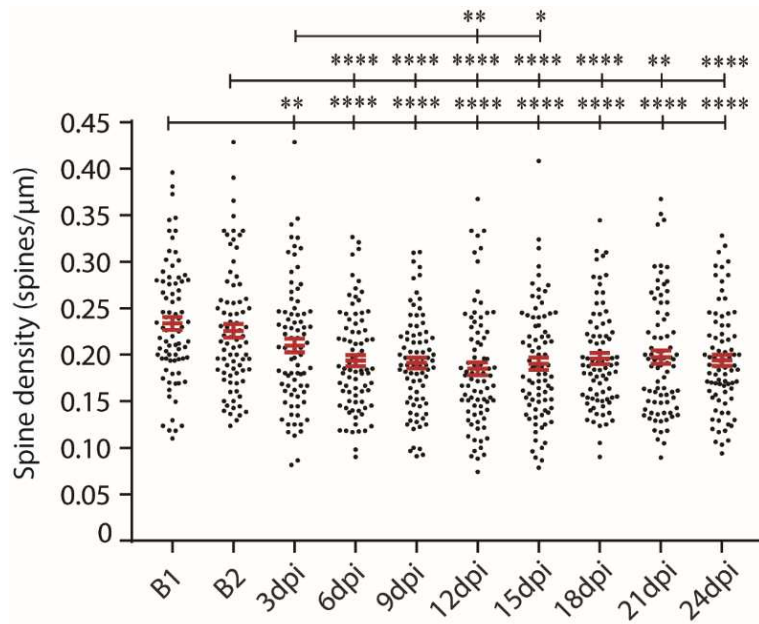


Figure 20. Spine density of layer V pyramidal neurons in GFP-M mice. Each dot represents one dendrite. Spine density significantly decreases after 6dpi when compared to baselines and does not recover to pre-injury levels. One-way repeated measure (RM) ANOVA with Bonferroni post hoc testing for each timepoint. **** $p < 0.0001$, ** $p < 0.01$; * $p < 0.05$; $n(\text{animals}) = 4$, $n(\text{dendrites}) = 81$, $n(\text{spines}) = 10.191$.

Further, there is an additional statistically significant decrease in spine density at 12 and 15dpi, when compared to spine densities at 3dpi. This decrease recovers to a similar density level as in 3dpi again, after 18dpi (see Figure 20 and Table 2). In contrast to spine density, turnover of spines within our imaging period did not significantly change over time (see Figure 21 and Table 2).

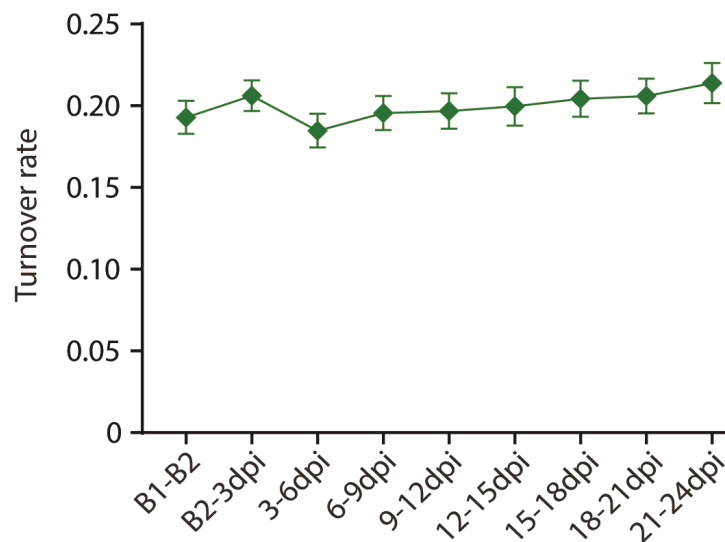


Figure 21. Mean spine turnover of layer V pyramidal neurons in GFP-M mice. Turnover did not significantly change over time, regardless of injury (One-way RM ANOVA with Bonferroni's post hoc testing; $n(\text{animals}) = 4$, $n(\text{dendrites}) = 81$; $n(\text{spines}) = 10.191$).

GFP-M						
N (animals)	4					
N (dendrites)	81					
Mean dendrite length (μm)	63.31 \pm 1.54					
Time-Point	Spine density (Mean/SEM)	Time-Point	Turnover (Mean/SEM)	% Stable (Mean/SEM)	% Eliminat. (Mean/SEM)	% Formed (Mean/SEM)
B1	0.234 \pm 0.007	B1-B2	0.193 \pm 0.090	80.9 \pm 1.41	19.1 \pm 1.41	19.24 \pm 1.89
B2	0.225 \pm 0.007	B2-3dpi	0.206 \pm 0.084	76.98 \pm 1.28	23.02 \pm 1.28	16.68 \pm 1.44
3dpi	0.210 \pm 0.007	3-6dpi	0.185 \pm 0.093	79.89 \pm 1.45	20.11 \pm 1.45	15.93 \pm 1.83
6dpi	0.194 \pm 0.006	6-9dpi	0.195 \pm 0.093	80.59 \pm 1.38	19.41 \pm 1.38	20.16 \pm 1.98
9dpi	0.191 \pm 0.006	9-12dpi	0.197 \pm 0.098	79.38 \pm 1.45	20.62 \pm 1.45	18.16 \pm 1.97
12dpi	0.185 \pm 0.007	12-15dpi	0.199 \pm 0.106	82.1 \pm 1.37	17.9 \pm 1.37	23.71 \pm 2.32
15dpi	0.190 \pm 0.007	15-18dpi	0.204 \pm 0.099	81.75 \pm 1.36	18.25 \pm 1.36	24.59 \pm 2.22
18dpi	0.196 \pm 0.006	18-21dpi	0.206 \pm 0.011	80.47 \pm 1.54	19.53 \pm 1.54	21.94 \pm 1.92
21dpi	0.197 \pm 0.007	21-24dpi	0.214 \pm 0.012	78.9 \pm 1.57	21.1 \pm 1.57	22.62 \pm 2.64
24dpi	0.194 \pm 0.006					

Table 2. Summary of all measures of spine dynamics at each time-point of the experiment. Data is expressed as the mean \pm SEM of numerical values at each time-point. Rate of stable, eliminated and formed spines are expressed as mean percentage \pm SEM.

Next, elimination, formation rate as well as the rate of stable spines was analyzed. In this respect, it was uncovered that the rate of eliminated, formed and stable spines did not significantly change over time (see Table 2; One-way RM ANOVA followed by Bonferroni post hoc test: elimination rate: $p=0.2337$; stable spine rate: $p=0.2765$; $p=0.0264$). While the rate of stable spines remains around 80% throughout the whole experiment, the rate at which spines are eliminated fluctuates around 17 - 23% (see Table 2). The formation rate fluctuates around 15-24%, not differing much from the overall elimination rate over time (see Table 2).

More importantly, elimination rate and formation rate were also compared to each other separately, in order to get a better idea of how both may balance each other out, or not, at any given time-point. In this case, the formation rate of spines was significantly higher than the elimination rate between 12-15dpi and 15-18dpi, while it was significantly lower than the elimination rate from B2 to 3dpi (see Figure 22). Although not statistically significant, we also observed a higher elimination than formation rate at 3-6dpi (see also Table 2).

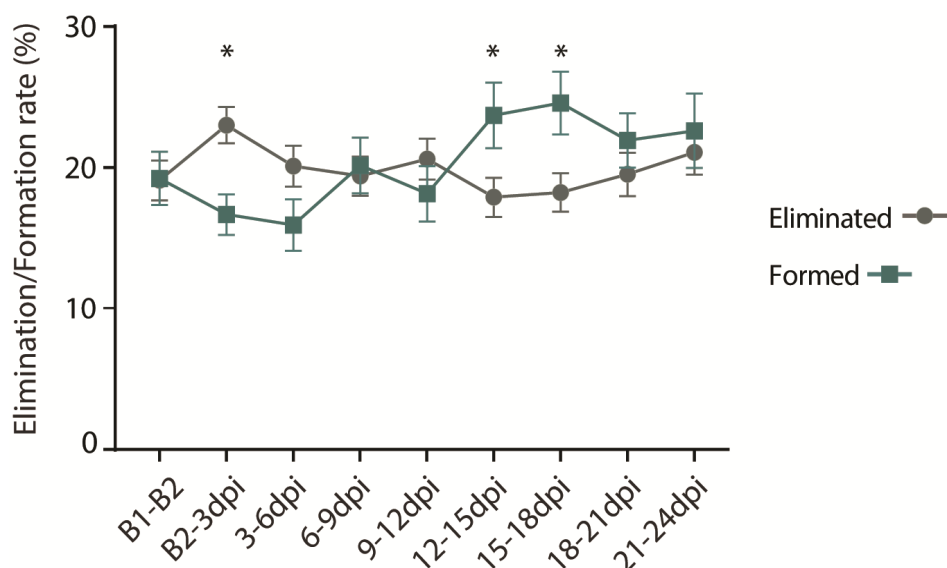


Figure 22. Mean percentage of elimination and formation rate of spines in GFP-M mice. Comparing elimination and formation rate to one another, there is a higher formation than elimination rate between 12-15dpi and 15-18dpi, while there is a higher elimination than formation rate of spines at B2-3dpi. (Two-way RM ANOVA with Bonferroni's multiple comparisons test; * $p < 0.05$; $n(\text{animals})=4$, $n(\text{dendrites})=81$; $n(\text{spines})=10.191$).

3.3.2. Observations based on TCN and CST neurons selectively labelled by retrograde viral tracing

As a second step in our investigation, the influence of TBI on the in vivo spine dynamics of *specifically* TCN in the non-injured hemisphere was evaluated. For this purpose, mice were injected with a retrograde AVV-CAG-GFP to explicitly trace TCNs in the contralateral non-injured hemisphere. Their axons are directly anatomically linked to the injury site and may have been injured through TBI on the opposite side. CST neurons were chosen as a type of control group, in contrast to TCN, because their axons originating in the spinal cord and projecting to the contralesional hemisphere would not be directly connected to the hemisphere affected by TBI. For this purpose, CST neurons in the cortex were visualized by injecting mice with the same retrograde AAV in the spinal cord (thoracic level 8). This retrograde viral tracing approach was efficient enough to perform in vivo two-photon microscopy, as dendrites and spines were sufficiently labelled up to several 100 μm in depth, even at low laser power settings (see Figure 23).

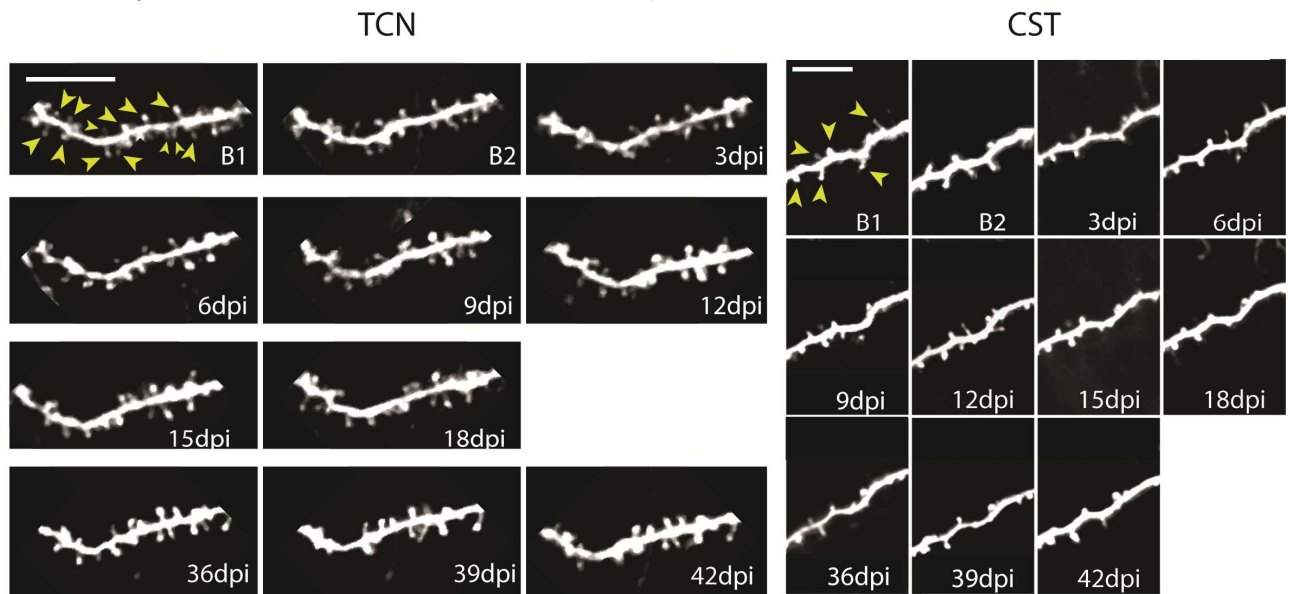


Figure 23. Representative two-photon microscopy images showing a time lapse series of the same apical dendrite originating from a retrogradely labelled TCN (left) and CST neuron (right). Each picture represents a snapshot of a specific dendrite stretch at a specific experimental time-point, followed up to 42dpi days post TBI. Images constitute maximum intensity projections. Arrowheads illustrate examples of spines on a dendrite stretch. B1: Baseline 1, B2: Baseline 2; scale bar: 10 μ m.

However, we could not definitively confirm layer origin of the dendrites imaged for CST neurons, which typically lie in layer V of the cortex, as the fluorescence of the retrograde AAV was not strong enough to be captured by the two-photon microscope at a depth above \sim 300-400 μ m. Therefore we did not have a low resolution overview image with cell bodies, as acquired in GFP-M mice, but only an overview image containing, dendrites and branch points of said dendrites, up to \sim 300 μ m in depth. However, we can be confident that the cell bodies of the dendrites analyzed for CST neurons were deeper than that, and hence in layer V, as no cell body was visible in the low resolution overview image taken, even at that “shallow” depth. As previously reported CST neurons lie below 300 μ m in depth ²⁹⁶. As for TCN, cell bodies of the dendrites that were imaged and analyzed were visible in the overview stack at a more superficial depth (around 200-300 μ m) indicating that they were predominantly originating from TCN in layer II/III. Furthermore, and as previously mentioned, spine density, TOR and elimination/formation rate as well as the rate at which spines remained stable over time were analyzed, as measures of spine dynamics. Figure 24 shows examples of stable, eliminated and formed spines as seen through retrograde viral tracing. The same criteria, as to what is considered to be a stable, eliminated or a newly formed spine, applied as in GFP-M mice.

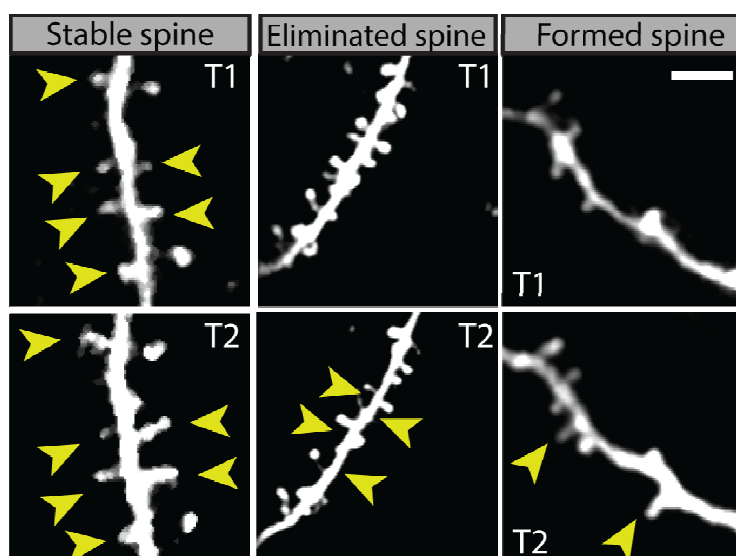


Figure 24. Representative two-photon microscopy images of stable, eliminated and forming spines on dendrites of retrogradely labelled neurons. Only structures clearly protruding from the dendritic shaft were counted as spines (see yellow arrowheads). A spine was considered stable when it was identified at the same location from one time-point (T1) to the next (T2, left panel). Further a spine was considered as eliminated, when the clear protrusion in one time-point could not be found back in the next time-point, having completely disappeared into the dendritic shaft (middle). Finally, we considered a spine to be newly formed, if it was only visible as a novel protrusion from the dendritic shaft at a specific time-point (T2), at a location that previously (T1) did not show any signs of a spine before. Scale bar 5 μ m.

In this respect, for TCN, 23 apical dendrite stretches (sum of number of all spines counted at each time-point for each animal: 8724) of most probably only layer II/III neurons in 3 C57/Bl6 mice over a span of 42 days after injury were imaged. The average length of the dendrite stretches counted was $62.56\mu\text{m} \pm 3.75\mu\text{m}$. In contrast, data for CST neurons were collected from 13 apical dendrite stretches (sum of number of all spines counted at each time-point for each animal: 4376) of cortical layer V neurons in 6 C57/Bl6 mice, equally over a span of 42 days after injury. The average dendrite stretch length was $87.78\mu\text{m} \pm 5.13\mu\text{m}$.

3.3.2.1. In-depth look into the spine dynamics of contralesional TCN after TBI

In the case of TCN, spine density in the contralesional somatosensory cortex did not significantly change, up until 42 days after injury, being the last chronic imaging time-point. At this point spine density drops, when compared to almost all other imaging time-points, but most importantly baseline (see Figure 25 and Table 3). However, only in the case of the second baseline measurements we can see a statistically significant decrease in spine density before and after injury.

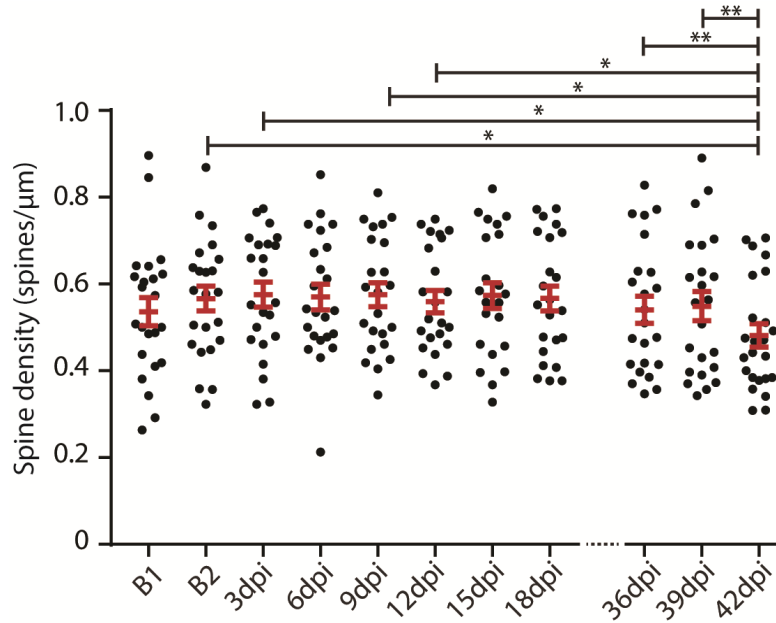


Figure 25. Spine density on apical dendrites of retrogradely labelled TCN.

Each dot represents one dendrite. Spine density in TCN significantly decreases at 42dpi, as almost all time-points show a statistically significantly higher spine density. (One-way RM ANOVA with a Bonferroni post hoc test: * $p < 0.05$; ** $p < 0.01$; $n(\text{animals}) = 3$, $n(\text{dendrites}) = 23$; $n(\text{spines}) = 8724$).

Furthermore, spine TOR of TCN was analyzed before and after TBI. As a result, we found that turnover significantly decreased at 9-12dpi when compared to the turnover at B2-3dpi and 3-6dpi (see Figure 26 and Table 3). This decrease slowly returned to similar levels of turnover before the dip at 39-42dpi.

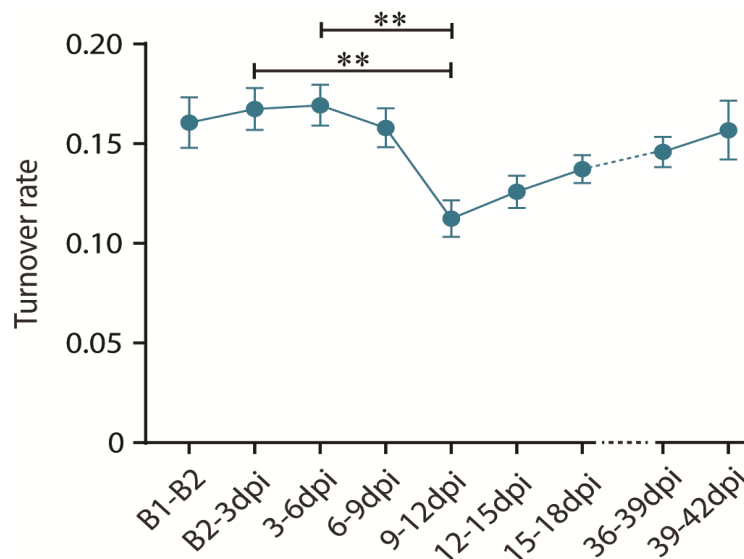


Figure 26. Mean spine turnover of retrogradely labelled TCN.

Turnover in TCN shows a significant decrease between the time-point 9-12dpi and B2-3dpi, as well as 3-6dpi. (One-way RM ANOVA with a Bonferroni post hoc test: ** $p < 0.01$; $n(\text{animals}) = 3$, $n(\text{dendrites}) = 23$; $n(\text{spines}) = 8724$).

TCN						
N (animals)	3					
N (dendrites)	23					
Mean dendrite length (μm)	62.56 \pm 3.75					
Time-Point	Spine density (Mean/SEM)	Time-Point	Turnover (Mean/SEM)	% Stable (Mean/SEM)	% Eliminat. (Mean/SEM)	% Formed (Mean/SEM)
B1	0.536 \pm 0.156	B1-B2	0.161 \pm 0.060	87.01 \pm 0.92	12.99 \pm 0.92	21.28 \pm 3.39
B2	0.567 \pm 0.137	B2-3dpi	0.167 \pm 0.050	84.19 \pm 1.53	15.81 \pm 1.53	18 \pm 1.80
3dpi	0.576 \pm 0.139	3-6dpi	0.169 \pm 0.048	83.04 \pm 1.67	16.96 \pm 1.67	16.88 \pm 2.29
6dpi	0.570 \pm 0.142	6-9dpi	0.158 \pm 0.047	85.34 \pm 1.49	14.66 \pm 1.49	17.73 \pm 2.79
9dpi	0.575 \pm 0.133	9-12dpi	0.112 \pm 0.044	87.95 \pm 1.49	12.05 \pm 1.49	10.04 \pm 1.11
12dpi	0.559 \pm 0.125	12-15dpi	0.126 \pm 0.039	88.45 \pm 1.11	11.55 \pm 1.11	13.9 \pm 1.33
15dpi	0.574 \pm 0.142	15-18dpi	0.137 \pm 0.034	86.1 \pm 1.27	13.9 \pm 1.27	13.46 \pm 1.44
18dpi	0.567 \pm 0.138					
36dpi	0.541 \pm 0.031	36-39dpi	0.146 \pm 0.007	86.07 \pm 1.08	13.93 \pm 1.08	15.56 \pm 1.66
39dpi	0.549 \pm 0.034	39-42dpi	0.157 \pm 0.015	87.01 \pm 0.92	20.23 \pm 1.78	9.461 \pm 2.22
42dpi	0.482 \pm 0.027					

Table 3. Numerical values for spine density, turnover, and percentages of stable, eliminated and formed spines in dendrites of TCN. Data is expressed as the mean \pm SEM of numerical values at each time-point. Rate of stable, eliminated and formed spines are expressed as mean percentage \pm SEM.

Further, rates at which spines newly form, get eliminated or remain stable on the dendrites of TCN were analyzed (see Table 3 and Figure 27). Here, all three rates only significantly differ from previous time-points at 39-42dpi (see Figure 27, left). In particular, we could see a decline in spine stability at 39-42dpi, compared to baseline measurements as well as 9-12dpi and 12-15dpi. Moreover, there were less newly formed spines on the last imaging time-point as compared to B1-B2, B2-3dpi and 3-6dpi. On the other hand spine elimination increased over time, as it was significantly higher at 39-42dpi when compared to baseline measurements, 9-12dpi and 12-15dpi. However, as a whole, stability of spines is not significantly changing over time, but rather fluctuates around the same amount, even after injury, except in the very last imaging time-points (also see Figure 27, left and Table 3), where stability drops (and formation rate as well, while elimination rate increases).

When comparing elimination and formation rates to each other specifically, we could detect that the formation rate between the two baseline measurements was higher than the elimination rate at baseline (see Figure 27, right). The opposite was observed between the last two imaging time-points (see Figure 27, right), where elimination of spines was significantly higher than their formation. In addition, even though not statistically significant, the elimination as well as formation rate decreases at 9-12dpi as opposed to the rates at 6-9dpi and previous time-points. Both rates stay lower than they used to be, except in the last imaging time-point where both diverge in different directions. However, with exception to the last imaging time-point, and although both rates see a decline after 6-9dpi, as a whole formation and elimination rates do not differ much between each other, almost cancelling each other out (also see Table 3).

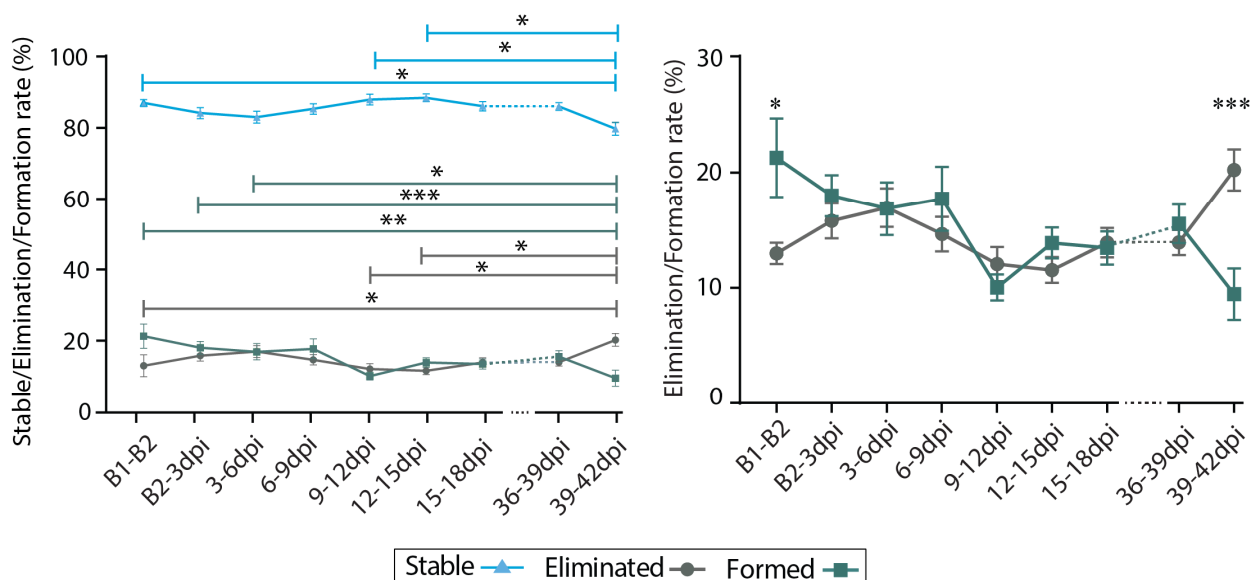


Figure 27. Quantification of stable (blue), elimination (grey) and formation (dark green) rate in TCN (left), as well as a “blow-up” of just the quantification of elimination and formation rate (right). All measures are expressed as percentages \pm SEM. **Left:** TCN show a dip in the stability of their spines, an increase in their elimination and a decrease in their formation by the last imaging time-points (One-way RM ANOVA with a Bonferroni post hoc test, elimination and stable rate * $p < 0.05$; *** $p < 0.001$; formation rate: Friedman’s test with Dunn’s post hoc testing: $p < 0.0001$). **Right:** A closer look at the elimination and formation rate shows statistically significant differences in both rates at the beginning of the imaging session as well as in the very end of it (Two-way RM ANOVA with Bonferroni post hoc test: * $p < 0.05$; ** $p < 0.01$; *** $p < 0.001$; $n(\text{animals}) = 3$, $n(\text{dendrites}) = 23$; $n(\text{spines}) = 8724$).

3.3.2.2. In-depth look at spine dynamics of CST neurons after TBI

Statistically speaking, other than a small increase of spine density between 3dpi and 15dpi, there was no other robust change in spine density over the course of the whole experiment in CST neurons, and especially not before or after the injury (see Figure 28).

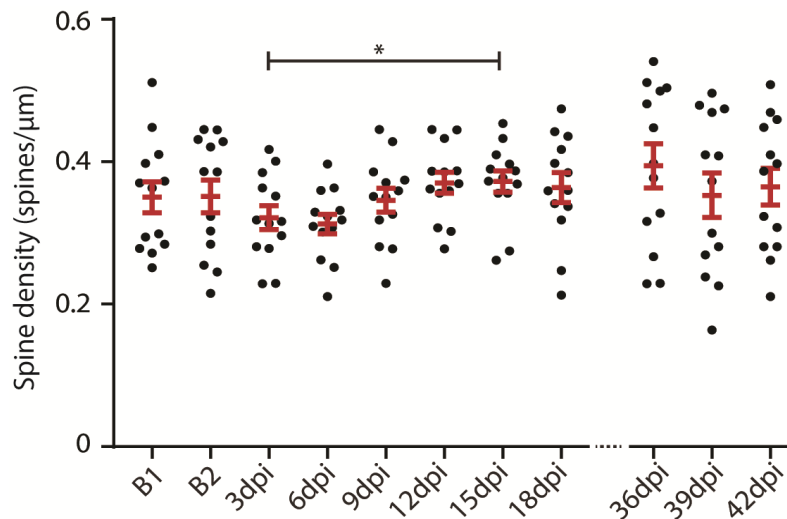


Figure 28. Spine density of apical dendrites of retrogradely labelled CST neurons. Each dot represents one dendrite. Spine density of CST neurons is not different after injury, when compared to baseline measurements. Only a slight increase between 3dpi and 15dpi occurred (One-way RM ANOVA with a Bonferroni post hoc test; * $p < 0.05$; $n(\text{animals})=6, n(\text{dendrites})=13; n(\text{spines})=4376$).

However, Figure 28 and Table 4 show a slight, not statistically significant, decrease of spine density at 3 and 6dpi, compared to baseline. This decline gradually returns to similar levels as in the baseline at 9dpi and later even exceeds levels of spine density at baseline. Finally, spine density recovers to baseline levels at 39dpi. In general, as Table 4 shows, changes in spine density are happening within a small range.

With regard to spine turnover, CST neurons exhibit a statistically significant dip in turnover from 9dpi to 12dpi (see Figure 29). Interestingly, this dip in turnover is similar to that seen in TCN neurons, in the sense that it happens around the same time frame and the observed decrease gradually returns to similar “pre-dip” levels.

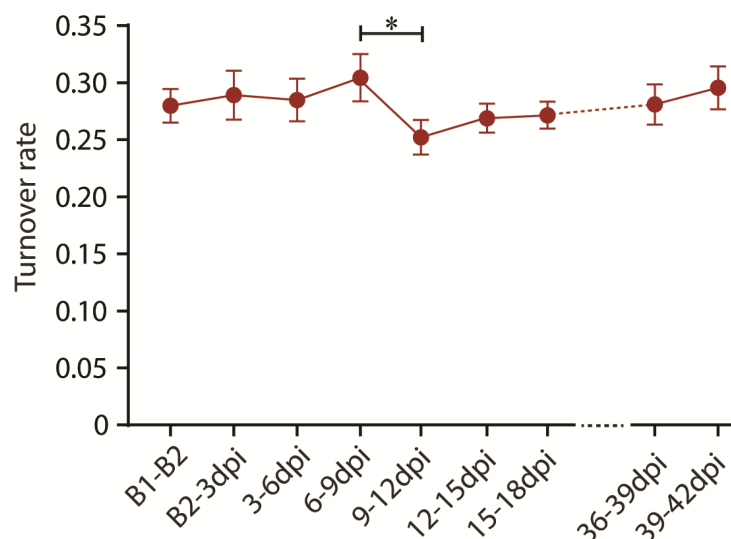


Figure 29. Mean spine turnover in retrogradely labelled CST neurons. CST neurons only show a slight dip in turnover at 9-12dpi, when compared to the previous time-point. (One-way RM ANOVA with a Bonferroni post hoc test, * $p < 0.05$; $n(\text{animals}) = 6$, $n(\text{dendrites}) = 13$; $n(\text{spines}) = 4376$).

CST						
N (animals)	6					
N (dendrites)	13					
Mean dendrite length (μm)	87.78 ± 5.13					
Time-Point	Spine density (Mean/SEM)	Time-Point	Turnover (Mean/SEM)	% Stable (Mean/SEM)	% Eliminat. (Mean/SEM)	% Formed (Mean/SEM)
B1	0.350 ± 0.022	B1-B2	0.280 ± 0.015	72.19 ± 1.66	27.81 ± 1.66	28.79 ± 3.95
B2	0.351 ± 0.023	B2-3dpi	0.289 ± 0.021	69.32 ± 3.28	30.68 ± 3.28	25.13 ± 3.53
3dpi	0.321 ± 0.017	3-6dpi	0.285 ± 0.018	71.28 ± 2.90	28.72 ± 2.90	27.99 ± 3.94
6dpi	0.313 ± 0.014	6-9dpi	0.304 ± 0.021	73.27 ± 1.89	26.73 ± 1.89	38.21 ± 4.31
9dpi	0.346 ± 0.017	9-12dpi	0.252 ± 0.015	77.96 ± 2.19	22.04 ± 2.19	30.43 ± 2.77
12dpi	0.370 ± 0.015	12-15dpi	0.269 ± 0.012	73.46 ± 1.75	26.54 ± 1.75	27.48 ± 2.35
15dpi	0.372 ± 0.015	15-18dpi	0.271 ± 0.012	71.91 ± 1.84	28.09 ± 1.84	25.46 ± 2.55
18dpi	0.364 ± 0.021					
36dpi	0.394 ± 0.031	36-39dpi	0.281 ± 0.018	68.24 ± 2.52	31.76 ± 2.52	21.04 ± 2.00
39dpi	0.353 ± 0.031	39-42dpi	0.295 ± 0.019	72.65 ± 1.88	27.35 ± 1.88	34.46 ± 5.02
42dpi	0.365 ± 0.026					

Table 4. Numerical values for spine density, turnover and percentages of stable, eliminated and formed spines in dendrites of CST neurons. Data is expressed as the mean \pm SEM of numerical values at each time-point. Rate of stable, eliminated and formed spines are expressed as a percentage \pm SEM.

CST neurons did also not exhibit drastic statistically significant fluctuations in their elimination, formation and stability rate over time. In effect, only the stable spine rate and the formation rate between 9-12dpi was significantly higher than the rates at a later time-point, namely 36-39dpi (see Figure 30, left). Both rates reach their lowest point at 36-39dpi, but then shoot up again at 39-42dpi (the same is true for the elimination rate but inversely; see Figure 30, left and Table 4).

In more detail, we also compared elimination and formation rate to each other. Here, we could see that the formation rate of spines was significantly higher than the elimination rate at 6-9dpi and the other way around at 36-39dpi (see Figure 30, right). Furthermore, Figure 30 (right) and Table 4 show that elimination is higher than formation rate at B2-3dpi, but not statistically significant.

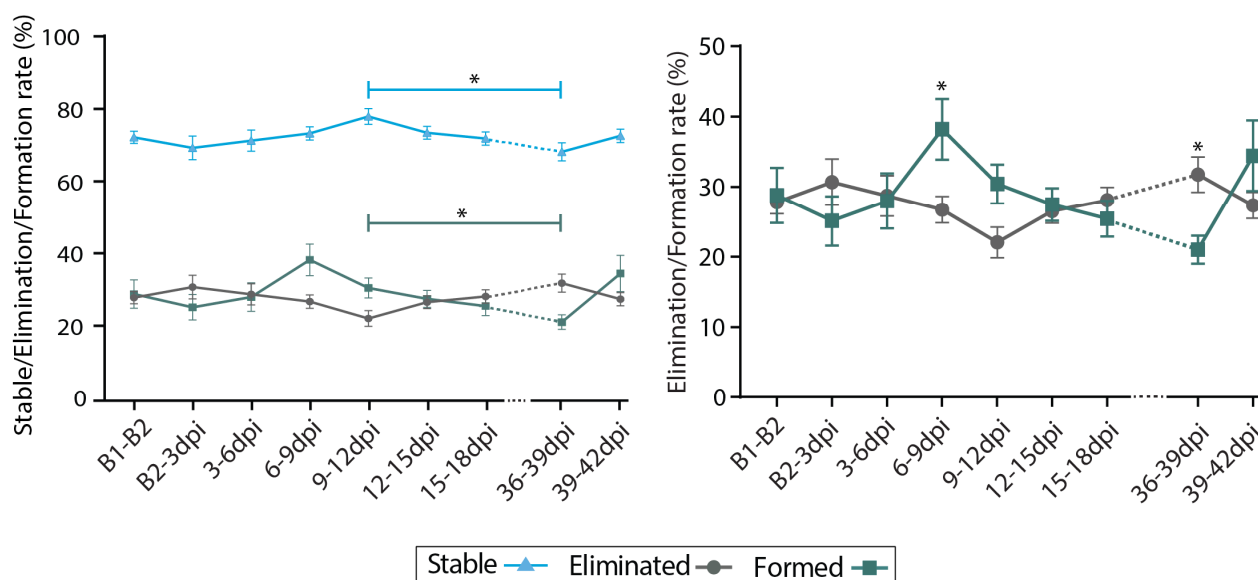


Figure 30. Quantification of stable (blue), elimination (grey) and formation (dark green) rate in CST neurons (left), as well as a “blow-up” of just the quantification of elimination and formation rate (right). All measures are expressed as percentages \pm SEM. **Left:** CST neurons only show a dip in the stability of their spines and their formation rate, between 9-12dpi and 36-39dpi, as revealed by a non-parametric Friedman’s test with Dunn’s post hoc testing (stable and elimination rate: $p = 0.06$, formation: $p = 0.1924$). **Right:** A closer look at just the elimination and formation rate shows that only the 6-9dpi and the 36-39dpi time-point show a statistically significant difference between both rates (Two-way RM ANOVA with Bonferroni post hoc test: * $p < 0.05$; $n(\text{animals}) = 6$, $n(\text{dendrites}) = 13$; $n(\text{spines}) = 4376$).

3.3.3. TCN and CST are inherently different in their spine dynamics

Since TCN and CST neurons were noted to be different in their spine dynamics in the observations made above, they were also compared as a whole in more detail below. In this respect, TCN had a significantly higher spine density in total when compared to CST neurons (see Figure 31, right). In contrast, they exhibited a significantly lower turnover (see Figure 31, right). Both populations exhibit a dip in turnover at the 9-12dpi time-point.

In terms of TOR, GFP-M animals lie in between TCN and CST neurons (see also Tables 2, 3 and 4). TCN animals overall have the lowest turnover, while CST neurons show the highest turnover. For time-points that can be compared (i.e. were imaged in all experimental groups), GFP-M animals have a significantly higher turnover than TCN-animals between the time-points of 9dpi and 18dpi (Ordinary two-way ANOVA with Bonferroni post hoc test: 9-12dpi: $p < 0.0001$, 12-15dpi: $p < 0.0007$; 15-18dpi: $p < 0.0025$) and a lower turnover than CST neurons (Ordinary two-way ANOVA with Bonferroni post hoc test: B1-B2 $p = 0.0018$, B2-3dpi: $p < 0.0032$; 3-6dpi: $p = 0.0002$, 6-9dpi: $p < 0.0001$, 12-15dpi: $p = 0.0188$, 15-18dpi: $p = 0.0241$).

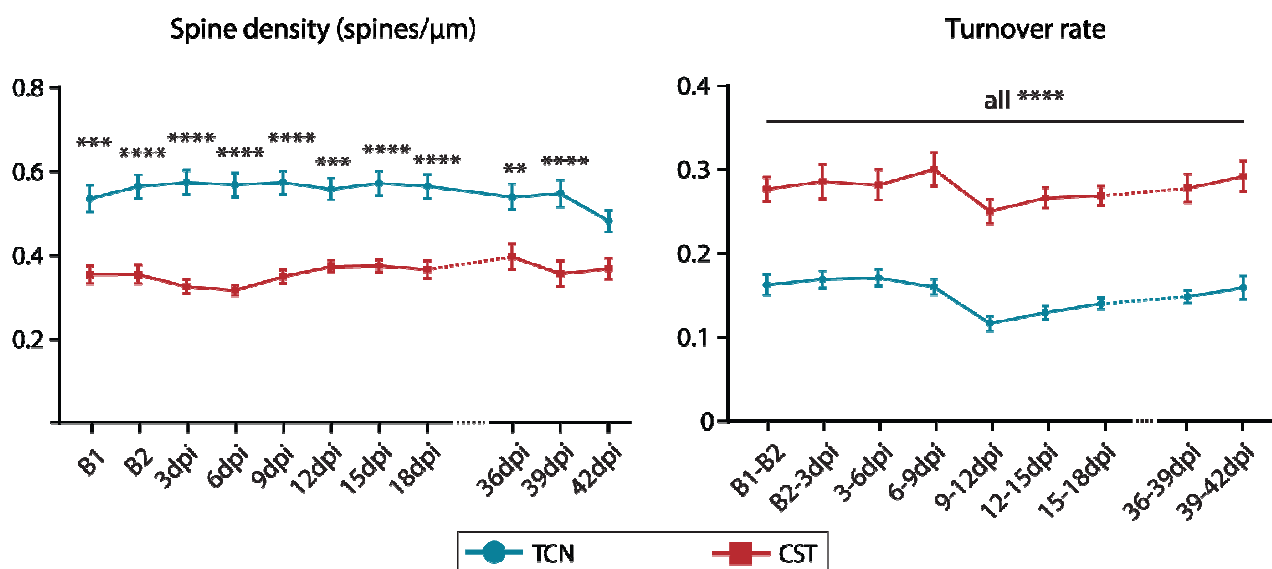


Figure 31. Comparison of mean spine density between TCN (blue) and CST neurons (red; left) and turnover (right). Left: When comparing spine densities between CST neurons and TCN we observed that TCN have a much higher spine density in general (Two-way RM ANOVA with Bonferroni post hoc test: $**p < 0.01$, $***p < 0.001$, $****p < 0.0001$). Right: The opposite is true when comparing the turnover of TCN and CST neurons, as TCN seem to have a significantly lower turnover than CST neurons (Two-way RM ANOVA with Bonferroni post hoc test: $p^{****} < 0.0001$).

Further, in comparison to GFP-M animals, neurons traced with our retrograde virus technique displayed a significantly higher mean spine density, calculated over all the time-points combined (see Figure 32). In general, layer V pyramidal neurons in GFP-M mice have an average spine density of $0.2 \text{ spines} \pm 0.002 / \mu\text{m}$, while both virally traced TCN and CST neurons show a significantly higher average spine density (TCN: $0.55 \pm 0.008 \text{ spines}/\mu\text{m}$; CST-neurons: $0.35 \pm 0.006 \text{ spines}/\mu\text{m}$).

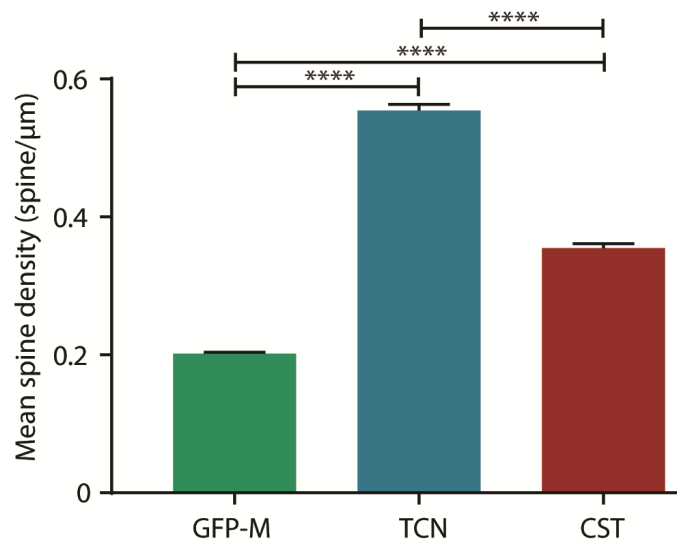


Figure 32. Mean spine density over all time-points on dendrite stretches of neurons in transgenic animals (GFP-M, green), and in retrogradely labelled via viral AAV tracing TCN (blue) and CST neurons (red). Dendrites of transgenic GFP-M mice have a significantly lower spine density compared to both TCN and CST neurons labelled via viral tracing. Ordinary one-way ANOVA with Bonferroni's multiple comparisons test: **** $p < 0.0001$.

Furthermore, when comparing the formation and elimination rate of only the virally traced neuronal sub-populations (TCN vs. CST neurons), we observed that in general TCN had a higher rate of stable spines, while their elimination and formation rate is lower than in CST neurons (see Figure 33, left, centre, right). In fact, TCN fluctuated around a stability rate between 83-88% over time, while spines in CST neurons remained stable at a rate between 68-77% (see Figure 33, left). On the other hand the elimination rate for TCN ranged from 11-20% over time and in CST-neurons from 22-31% (see Figure 33, centre). Interestingly though, for their stability and elimination rate both neuronal subtypes follow a similar curve of fluctuation over the course of the experiment. In contrast their formation rate does display more diverging paths over time, but only for specific time-points, especially at 6-9dpi and 39-42dpi (see Figure 33, right).

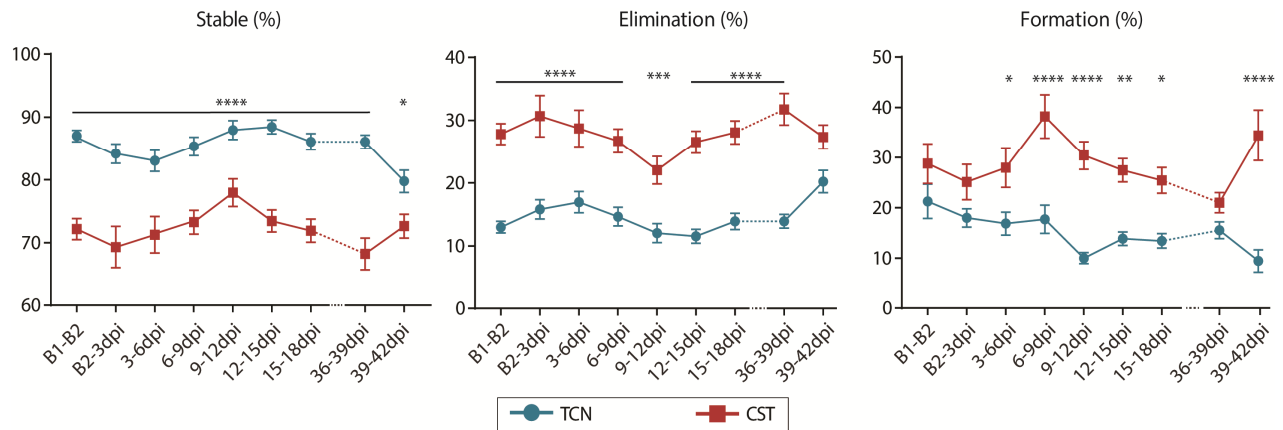


Figure 33. Comparison of quantification of the stable (left) elimination (centre) and formation rate (right) between TCN (blue) and CST neurons (red). Data expressed in percentages \pm SEM. Left: When comparing stability rates of spines between CST neurons and TCN, we observed that TCN have a much higher percentage of stable spines than CST neurons (Two-way RM ANOVA with Bonferroni post hoc test: **** $p < 0.0001$). Middle: Elimination rates seem to follow a similar course over time, however TCN exhibit a lower elimination rate in general (Two-way RM ANOVA with Bonferroni post hoc test: *** $p < 0.001$; **** $p < 0.0001$). Right: The same observation was made when comparing the formation of TCN and CST neurons, as TCN seem to have a lower formation rate than CST neurons, especially at 6-9dpi and 39-42dpi (Two-way RM ANOVA with Bonferroni post hoc test: * $p < 0.05$; ** $p < 0.01$; **** $p < 0.0001$).

Furthermore, GFP-M animals again lie in between TCN and CST neurons when looking at their elimination, formation and stability rate of spines (see respective Tables 2, 3 and 4). TCN show the smallest rate of elimination and formation overall, reflected by their highest rate of stable spines and lowest rate of turnover. In opposition to GFP-M and TCN, CST neurons display the highest rates of elimination and formation, equally reflected in the lowest rate of stable spines overall and the highest turnover.

3.3.4. Survival and persistence of spines in TCN and CST neurons after injury

As a final measure, the survival and persistence of spines throughout the experiment were analyzed for both TCN and CST neurons. For TCN 368 spines on TCN, and 200 spines on CST neurons respectively, were analyzed on 7-9 dendrites.

First, the ratio of initial spines (i.e. present at both baselines) and those that were newly formed after injury (i.e. spines appearing after injury) to that of all spines observed on a dendrite within the experiment was evaluated (see Figure 34). While both CST neurons and TCN have a lower ratio of spines that are newly formed after the injury, compared to the ratio of initial spines, they do not differ in either ratio when compared to each other.

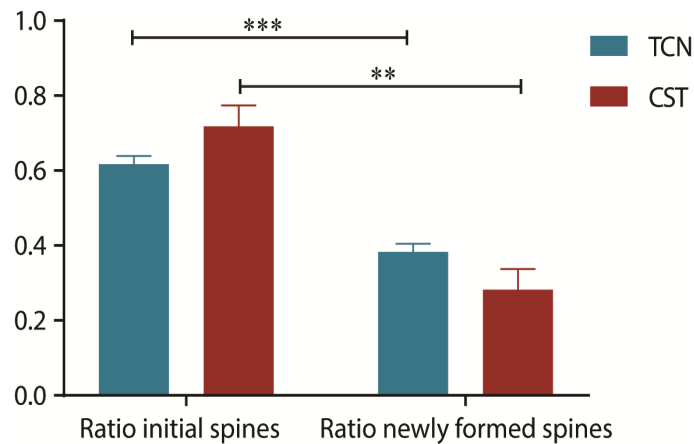


Figure 34. Ratio of spines per dendrite present at the beginning of the experiment (initial spines) and spines that are formed after injury in TCN (blue) and CST neurons (red). TCN and CST neurons have significantly lower ratio of spines that are formed after injury, than spines that were initially present before injury (n(dendrites TCN): 9; n(dendrites CST): 8; TCN: Two-tailed paired t-test $p=0.0009$; CST neurons: Two-tailed paired t-test $p=0.0055$; $**p < 0.01$; $***p < 0.001$). When compared to each other both CST and TCN are not different in their ratio of initially present and newly formed spines (n(dendrites TCN): 9; n(dendrites CST): 8; TCN: Two-tailed unpaired t-test $p=0.07$; CST neurons: Two-tailed unpaired t-test $p=0.07$).

Secondly, both spine categories (initial vs. newly formed spines after injury) were inspected more closely. Firstly, the SF of spines that were present at baseline (i.e. initial spines) was followed after injury as a first measure (see Figure 35). The SF characterizes the amount of spines that survive over the course of each imaging session, as a fraction of the spines that were present at baseline. Over time, the SF of CST neurons and TCN does not significantly differ when compared to each other (see Figure 35).

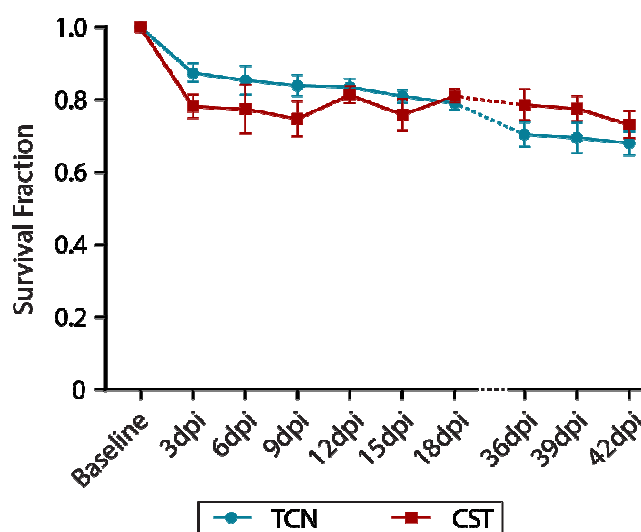


Figure 35. Survival fraction of spines present at baseline per dendrite in TCN (blue) and CST neurons (red). Both neuronal populations do not differ in their survival of spines that are present before injury over time (n(dendrites TCN): 8; n(dendrites CST): 7; Ordinary two-way ANOVA with Bonferroni post hoc test).

In order to possibly uncover more sensitive changes, other than the general survival of spines on each dendrite, the PI was calculated for both initial spines and those that were newly formed after injury. The PI of a spine gives a more detailed idea of how long each individual spine survives at each imaging time-point. Single spines are followed over time and categorized in a “binary matrix” as either present or not present at every imaging time-point. The PI is then calculated as the mean of a binary categorization (“1”: present; “0”: not present) of spines at each imaging time-point. As such a PI of 1 indicates that a particular spine was present at every imaging time-point during the experiment, from the moment it was registered as appearing for the first time. Consequently, in general, the lower the PI the smaller a spines life-time and the more transient it was. In effect, TCN have significantly more initial spines with a longer life-time than CST neurons (see Figure 36). Also from these initial spines, TCN have a higher fraction of spines that are present throughout the whole experiment, even after injury (unpaired two-tailed t-test: $p=0,032$). In fact, on average 51,4% of spines in TCN were present at every time-point (i.e. category “persistent initial spine”), compared to only 36,9% in CST neurons.

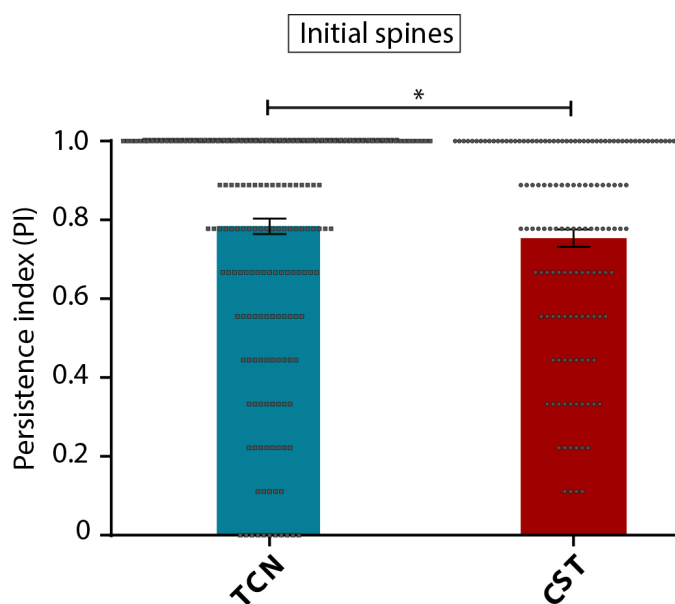


Figure 36. Mean persistence index (PI) of spines present at the beginning of the experiment (initial spines) in TCN (blue) and CST neurons (red). Each dot represents one spine. TCN have a significantly higher ratio of persistent spines compared to CST neurons (Mann-Whitney unpaired non-parametric t-test: $*p=0.03$; TCN: $n(\text{spines})=234$, CST: $n(\text{spines})=145$).

Furthermore contralesional TCN also have a significantly higher fraction of spines with a longer life-time that are newly formed after injury, as indicated by a significantly higher average PI than CST neurons (see Figure 37). In fact, spines that appeared after injury and survived for more than 3 imaging sessions and up until the very last imaging time-point and were thus “persistently gained” or ‘PGI’,

were only present in TCN but not in CST neurons. In more detail, an average of about 18,3% of newly formed spines were persistently gained after injury in TCN compared to none in CST neurons (unpaired two-tailed t-test: $p < 0.0001$).

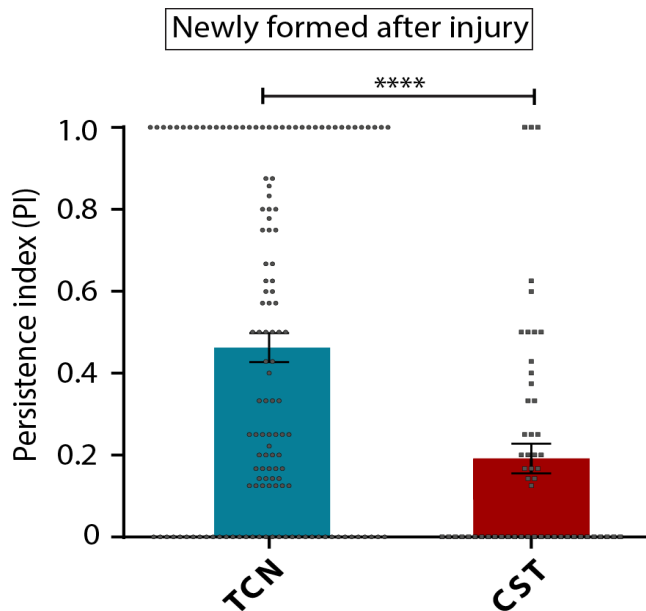


Figure 37. Mean persistence index (PI) of newly formed spines after injury in TCN (blue) and CST neurons (red). Each dot represents one spine. TCN have a significantly higher ratio of spines with a longer life-time compared to CST neurons (Mann-Whitney unpaired non-parametric t-test: **** $p < 0.0001$; TCN: $n(\text{spines}) = 134$, CST: $n(\text{spines}) = 55$).

3.4. Alterations of the circuit structure and organization in the non-injured cortex after TBI

Seeing the interesting changes in spine dynamics in the intact contralesional cortex, and especially in terms of newly formed spines after injury being more robust in TCN than in CST neurons, the final aim of our study was to investigate whether TBI also influences circuit connectivity of TCN on the contralateral side of the injury. In addition, our *in vivo* imaging results showed both early and delayed changes in spine dynamics. Therefore we defined two time-points at which we wanted to map circuit connectivity of TCN after injury, an early time-point (7dpi) and a late time-point (42dpi). In addition we carried out the experiment in one early and one late control group, where animals were not injured, but followed the same surgical and experimental timeline as the injury group. For this purpose we used a modified-rabies-virus-based monosynaptic circuit tracing technique, with the help of Cre-dependent targeting of TCN ²⁹⁷.

Briefly, we retrogradely labelled TCN cell bodies in the contralesional intact somatosensory cortex with a retrograde AAV-cre. In addition, we labelled and

marked these retrogradely labelled TCN with a GFP fluorophore, and the necessary proteins to allow for an “m-Cherry-rabies virus” to infect these TCN and in turn their first-order pre-synaptic partners, via an AAV-TVA-G-eGFP (helper virus) injection. Finally, pre-synaptic partners were labelled by injecting a modified “m-Cherry-rabies virus”. As a consequence of the technique and the fluorophores in question, cells that are TCN, constitute the starting point of the circuit tracing and are positive for GFP and m-Cherry. They are termed starter cells. They appear yellow after image processing under the microscope. Their first-order pre-synaptic partners are only positive for m-Cherry, as the rabies can only jump one synapse, and appear red. Figure 38 shows representative images of both TCN starter cells and their immediate pre-synaptic partners.

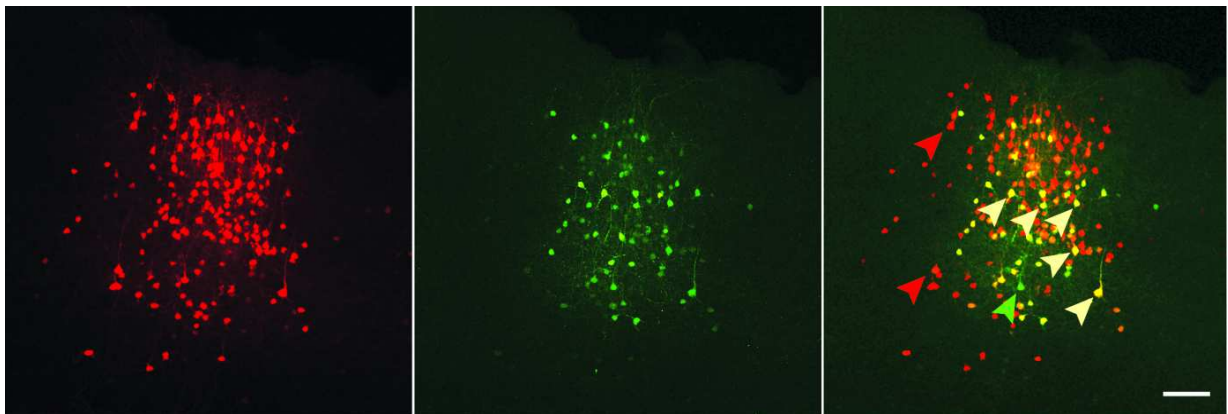


Figure 38. Representative confocal images of m-Cherry-positive pre-synaptic TCN partners (left), GFP-positive TCN (centre) and a merge of both pictures additionally showing GFP- and mCherry- positive starter cells (right). M-Cherry positive cells represent cells that have only been infected by the m-Cherry-rabies virus via mono- and trans-synaptic spread (left). Cells that appear green are representative of TCN, as they have previously been selectively labelled with an AAV-cre. These TCN can only be infected by the second helper virus (i.e. AAV-TVA-G-eGFP), containing GFP as a fluorophore (hence they appear green) and the necessary proteins to allow for, an “m-Cherry-rabies virus” to infect these TCN and in turn their first-order pre-synaptic partners (centre). Merging the images of m-Cherry- and GFP-positive cells reveals starter cells (yellow; off-yellow arrowheads, both positive for m-Cherry and GFP), which constitute the starting point of the circuit mapping (left). Cells that are only positive for m-Cherry (red, red arrowheads) reflect the pre-synaptic partners of the starter cells, as the rabies virus can only jump one more synapse after infecting the starter cell itself. Finally, green cells (green arrowhead) represent a minority of cells that are TCN but did not get infected by the rabies virus. Scale bar: 100 μ m.

3.4.1. Proof of concept: Mono-synaptic tracing of circuit connectivity with modified-rabies and cre-dependent targeting of TCN

To ensure that our viral tracing technique is specific in its labelling of neurons, we also injected animals with just the cre-dependent AAV-TVA-G-eGFP helper virus (see Figure 39), and just the modified-rabies virus (see Figure 40).

In effect, the cre-dependency of AAV-TVA-G-eGFP means that this helper virus should not be able to infect cells without “cre” and label them. As a matter of fact, Figure 39 shows no trace of a labelled cell, in the absence of AAV-cre.

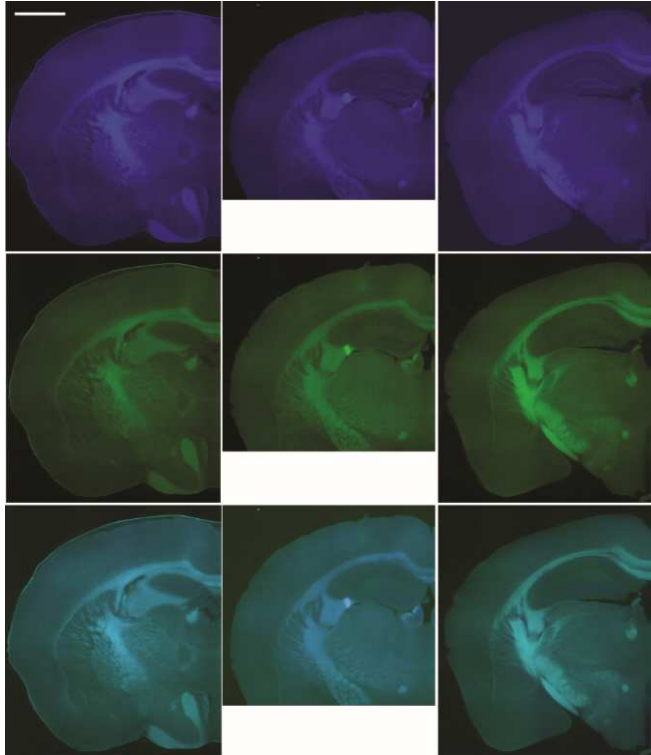


Figure 39. Representative confocal images of brain tissue injected only with AAV-TVA-G-eGFP at different levels of the mouse brain. Top row: Neurotrace 435 staining; Middle row: AAV-TVA-G-eGFP; Bottom row: Merge of both images. To ensure that our helper virus would not infect cells non-specifically, we solely injected cre-dependent AAV-TVA-G-eGFP without injecting animals with AAV-cre prior. Animals used for proof of concept experiments were sacrificed after 14 days post injection. Thus we also abided by the same expression time the virus had during the real experiment. As is visible no cells were labelled by the AAV-TVA-G-eGFP helper virus (see middle row, green). Scale bar: 50 μ m.

In turn, the modified-rabies virus requires the helper virus, as it cannot infect cells without a TVA-receptor protein (only present through infection of AAV-TVA-G-eGFP) and can further not jump one more synapse to infect pre-synaptic partners without G-protein complementation (solely given through AAV-TVA-G-eGFP presence). Again, we observed no labelling of cells, when only the modified-rabies virus was injected into the brain (see Figure 40). The AAV-cre did not have a fluorophore “attached” and was thus not tested. However, our previous in vivo two photon imaging experiments using a retrograde AAV-GFP showed that we can confidently retrogradely trace neurons to the contralateral hemisphere, indicating they are TCN.

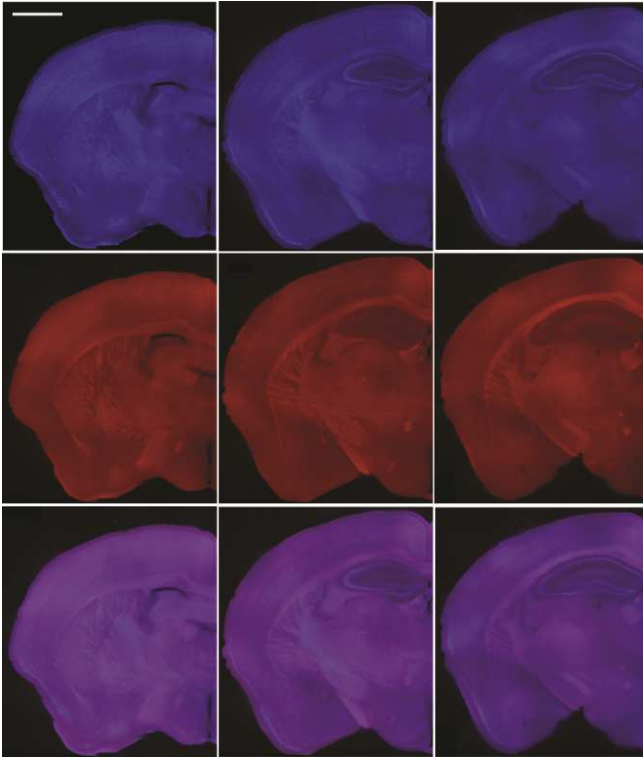


Figure 40. Representative confocal images of brain tissue injected only with modified-rabies virus SAD- Δ G-mcherry (EnvA) at different levels of the mouse brain. Top row: Neurotrace 435 staining; Middle row: SAD- Δ G-mcherry (EnvA; RABV- Δ G-EnvA); Bottom row: Merge of both images. To ensure that our rabies virus would not infect cells unspecifically, we injected SAD- Δ G-mcherry (EnvA) without injecting animals with AAV-TVA-G-eGFP or AAV-cre. The animal used for proof of concept experiments was injected with just the modified-rabies virus and sacrificed 7 days after injection. Thus we also abided by the same expression time the rabies virus had during the real experiment. No cells were labelled by the rabies virus without G-protein complementation and the presence of a TVA-receptor, thus confirming its specificity (see middle row, red). Scale bar: 50 μ m.

3.4.2. Starter cell quantification

In order to map the brain circuit of contralesional TCN after injury, we first analyzed the starter cell population, by quantifying the total number of starter cells in each experimental animal. In brief, we fitted the number of starter cells, for each section analyzed, to create a curve, by polynomial curve fitting and thus an estimate of the total number of cells in each brain. In order to make sure that all experimental groups have the least amount of variability possible between each other, we evaluated the spread of starter cells throughout the brain in a rostro-caudal direction as well as the location of their peak (in terms of maximum number of cells). Outliers were removed accordingly, meaning that only animals with 70% of their starter cells lying between 1.5 and 2.36 relative to Bregma and at least one “peak” (3 sections with the highest number of cells) within the coordinates 1.5 and 2.36 relative to Bregma were included.

Finally we also determined that control animals of early and late time-points did not differ significantly in their number and distribution of starter cells (unpaired two-tailed t-test: $p=0.7462$), and were consequently pooled together as a whole. The final distribution of starter cells and their interpolated number within each animal can be seen in Figure 41.

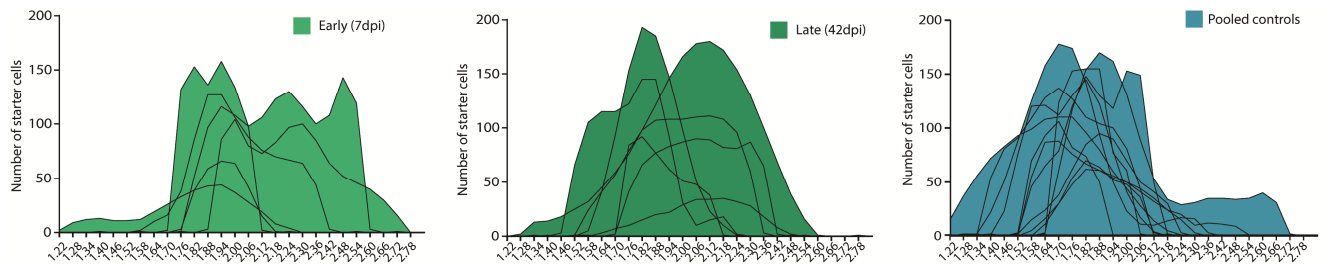


Figure 41. Rostro-caudal distribution of starter cells for each experimental group. The X-axis shows the coordinate of the section (from 1.22 to 2.78 relative to Bregma) interpolated by polynomial curve fitting, while the Y-axis shows the total number of cells interpolated at the specific section. Each line corresponds to an individual animal within each experimental group: Early time-point (7dpi; n=6): light green (left); late time-point (42dpi; n=8): dark green (middle); pooled controls (n=12): blue (right).

3.4.3. Pre-synaptic cell mapping

3.4.3.1 Number of starter cells and pre-synaptic cells are correlated

Our initial analysis prompted us to investigate whether there would be a correlation between the total number of starter cells and total number of pre-synaptic partners, indicating that more or less starter cells would mean that more or less pre-synaptic partners could be revealed by our monosynaptic rabies-virus tracing. Indeed, we could find that there is a significant correlation between the number of starter cells and the pre-synaptic partners revealed by our circuit mapping (Pearson's r : 0.5552; p = 0.0032, see Figure 42). In fact, the more starter cells there are the more pre-synaptic partners were counted.

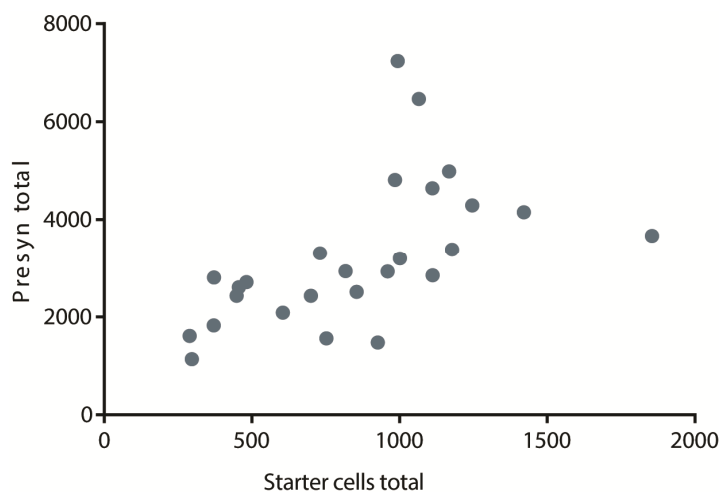


Figure 42. Correlation of total number of starter cells and pre-synaptic cells per animal. Each dot represents one animal. The total number of pre-synaptic partners is correlated to the total number of starter cells (Pearson's r : 0.5552; p = 0.0032).

3.4.3.2 Connectivity ratio of TCN after injury - Layer and time-point specific changes are detectable

Pre-synaptic connectivity of TCN in injured and non-injured animals was analyzed in 20 specific brain regions and expressed with a measure termed connectivity ratio²⁹³. In this respect, the connectivity ratio represents the ratio of the total number of pre-synaptic cells in a given brain area by the total number of starter cells in the given brain. Figure 43 shows examples of pre-synaptic cell spread in an injured and a control animal.

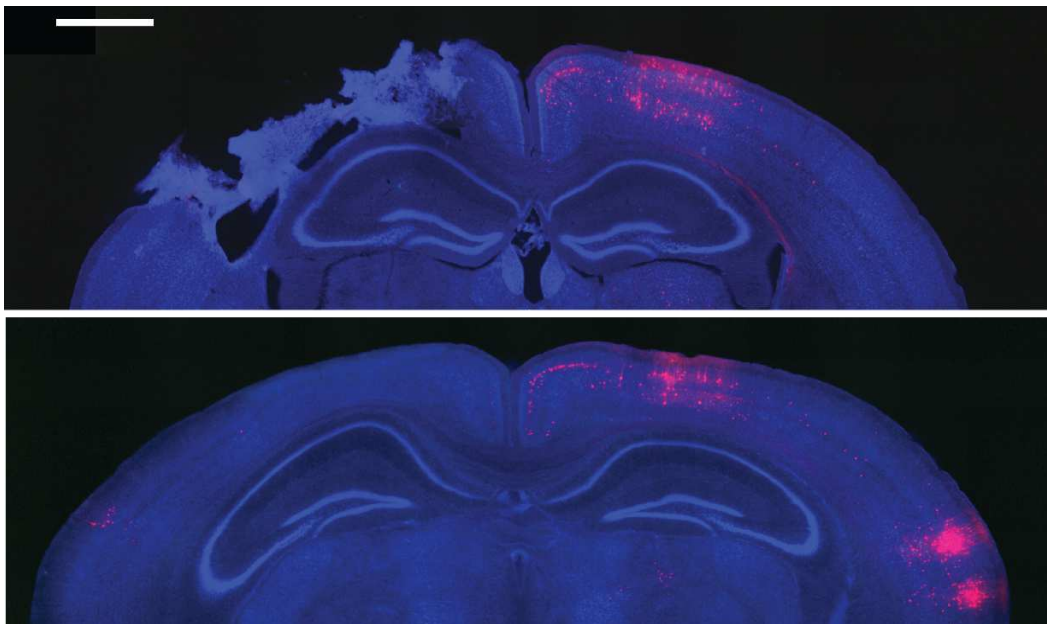


Figure 43. Representative confocal images of pre-synaptic cells in an injured (top) and a control animal (bottom). The injured animal displays damaged tissue at TBI location (left side of the brain). Pre-synaptic partners of TCN are m-Cherry positive from infection with the m-Cherry associated rabies virus. They are distributed in a layer specific fashion and throughout the whole medio-lateral axis of the cortex. Scale bar: 50 μ m.

The analysis of the data shows that pre-synaptic partners of TCN are differentially distributed within the individual brain areas even without injury (as observed by connectivity ratios in control animals (CTRLS)). As such the cortical areas with the most pre-synaptic partners to TCN are the somatosensory (SS) and somatomotor area (MO), as well as the auditory (AUD), retrosplenial (RSP) and posterior parietal association area (PTL; see Figure 44, top). Much less but tangible connectivity was also observed in the anterior cingulate (ACA) and the visual area (VIS). Very low connectivity ratios were found in the temporal association (TEA), entorhinal (ENT), perirhinal (PER) and visceral area (ViscA; see Figure 44, top). With regard to the subcortical areas and white matter structures, the highest connectivity towards

TCN was detected in the thalamus (Thal) (see Figure 44, bottom). In contrast, virtually no connectivity was found in all other areas, whether it was in the control, early (7dpi) or late time-point (42dpi) groups (mean connectivity ratio < 0.04; see Figure 44, bottom). In particular, we found no cells and thus no connectivity of TCN to pre-synaptic partners in the amygdala for all groups.

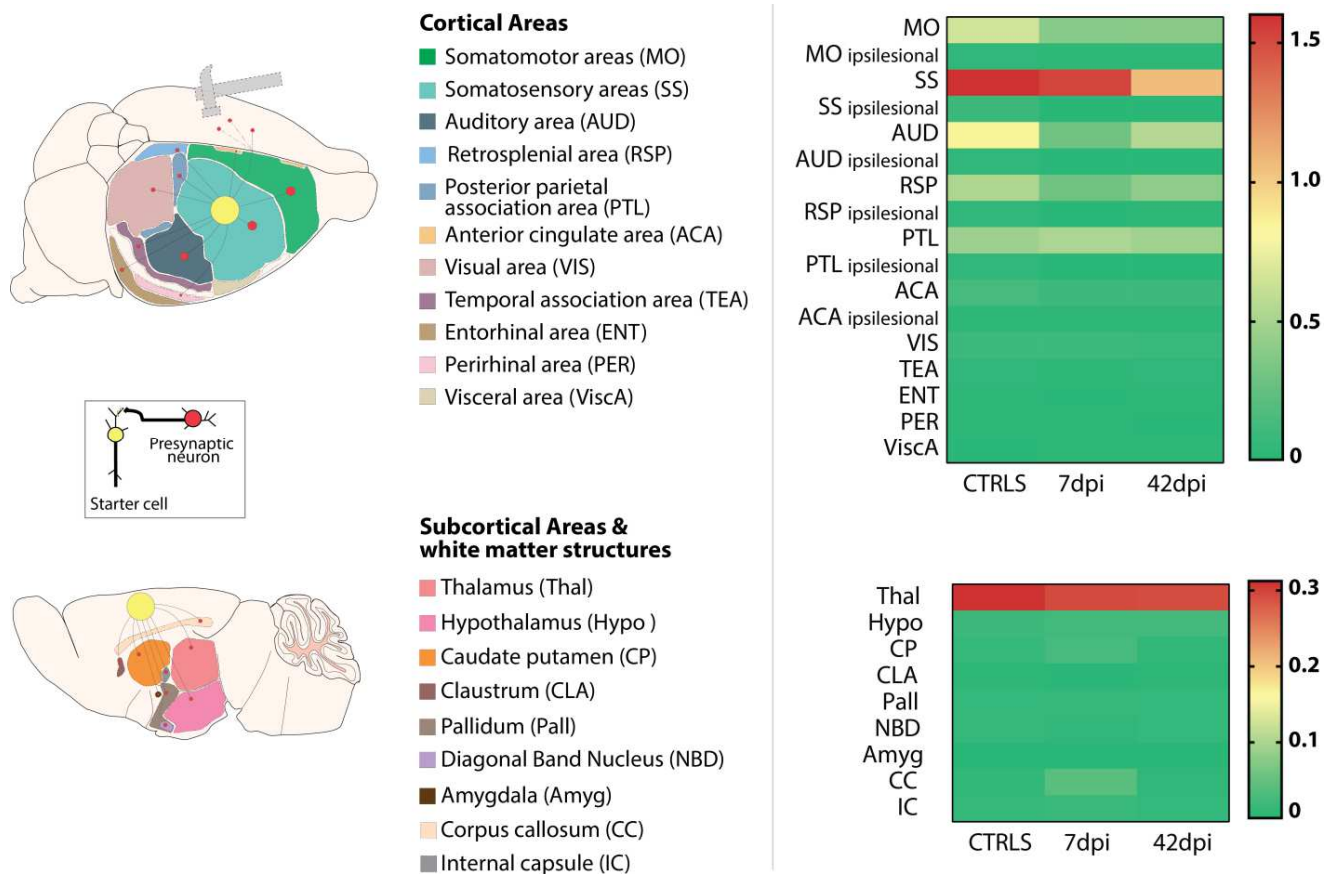


Figure 44. Illustration of areas investigated (left) and heatmaps displaying mean connectivity ratio per group and area (Right; Top right: cortical areas; Bottom right: subcortical areas and white matter structures). Left: Illustrations show the 20 brain areas analyzed in the cortex and subcortical areas, as well as white matter structures like the CC itself. Each area was assigned a colour. In addition yellow dots represent starting point of circuit mapping (i.e. starter cell pool; see inset with scheme of starter cells and pre-synaptic partners). Red circles and their corresponding lines represent possible pre-synaptic partner locations (see inset with scheme of starter cells and pre-synaptic partners) and show how TCN are connected to the areas analyzed. Right: Heatmaps represent the mean connectivity ratio within the different areas for each experimental group (red: higher connectivity ratio; yellow: intermediate connectivity ratio, green: low connectivity ratio). Brain regions described with “ipsilesional” stand for an area counted on the injured side of the brain, in early and late time-points, and thus contralateral to the hemisphere that is intact. Early time-point (7dpi; n=6); late time-point (42dpi; n=8); pooled controls (CTRLS; n=12).

Moreover pre-synaptic connectivity of TCN was also evaluated in the injured cortex of early (7dpi) and late time-point (42dpi) injury groups, in order to further validate our TBI model. As a result, very few, to no cells, were found in the ipsilesional

hemisphere (see Figure 44, areas described with “ipsilesional”). In fact, while control groups did always show a small number of pre-synaptic partners in the “ipsilesional” hemisphere, animals arising from the injured experimental groups did not (see Figure 45). This was especially true for the SS, AUD and PTL, as zero connectivity was found in both early (7dpi) and late time-points (42dpi) in the injured hemisphere (“ipsilesional”). Nevertheless, the MO, RSP and ACA still showed a very small fraction of connectivity (mean connectivity ratio < 0.03), but only in late time-point injured groups. The CLA and ENT also displayed a small mean connectivity ratio in the control as well as 42dpi group, however it was so small (mean connectivity ratio: 3.3244625e-004) that they were not taken into further consideration. Statistical significance could however only be shown in SS areas (see Figure 45).

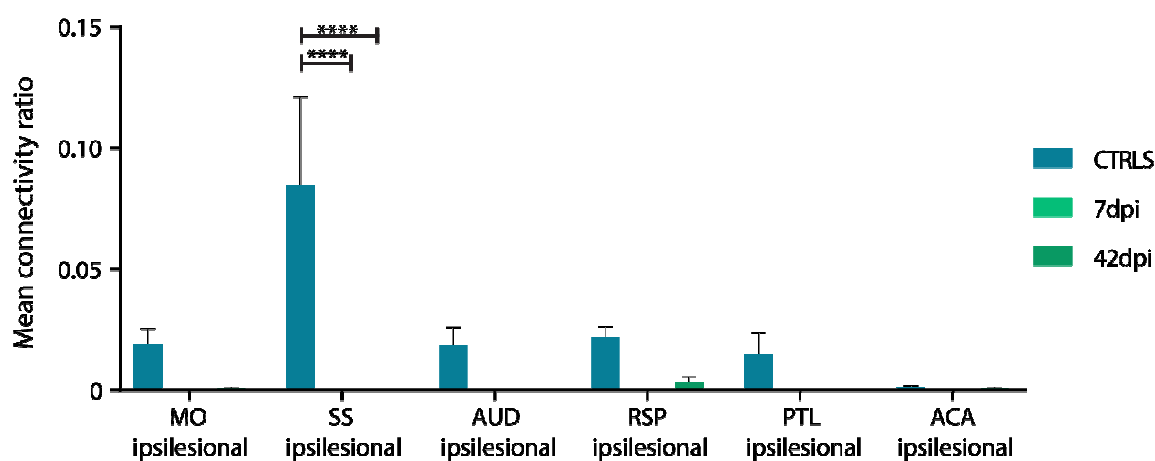


Figure 45. Mean connectivity ratio of areas counted in the “ipsilesional” hemisphere. Control groups show a small but concrete pre-synaptic connectivity of TCN to neurons in the ipsilesional (as dictated by injury groups) hemisphere, with the somatosensory (SS) area displaying the highest connectivity ratio. TCN within the early (7dpi) and late (42dpi) time-point groups show virtually no connectivity to the ipsilesional hemisphere anymore following TBI. Only a small pre-synaptic connectivity is left in the MO, RSP and ACA, but only at 42dpi. Two-way ANOVA with Bonferroni post hoc test: **** $p < 0.0001$; Early time-point (7dpi; $n=6$); late time-point (42dpi; $n=8$); pooled controls (CTRLS; $n=12$).

In a second step, pre-synaptic connectivity of contralesional intact TCN was quantified in the contralesional intact cortex. Here, the areas with the highest connectivity (as determined by the connectivity ratio of control animals) were especially put into focus. Indeed changes in pre-synaptic connectivity of contralesional intact TCN were uncovered when comparing our experimental groups (controls: CTRLS; early time-point: 7dpi, late time-point: 42dpi; see Figure 44 and 46). More specifically, these changes were area- and time-point-specific (see Figure

44 and 46). In this respect, Figure 44 and 46 illustrate that the connectivity ratio of the MO decreases at 7 and 42dpi, when compared to controls. In the case of the RSP, connectivity ratio decreases at 7dpi, but recovers to levels similar to controls at 42dpi. However, statistically significant differences in connectivity ratio were only observed in upper (layers I-IV) of the somatosensory (SS) and auditory areas (AUD; see Figure 46). Connectivity of TCN, specifically in the somatosensory and auditory cortex of the hemisphere that was not directly injured, decreases significantly and long-term after TBI, compared to TCN that have not been injured at all (i.e. controls). Here, as seen in the upper cortical layers of auditory cortex, a decrease of connectivity is already visible in the early time-point group (7dpi) and observationally recovers to a certain extent at 42dpi (see Figure 46). However connectivity ratio does not reach levels of control animals again.

Furthermore, upper cortical layers of the somatosensory area (SS) show a sudden significant decrease of connectivity in the late time-point. Thus, it was observed that connectivity at 7dpi was similar to that seen in control animals, but then only deteriorated by 42dpi. For both the auditory as well as the somatosensory areas, respectively, comparable findings observed in upper layers can also be seen on an observational basis for deeper layers of the cortex. However these did not reach statistical significance.

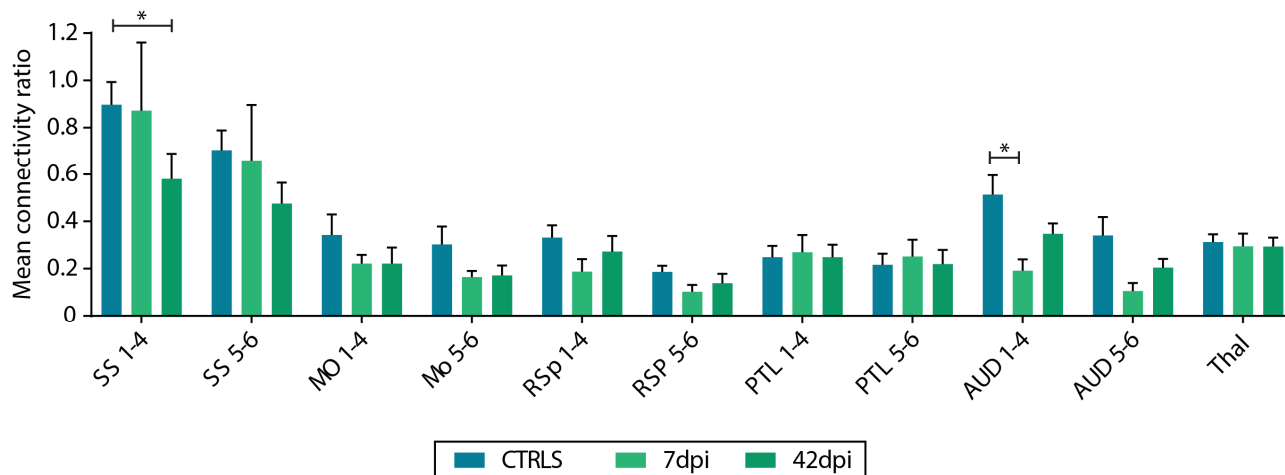


Figure 46. Layer- and area-specific changes in mean connectivity ratio in the somatosensory area (SS), somatomotor area (MO), retrosplenial area (RSP), posterior parietal association area (PTL), auditory area (AUD) and the thalamus (Thal) for each experimental group. Connectivity ratio of contralesional TCN significantly changes in the somatosensory areas of the cortex. Here animals display a much lower connectivity ratio in late time-points (42dpi), as compared to control animals and those in the early time-point group (7dpi). In contrast, the auditory cortex experiences a sudden decrease in connectivity ratio shortly after injury (7dpi), but is able to recover this loss at 42dpi, albeit not to control levels. Lower layers: cortical layers 1-4; Upper layers: cortical layers 5-6. Two-way ANOVA with Bonferroni post hoc test: * $p < 0.05$; Early time-point (7dpi; $n=6$); late time-point (42dpi; $n=8$); pooled controls (CTRLS; $n=12$).

- DISCUSSION -

4.1. Descriptive study of the distribution and location of TCN in the intact mouse cortex

The first part of this thesis was dedicated to systematically and comprehensibly describe and analyze the location and distribution of TCN and their projections throughout the cortex. In this respect, it was determined in which layers they preferably lie and if they are uniformly and homotopically organized in different functional areas (i.e. motor and sensory cortices) of the mouse cortex, or if in fact, depending on the region, their distribution differs. This was done by injecting anterograde and retrograde tracers, such as BDA and FG respectively.

4.1.1. Anterograde tracing of TCN projection patterns

Based on previous reports, that TCN predominantly lie in layers II/III and V ^{144,182} two different depths of BDA tracer injection (i.e. an injection depth corresponding to layers II/III and V respectively) were chosen, in order to investigate if TCN in different cortical layers project to the same cortical column in the homotopic contralateral cortex or not. Both injection depths lead to a similar projection pattern, indicating that TCN in either layers II/III or V project to the same layers overall. However, they both project over the entire homotopic contralateral cortical column and not just some specific layers, albeit with a higher preponderance of projections in layers II-V. This result shows that TCN may project to a much broader population of neurons in different layers, than previously described ¹⁷⁸. In a study using Channelrhodopsin2-assisted circuit mapping, Petreanu et al., (2017) ²⁹⁸ showed that layer II/III callosal neurons mostly project to layers II-III, V and a subset of layer VI ²⁹⁸, corroborating the findings presented in this thesis, at least for layer II/III callosal neurons. In addition, one could argue that the broad projection pattern observed in this thesis, may be caused by using a large amount of anterograde tracer, which could have lead to an “overspill” of it into neighbouring unspecific regions (i.e. injections of BDA in layer II/III may have also been picked up by neurons in much deeper layers and thus clouded the specificity of the results). While there was indeed a slight spread into directly adjacent layers, it did not reach the layers of interest ¹⁷⁸. Moreover both layer II/III and layer V injections showed equal projection patterns, indicating that tracer spread is not a confounding factor ¹⁷⁸. Finally, non-homotopic projections, if any, were more prominently observed with layer V tracer injections ¹⁷⁸. These ectopic projections may play a yet unknown role in inter-hemispheric connectivity ¹⁷⁸.

4.1.2. Retrograde labelling of TCN cell bodies in the intact mouse cortex

Stereotactic injections of the retrograde tracer FG allowed for the analysis of the location and layer distribution of TCN somata in distinct cortical regions (i.e. barrel, somatosensory, and motor cortex).

In more detail, around 60% of TCN were found in the respective homotopic contralateral area of the cortex, regardless of region¹⁷⁸. This in alignment with previous reports that confirm that TCN are a homotopically organized population^{144,159,178,296}. In addition the findings in this thesis also confirm that a considerable portion of TCN reside outside of this homotopic column, in directly adjacent areas and most importantly much further away from the injection site. Such heterotopic connections have also been previously reported: In fact, Fenlon et al., (2017)¹⁵⁹ applied a retrograde tracing approach combined with *in utero* electroporation to the primary somatosensory cortex, as well as the insular/perirhinal area and found, similar to our findings¹⁷⁸, that for both regions heterotopic connections existed¹⁵⁹. Secondly, these heterotopic connections did not coincide with labelling from the area they were initially traced, indicating that both projections arose from their two distinct brain regions (i.e. TCN axons traced from the somatosensory cortex did have cell bodies in the perirhinal area and vice versa, but did not come from the same neuron)¹⁵⁹. In contrast, other studies report that TCN can have dual projections^{144,299}, preferentially from TCN in layer V and not layer II/III¹⁴⁴. As such, these heterotopic connections can represent “mirror images of those within the hemisphere from which they originate” (Nowicka & Tacikowski, (2011), p. 26)¹⁵⁴. Hence a connection of the frontal cortex to the motor cortex on the same side, can also have a heterotopic transcallosal projection to the motor cortex on the opposite side¹⁵⁴ and can either come from a separate and distinct population or from dual projecting neurons. What is more, Wahl and colleagues (2009)³⁰⁰ showed that non-homotopic connections were present in patients with partial agenesis of the CC, but not healthy participants^{178,300}. This shows that these heterotopic connections could play a yet undiscovered role in normal/aberrant CC function and communication or even have a compensatory capacity after injury.

In addition, laminar organization of TCN was analyzed. Here, as previously reported by others^{144,145,182}, TCN cell bodies were observed in layers II/III and layer V¹⁷⁸, with the majority of cell bodies residing in layer II/III. Previous publications have reported as much as 80% of TCN somata residing in layer II/III, in comparison to 20% in layer V¹⁴⁴. Moreover, this thesis showed that about 20% of cell bodies also

resided in layers IV and VI, which gives a more complete look on TCN distribution¹⁷⁸, and has not yet been reported to that extent. Furthermore this layer distribution was quite conserved within the homotopic area, and its laterally and medially adjacent areas.

Finally, it was important to analyze whether TCN have different distributions across distinct anatomically and functionally different cortical regions, in order to elucidate transferability of results within anatomical TCN-tracing studies¹⁷⁸. In the past, most studies have focussed on the somatosensory cortex^{144,145,182,301}. This thesis provides a more thorough overview of TCN distribution. In this respect, laminar distribution was mostly similar across the different cortical regions examined (i.e. barrel, somatosensory, and motor cortex). This confirms, for future researchers, that TCN are a rather homogenous population in terms of overall distribution in the brain, but do show slight differences in layer distribution depending on their anatomical location. Especially non-homotopic areas showed slightly more variation in different regions, suggesting once more that not only homotopic TCN may play a distinct role in CC function and connectivity.

4.2. In-vivo imaging of spine dynamics after TBI in the contralesional intact somatosensory cortex

As has been already laid out in the introduction, the contralesional hemisphere can be affected by injury and has also previously been implicated in aiding functional recovery after unilateral stroke and TBI. Therefore the subsequent focus of this work was to investigate how the intact but anatomically connected hemisphere to the injured side reacts to the loss of input and axonal damage created by TBI, in terms of their spine dynamics.

4.2.1. Spine dynamics after TBI in a mixed non-specific neuronal population

Firstly, the present study provides evidence, that spine dynamics are altered in the intact contralesional cortex after TBI.

In more detail, spine density in layer V neurons in the intact contralesional cortex of GFP-M mice significantly decreases 6 days after injury, compared to spine densities before TBI. Spine density does not come back to pre-injury levels. While spine density showed a statistically significant change after injury, spine turnover did not. In effect, spine turnover remained rather stable over time. However, as seen

in other publications, changes in turnover do not always correlate with changes in spine density^{141,142}. In this case, changes in spine formation and elimination may be more indicative of changes in spine dynamics as a whole. In this respect, it is not the turnover that reflects the lasting loss of spines after injury, but the increased spine elimination in comparison to spine formation between B2 and 3dpi and 6dpi. Moreover, after about 2 weeks post-injury spine formation supersedes elimination up until the last imaging session. This could be a sign that spine loss is beginning to be compensated by an increased formation or re-appearance of spines, and may be the beginning of the recovery of spine density to pre-injury levels. However, this compensatory process may be more gradual and delayed. Thus, it is not yet visible in the spine density measurements, as a steep increase back to pre-injury levels.

In addition, to the best of my knowledge, this thesis posits the first in vivo two photon imaging study of spine dynamics in the contralesional cortex after TBI. The state of research to date is mostly limited to ex vivo investigations of spine characteristics/dendritic branching and other imaging modalities. These mostly confirm the present finding that not only the injured but also the intact contralesional cortex experiences changes in spine dynamics after injury. As such, an immunohistochemical study using CCI as their injury paradigm, uncovered a significant decrease of spine density in neurons of the intact contralateral hippocampus as well as entorhinal and parietal cortex, as soon as 1 day after injury⁸³. Moreover, a stark decrease of hippocampal spine density has also been noted in the contralateral hippocampus, but only arose 1 year after injury³⁰², indicating that changes in spine density are time and brain-region-dependent. Similar findings have been identified after experimental stroke, which can entail similar, but not the same, injury cascades as seen in TBI. Here, Huang et al., (2018)³⁰³ demonstrated that spine density of mushroom spines in deeper layers of the contralateral intact cortex was decreased as soon as 24 hours after stroke, but normalized to sham levels at 28 days post-stroke³⁰³. This speaks for a possible recovery mechanism of spine density, as seen in the present data around 2 weeks after TBI. Here, imaging sessions beyond 24dpi could help uncover whether spine density really comes back to baseline levels following the increased formation of spines (compared to a lower elimination) after about 2 weeks post-injury.

Finally, Takatsuru and colleagues (2009,2011)^{142,304} as well as Johnston and colleagues (2013)³⁰⁵ conducted studies that strongly resembled our experimental setup/question and should be mentioned as such. In their work they also used in

vivo two-photon microscopy to study spine dynamics in the contralateral intact hemisphere, but after experimental stroke^{142,304,305}. While Johnston et al., (2013)³⁰⁵ could not find changes in spine density, turnover (i.e. gains and losses of spines) or SF of spines in the contralateral intact somatosensory cortex after middle cerebral artery occlusion (MCAO), Takatsuru et al., (2009,2011)^{142,304} uncovered that spine dynamics and neuronal activity of the contralateral intact somatosensory and visual cortex were indeed influenced by infarction^{142,304}, thereby corroborating the results presented in this thesis (i.e. the contralateral intact cortex is affected by injury in terms of spine dynamics). In more detail, in one of their earliest studies Takatsuru et al., (2009)¹⁴² showed that phototrombotic stroke in the somatosensory cortex elicited a significant increase of spine elimination and formation of specifically mushroom-type spines 1 week, but not 2 or 4 weeks, after stroke¹⁴². In another experiment the Japanese researchers performed infarction in the visual cortex, and found increased elimination and formation of mushroom but not filopodia-like spines in the intact contralateral cortex³⁰⁴. Spine density remained the same as in sham animals though, since gains and losses of spines happened at the same rate^{142,304}. Takatsuru et al.'s work (2009,2011)^{142,304} does indeed show the influence of injury on the intact hemisphere, as seen in the present work as well, nevertheless the results may vary slightly from the ones in this thesis. In this respect, the most important confounding factor for the reproducibility of results is the difference in injury paradigms (TBI vs. stroke). While experimental stroke does in fact encompass some similar injury mechanisms as observed in TBI, it can probably not fully recapitulate all the intricate consequences that follow an injury from an external force. In addition, Takatsuru et al., (2011)³⁰⁴, predominantly used YFP-H animals for their in vivo two-photon imaging experiments. YFP-H mice constitute a different transgenic line, to GFP-M mice, that mostly labels cortical pyramidal neurons in layer V with yellow fluorescent protein (YFP) instead of GFP²³⁸. This in itself could pose a reason for divergence between the results of this thesis and the study at hand. Joshua Trachtenberg, an experienced scientist in the vivo two-photon imaging field, has in fact argued that using different transgenic mouse lines can explain divergence between different studies, because different mouse lines may label different neuronal subtypes, which can in turn exhibit different behaviour³⁰⁶. Another reason for the discrepancies between studies may include the different choice of how neurons were accessed for two-photon microscopy (i.e. thinning vs. glass CW). As has been well described by Xu et al., (2007)³⁰⁷ and Dorand et al., (2014)²⁴⁷, thinning or chronic CW implantation can create a vastly different outcome in terms of spine dynamics, owed to the different levels of inflammation

both technique create ^{247,307}. Therefore it was important to follow previous guidelines and wait at least 2 weeks after CW implantation in the present thesis, in order for any possible inflammation to subside and minimize the influence of inflammation on the results presented here.

4.2.2. Spine dynamics after TBI in a specific population of TCN and CST neurons

The findings of changes in spine dynamics in the contralesional cortex after TBI in GFP-M animals, represented a catalyst to further dissect how TCN, and thus anatomically connected but intact areas in particular, would react to TBI. In the past, most of the *in vivo* imaging studies on spine dynamics have been limited to the use of transgenic animals ^{109,308-310}. As a result, the neurons that are being investigated usually depict a non-homogenous mix of different neuronal sub-populations. Inferences on specific subtypes are hard to make. Furthermore the most widely used types of transgenic animals used for *in vivo* imaging studies, i.e. YFP-H and GFP-M mice, preferably tag a mixed population of layer V neuronal subtypes²³⁸. In order to label neurons in other cortical layers more abundantly, previous studies have usually resorted to using *in utero* electroporation ^{102,298,311}. This process can be arduous and requires a long waiting time before experimental animals can be imaged at a more mature age. Therefore a more straightforward and less time-consuming technique was needed to investigate more diverse cortical sub-layers, as well as the spine plasticity of specific populations, namely TCN and CST neurons, in this study. Thus the use of just transgenic animals was not sufficient.

As a result, to the best of my knowledge, the present thesis is the first of its kind to specifically label spines on TCN (or CST neurons respectively) and evaluate their *in vivo* spine dynamics longitudinally after TBI, using a quick but precise retrograde virus labelling technique. In order to evaluate possible changes in spine dynamics shortly as well as more chronically after TBI, spines were imaged for up to 42 instead of just 24 days after injury.

Consequently, it was found that spine density of TCN in layer II/III significantly dropped below pre-injury levels late after TBI (i.e. at the very last imaging time-point, 42dpi). In contrast, turnover was not markedly different over time, except for a dip between 9dpi and 12dpi. That said, in general elimination and formation rate consistently balance each other out over time, except for two imaging time-points. For one, between B1 and B2 spine formation is slightly higher than the elimination

rate. Here, the formation rate displayed a higher SEM than the elimination rate, indicating that a single numerical value of formation rate may have incidentally increased the overall mean formation rate, without being detected as a possible statistical outlier and was thus retained in the analysis. Overall, this slight opposition of elimination and formation rate at baseline does however not significantly convert into spine density changes.

More importantly, between 39-42dpi elimination is outweighing formation rate significantly. This large gap between both rates seems to be sufficiently strong to translate directly into a decreased spine density at 39-42dpi. One could argue that the sudden decrease of spine density could be caused by phototoxicity due to the prolonged exposure to the laser light of the two-photon microscope. However, CST neurons who underwent the same imaging timeline did not display such a sudden decrease of spine density, although they were exposed to the same laser power and microscope calibration. In addition, Holtmaat et al., (2005)¹¹⁷ have noted that laser power of up to 4 orders of magnitude higher than the usual light dose used, did not result in photodamage¹¹⁷. Hence, even slightly different and coincidental use of laser power between the two groups could not result in such drastic differences. Therefore the visible changes in spine density may indicate an actual plastic response of TCN to TBI at a more prolonged time-point after injury.

The change in spine turnover at 9-12dpi becomes visible when comparing elimination and formation rate between the imaging time-points of 6-9dpi and 9-12dpi. Here, both elimination and formation drop between those time-points compared to previous time-points, with formation dropping more steeply. This change of rates could cause the change of turnover. In this respect, the drop of both elimination and formation could be a sign for early plastic changes in TCN in response to injury. However, formation rate is still compensated by a similar rate of elimination, leading to no net change of spine density as a whole, even with a changed turnover. This effect of disconnected turnover and spine density is similar to the one seen in studies of Takatsuru et al., (2009, 2011)^{142,304}.

Further down the line, spine dynamics of spines on dendrites of CST neurons were analyzed. Here, CST neurons that were imaged in the intact hemisphere acted as a counterpart to TCN, since they might be influenced by the TBI but are not a population that is anatomically connected to the ipsilesional hemisphere, like TCN. In order to visualize CST neurons in the cortex, CST axons passing the dorsal column of the spinal cord were retrogradely traced to the cortex via a spinal cord

injection of the same retrograde AAV as TCN. More importantly the axons within the dorsal column that were ipsilateral to the TBI were traced, so that only the cell bodies of layer V CST neurons in the intact cortex were labelled. This labelling/tracing outcome has also been confirmed by previous studies^{286,287}. The data in this thesis show that CST neurons, in comparison to TCN, did not drastically change in their spine dynamics after TBI. Firstly, spine density was not significantly different before and after TBI. Interestingly, spine density at 3dpi was significantly lower when compared to spine density at 15dpi, but gradually increased in the time-points in between. Here, the higher formation rate in comparison to elimination rate at 6-9dpi (and albeit not significant at 9-12dpi) could be explanatory of this rise in spine density from 3dpi to 15dpi. Finally, as seen in TCN, at later stages elimination rate significantly exceeds the formation rate of spines, which translates into spine density slightly decreasing from 36dpi to later time-points, but only by trend. Secondly, turnover did not vastly change over time. However, just like in TCN, there was a small decrease between the time-points at 6-9dpi and 9-12dpi. This change in turnover could be explained by a significant increase of spine formation (compared to spine elimination), around that time. Why both sub-populations of TCN and CST neurons show a change in their turnover, is still not clear. However this could be an indication that between 1-2 weeks, or rather in earlier stages after injury, spine dynamics in either population are especially sensitive to injury and foremost with regard to their formation rate. This is plausible given the findings in this thesis and the studies mentioned prior, which indicate that spines in the contralateral intact cortex as a whole can be influenced by injury. In that sense, CST neurons may not be directly anatomically connected to the injury site itself, but can still be influenced by the input loss the injured hemisphere suffers via their connection to affected neurons (for instance TCN). Moreover, some sort of recovery after TBI may also arise from unaffected fibres, namely CST axons. In that sense, Lee and colleagues (2011)³¹² labelled fibres of CST neurons in the contralateral intact cortex after CCI and observed an increase of CST fibres crossing back to the injury-affected part of the CST (i.e. fibres that connect to the injured cortex) on several levels of the spinal cord³¹². This increase in re-crossing fibres was related to functional recovery of motor function³¹² and may also be related to changes of spine dynamics in either cortical hemisphere.

Furthermore this thesis also shows evidence from *in vivo* imaging data that CST neurons and TCN generally display inherently different spine dynamics. In that sense it became apparent, that TCN neurons have a higher spine density than CST

neurons. Conversely, CST neurons have a higher turnover compared to TCN neurons. The reason for this observation becomes apparent when investigating elimination and formation rate of both populations. Here, CST neurons have a consistently more elevated elimination and formation rate throughout the imaging period, compared to TCN. As a consequence of the more prevalent formation and but also elimination of spines on dendrites of CST neurons, they also have a lower population of stable spines than in TCN. Given that TCN and CST neurons hold different functions in the CNS this difference in spine dynamics seems plausible. In fact, Oswald et al., (2013) ²⁹⁶ performed a thorough investigation of morphological and electrophysiological properties of different sub-populations in the primary motor cortex of mice ²⁹⁶. They also showed that CST neurons were inherently different from commissural cortico-cortical neurons: For one CST neurons had bigger cell bodies and more pronounced and thick dendritic tufts than cortico-cortical neurons ²⁹⁶. As seen with the presented data in this thesis, commissural neurons had a much broader layer distribution, than CST neurons which were confined to layer V of the cortex ²⁹⁶. Both subpopulations also exhibited distinct firing properties, with CST neurons having the higher firing rate of action potentials and a more regular firing pattern ²⁹⁶. These data, albeit coming from a different cortical region than investigated in the present work, confirm that TCN and CST neurons that differ in their morphology and firing properties are likely to also have different spine dynamics and be involved in different networks in the intact but also injured brain. Interestingly, the ratio of stable, formed and eliminated spines of neurons in GFP-M animals lie predominantly in between that of CST neurons and TCN. This could reflect the fact that GFP-M neurons are a mixed population of neuronal subtypes that contain both TCN and CST neurons. In terms of spine density, virally traced TCN have the highest spine density, followed by CST neurons and finally neurons in transgenic animals. This could be due to the fact, that the viral expression of the fluorophore is more efficient and leads to more spines being brightly labelled, than when a fluorophore is expressed through transgenic modification. A different reason could be the difference in layer origin between the neurons imaged in GFP-animals (originating in layer V) and those where TCN were virally traced. In this study, imaged TCN were most probably only originating from layer II/III of the cortex. This was the case, because viral injections were placed into more upper layers of the cortex and thus might have been more prone to label their homotopic partners in the same layer. Also, as shown in Chovsepian et al., (2017)¹⁷⁸, TCN cell bodies lie more abundantly in layer II/III compared to deeper layers ¹⁷⁸, increasing the chances of finding more suitable neurons for imaging in

upper rather than deeper layers. Finally, it has been shown that TCN in layer V have much thinner and less pronounced apical tufts, that do not always reach the pial surface¹⁴⁵. Hence, the probability of finding suitable dendrites, originating from TCN in layer V, for imaging was also lowered. In addition Tjia et al., (2017)¹⁰² has previously published findings indicating that layer II/III and V pyramidal neurons do indeed have different spine densities¹⁰². As such, layer II/III had a much higher spine density on their apical dendrites than their counterparts in layer V¹⁰². As seen in the results presented in this thesis, spine density in layer II/III neurons was almost twice as high as in layer V pyramidal neurons in the study of Tjia et al., (2017)¹⁰². Similar results of spine density being higher in layer II/III than layer V neurons were previously also observed by Holtmaat and colleagues (2005)²⁹⁵. The observation that CST neurons in layer V have a higher spine density than neurons in layer V of GFP-animals, may also be an indication, that virally traced spines on CST neurons showed a more efficient expression of the fluorophore and were thereby more abundantly labelled. However, since they still belong to the layer V neuron population their spine density is still not as high as seen in virally traced layer II/III neurons.

Moreover the findings of this thesis demonstrate that TCN of layer II/III only show a delayed response to TBI, since their spine density only significantly decreases at 42dpi. In contrast, the mixed population of layer V neurons (in GFP-M animals) experience an early response to TBI, by exhibiting a decrease of spine density at 6dpi. CST neurons do not experience any change in spine density, despite being layer V neurons and technically resemble neurons from GFP-M animals the most. This could stem from the fact that generally data from the CST-group have the smallest sample size out of all data-sets. Hence a statistical effect could have been missed due to lower statistical power.

In general, the discrepancies between TCN and neurons in GFP-M animals may be due to the different layer origin of the neurons imaged. This would be in line with the idea that layer origin is a defining factor on how spines of different layers behave, as seen with layer-dependent disposition of spine densities. As such, the layer-dependent behaviour of spines, in terms of their turnover, has been previously reported in the healthy as well as in the injured brain. In accordance with the findings of this thesis, a previous publication from Holtmaat and colleagues (2005)²⁹⁵ reported that layer II/III pyramidal neurons of the intact somatosensory cortex had a smaller fraction of transient/short-lived spines than layer V neurons,

thus inferring an overall lower spine turnover in upper layers ^{241,295}. Furthermore Tjia et al., (2017) ¹⁰² showed that whisker trimming, comparable to a loss of input after TBI, induced a layer-dependent response for upper and deeper layers of the somatosensory cortex ¹⁰². Here, only layer V neurons experienced a significant increase in spine elimination and formation after whisker trimming when compared to controls, while layer II/III neurons only had a significantly lower formation rate ¹⁰². Other reports, investigating monocular deprivation in the visual cortex of adult mice, showed that the unilateral loss of input did not influence spine formation or elimination of layer II/III neurons but only increased spine formation in layer V neurons ²⁴². Takatsuru and colleagues (2013)²¹⁶ found that a specific pattern of neuronal activity was especially changed in layer II/III neurons of the contralesional somatosensory cortex, hinting at a layer-specific influence of the contralateral intact cortex to functional recovery ²¹⁶. Even within TCN layer specificity seems to play a role: Electrophysiological and histological experiments in the mouse somatosensory cortex revealed that TCN in layer II/III had similar morphologies and membrane properties of regular-spiking neurons to TCN in layer V/VI ¹⁴⁵. However, they differed in their firing properties of spontaneous postsynaptic potentials (amplitude, frequency and decay time), indicating that they are intertwined in different cortical networks ¹⁴⁵ and may thus display different spine dynamics. As a whole it becomes clear, that changes in spine dynamics can be highly layer-dependent and injury can have layer-dependent impact on spines. This could imply that the information extracted from this thesis, specifically applies to the effects of injury on connected neurons on the contralateral intact cortex (i.e. TCN) in the upper layers of the cortex and might not have the same outcome, if TCN in layer V were analyzed. Discrepancies between results coming from layer V neurons in GFP-animals/CST neurons and those from TCN, may thereby not only be due to the fact that GFP-M animals include a mixed population of neuron subtypes (which may or may not contain neurons that are anatomically connected to the lesioned hemisphere), but also because upper and lower layers of the contralesional intact cortex may change their spine dynamics differently after injury.

As a final measure to dissect spine dynamics in brain regions that are either anatomically connected or not directly linked to the lesion site, the survival and persistence of spines in TCN and CST neurons was analyzed. First, the SF of initially present spines for both populations was determined. Here, the SF did not differ between the two different neuronal populations. In fact, both survival rates of spines in the contralateral intact cortex lie within similar ranges of SFs reported in

control or uninjured animals implicated in previous research ^{126,137,249,295,309}. Additionally, these findings are also in line with a comparable study using experimental stroke as their injury paradigm, where SF did not significantly change in the contralateral intact cortex ³⁰⁵.

As an additional and crucial layer of information the persistence/lifetime of spines throughout the experiment was considered with the so called persistence index (PI). In particular, spines that were present in the beginning of the experiment (i.e. in both baseline measurements) and those that newly appeared after injury were taken a closer look at. For both CST neurons and TCN, the ratio of spines that were newly formed after TBI was lower than the spines present from baseline onwards (also referred to as “initial spines”), but did not differ between each other. This, and the stable SF of initial spines, could speak for the fact that both anatomically connected and not-connected neuron types, despite everything, retain a robust capacity to keep the spines that already are overall stable and involved in neuronal circuitry in that same state, even after injury. However, in TCN initial spines had a significantly longer life-time than those in CST neurons, since their PI was significantly higher than in CST neurons. This is also exemplified by the finding that the ratio of spines that is consistently present throughout all the analyzed imaging time-points is higher than in CST. This could be an indication that initial spines in TCN that are already stable and in an established network would have a better capacity to withstand the possible effects of injury than CST neurons.

Interestingly, and most importantly, TCN and CST neurons also differ in the behaviour of spines that are newly formed after TBI. In this respect, TCN have more newly formed spines after injury with a higher PI than CST neurons. This indicates that spines in TCN that are formed after the injury usually have a longer life-time than those in CST neurons, which seem to be of a more transient nature. As a consequence TCN had much more spines that were not only newly formed after injury but also persistently gained until the very last imaging time-point and present for at least 3 imaging sessions (i.e. 9 days). In that sense, previous research has coined that spines that are present for more than 8 days are more likely to be of a stable nature ¹¹⁷. That said, spines that were formed after injury and persistently gained were only observed in TCN and not CST neurons. In this regard, neurons that are connected to the lesion site (i.e. TCN) may have a higher capacity, by necessity since they seem to be more affected by TBI, to compensate for the loss of input in the lesioned hemisphere. These findings are in line with previous reports,

in which layer II/III neurons of the barrel cortex have also been shown to react with a larger fraction of newly persistent spines after whisker removal, in comparison to layer V neurons³¹³. An interesting addition to the data at hand could be to investigate if the morphological features of spines are related to their behaviour and longevity after injury. As a matter of fact, spine morphology has been closely linked to spine dynamics in the past and can be a good indication whether a spine will be of a transient/short-lived or stable nature. Typically, thinner spines (for instance filopodia) and smaller spine-types are attributed to a short-lived fate (from minutes to about 2 days^{97,107,117}) and contain immature synapses^{97,103}. The bigger and more mature a spine is, the more likely it is to have a long life-time and become a stable synaptic connection between neurons (as is the case for mushroom spines)^{97,99,103}. A stable spine in the mature CNS may not be eliminated for a considerable amount of time ranging from weeks to months and maybe even years⁹⁷. In this case, it would be interesting to see if the newly formed spines after injury also tend to have a more mature morphology (for instance mushroom-type spine like) and how this relates to their lifetime. Lastly, it is important to point out, that the presented survival and longevity data for spines do accommodate one caveat: Only a random and smaller subset of dendrites was chosen for analysis of both parameters. Therefore there could be a possibility that by chance dendrites with spines that were generally more stable/persistent were picked.

4.3. The effects of TBI on intact contralesional TCN network organization

The changes of spine dynamics seen in TCN of the intact contralesional cortex, and especially the finding that newly formed spines after TBI had the capacity to be persistently gained, were the reason to further evaluate whether their altered spine dynamics could also translate into actual synaptic alterations in the form of network connectivity changes in the intact contralesional cortex. Such circuit tracing was performed using mono-synaptic rabies virus tracing. Hereby, the first order pre-synaptic partners of TCN in the contralesional cortex, as well as their TCN starter cells, were labelled. The fact that starter cells and pre-synaptic partners were correlated, are a good indication that our tracing technique was overall balanced. Furthermore, fixed tissue of animals having been injected with either only the rabies virus or the essential helper virus (containing the genetic information for G-protein and TVA-envelope complementation), showed no labelling and confirmed that our tracing technique is dependable and the viruses used do not trace

unspecific cells. This is in line with many prior reports validating mono-synaptic rabies tracing as a reliable and important technique ^{280,282,293,314–316}.

Since TCN spine turnover decreased early after injury (a little over a week after TBI), and spine density significantly dropped at much later imaging time-points (namely 42dpi), mono-synaptic rabies tracing of intact TCN circuits was performed at 7 and 42 days after TBI, as well as in uninjured controls. The first interesting finding was circuit connectivity of healthy uninjured TCN. To the best of my knowledge pre-synaptic connectivity of TCN has yet to be described in the way it has been done in this thesis. In this respect, healthy uninjured TCN of the somatosensory cortex primarily and predominantly connect to the somatosensory, somatomotor and auditory cortex as well as the PTL, RSP and the subcortical thalamus. Less but still tangible connectivity was found in the visual and anterior cingulate cortex. Given that TCN have been shown to connect to neuronal partners in the ipsilateral cortex, especially through intralaminar connections between layer II/III and V ²⁹⁸, and play a crucial role in cortico-cortical communication during sensory-motor, visual and auditory tasks this distribution of connectivity makes sense. Additionally, TCN were also found in layer IV ¹⁷⁸ and could explain direct connectivity to the thalamus, which predominantly sends input to layer IV of the cortex ^{317,318}.

Also, pre-synaptic connectivity was almost eradicated in the ipsilesional hemisphere after TBI, further validating the injury model used here: While some pre-synaptic connectivity was found in both hemispheres in the somatosensory, somatomotor and auditory cortex as well as the RSP, PTL and the ACA of control animals, virtually no pre-synaptic cells were observed in the ipsilesional hemisphere of injured animals. This could be attributed to the fact, that TBI damaged the whole area at hand, often leaving a cavity after tissue processing, due to necrosis of the tissue. In some cases small levels of connectivity returned at 42dpi, for example in the RSP. One could argue that some level of connectivity was appropriately restored at later stages post-injury. This re-establishment of connectivity in the injured cortex might stem from cell bodies of pre-synaptic partners in the penumbra of the injury. Cells in the penumbra, and thus further away from the lesion core, can still retain the capacity to recuperate from the injury and thus might be able to re-establish the previous circuit with their post-synaptic TCN. Here, a study using the stroke model of MCAO, demonstrated that layer V neurons of the somatosensory peri-infarct cortex were able to recover from a steep decline in spine number after

infraction and that this recovery was faster in regions of the cortex that were further away from the infarct core and thus better perfused ¹⁹⁰.

Further, looking at TCN in the intact contralesional cortex, no new areas were pre-synaptically connected to those TCN, post-lesion. Control animals, as well as the animals in the 7dpi and 42dpi experimental groups had their synaptic partners within the same brain region. This could be an indication that in general no completely new brain areas containing pre-synaptic partners were sought out or no new circuits were recruited in the contralesional cortex, as a result of the injury. On the contrary, TCN seemed to have only lost, kept or possibly re-established their initial pre-synaptic connections. In this respect, this thesis further uncovered that an initial loss of connectivity of TCN towards the contralesional intact RSP at 7dpi, was partially recovered at 42dpi. The same happened within the auditory cortex, but in a statistically significant way. Functionally, interhemispheric communication through TCN is essential for sound localization in rodents ³¹⁹. A loss of TCN input, as could have been caused by TBI here, has been shown to decrease activity in their contralateral counterparts ^{145,319,320}. Initially this decrease of activity may have led to a transient disconnection of pre-synaptic partners that was re-established at 42dpi. Again, such a capacity to restore pre-existing pre-synaptic connections may arise from post-synaptic TCN partners, whose axons lie further away from the lesion core and thus retained a potential to recuperate better from the damage caused by the TBI. Moreover, intact axons of the CC, which “only” experienced demyelination after TBI, were shown to be able to remyelinate and recover after a week ^{23,31}. Perhaps injured axons in the cortex were able to recover and restore their activity within the cell body in the intact hemisphere, thereby facilitating the re-establishment of connections to prior targets to a certain degree. However, pre-synaptic connectivity never reached control levels again, hinting at an incomplete compensation of the damage caused in the ipsilesional cortex.

As such, although seen in TCN of the intact somatosensory and not the auditory cortex, the fact that TCN showed a considerable amount of spines that were newly formed and persistently gained after injury, may indicate another mechanism of how connections are re-established. The data in this thesis suggest that lost spines could be replaced by the newly formed spines after injury, which form new contacts but on the same target neuron and could then be stabilized to possibly functional synaptic connections. As a result newly formed spines after TBI seem to re-integrate into the same pre-existing circuit as a compensatory mechanism for early loss of

pre-synaptic connectivity. Further, as indicated above, Holtmaat et al., (2005)²⁹⁵ found that spines that were consistently present for over 8 days, had a 93% chance of surviving the remaining imaging time-points in their experimental setup (over 3 weeks and even up to 3 months). The fact that a considerable amount of the newly formed spines on TCN had a life-time of over 9 days indicates that these spines could likely persist longer and actually be stabilized into a lasting functional synaptic connection. Still, at this point in time, these mechanisms do not seem to be efficient enough to re-establish the same connectivity as in controls and might require a longer period of time to do so.

In contrast to a possible recovery of pre-synaptic connections at 42dpi, seen in the auditory cortex, a significant and substantial loss of those synaptic connections was observed in the intact contralesional somatosensory cortex. Here, connectivity ratios at 7dpi were still comparable to controls, while at 42dpi pre-synaptic connections to contralesional intact TCN were significantly lower than in controls. This significant loss of connectivity could arise from TCN whose axons are more significantly affected by the injury because they originate in the actual injury core. In addition, somatosensory TCN exhibit a high number of cortico-cortical connections within the same brain region (the highest pre-synaptic connectivity of somatosensory TCN in control animals was found in the somatosensory cortex). TBI in this thesis was induced in and spanned along substantial parts of the homotopic somatosensory cortex. Therefore the massive input loss, necrosis and axonal damage created within the lesion core might not be possible to recuperate by the homotopic TCN cell bodies on the contralesional side, thus neuronal cortico-cortical connections to their pre-synaptic partners in the somatosensory cortex were more prone to be lost. Interestingly, this late loss of pre-synaptic connectivity in the somatosensory cortex directly ties into to the decrease of spine density at 42dpi observed in the in vivo imaging data of this thesis. Spines are considered to be the gateway of synapses, and the presence of a mature stable spine likely confirms the presence of a functional excitatory synapse and stable circuit connection, as spines and excitatory synapses are considered to be correlated structures⁹⁶. Thus the loss of spines seen in TCN at 42dpi in the in vivo imaging experiment could result in a real loss of (pre-)synaptic connections as seen in our tracing experiment. Interestingly this process does not immediately happen after injury but is rather delayed, indicating both a sensitivity but also a time-dependent level of robustness against injury in contralesional TCN of layer II/III in the somatosensory cortex.

- CONCLUDING REMARKS -

5.1 Descriptive study of transcallosal neurons in the intact mouse cortex

Using retro- and anterograde tracing techniques we could show that TCN are organized mainly homotopically in layers II/III and V of the cortex, but to a lesser extent also in layers IV and VI. This organization seems to be predominantly uniform throughout different cortical areas, such as the somatosensory, motor and barrel cortex, especially in the homotopic area ¹⁷⁸. However, TCN were also found in non-homotopic regions, in which layer distribution was more diverse and even found in ectopic areas. In turn, their projections were observed to extend within the full cortical column.

As a result this study provides a thorough characterization of the organisation and distribution of TCN in different anatomically and functionally distinct regions of the intact mouse cortex, and shows that TCN are more broadly distributed than previously reported. In addition it adds to the previous understanding that non-homotopic TCN may play a distinct role in CC function and connectivity.

5.2 Spine dynamics and circuit connectivity of the contralesional intact somatosensory cortex after TBI

Firstly, this thesis provides evidence that the intact contralesional cortex is indeed structurally affected by TBI in terms of its spine dynamics. This becomes especially clear when looking at the results collected from a mixed neuronal population, by imaging unspecific layer V neurons of GFP-M mice. Here, spine density permanently decreases after 6dpi and is significantly lower to spine density before injury. This is reflected by an increased elimination and decreased formation rate around the same time. In contrast, we observed a significantly higher level of spine formation compared to elimination about 2 weeks after TBI. While these changes were not yet visible in the general spine density, this could be an indication of a slow recovery process towards pre-injury levels of spine density (i.e. spines that were lost previously are being redeemed by an increased formation of spines). While imaging time-points beyond 24dpi could be the key to finding out whether this is true, we can generally conclude that spines in deeper layers of the contralesional intact cortex are vulnerable to TBI early on.

Subsequently, the purpose of this thesis was to investigate whether TBI would create plastic changes in and affect spine dynamics of TCN, a special neuron type that is anatomically connected to the injury site as opposed to non-connected CST

neurons, in the contralesional intact hemisphere. Taken together the findings of this thesis demonstrate that, for one CST neurons did not show drastic changes in their spine dynamics after TBI. Also they consistently and significantly vary in their spine dynamics as whole from TCN.

Moreover, and most importantly, this thesis uncovers that contralesional TCN specifically experience a significant decrease in spine density and network connectivity at more chronic stages after TBI (42dpi), as opposed to earlier changes of spine density seen in GFP-animals. In accordance, discrepancies between how TCN and that mixed population of neurons in GFP-animals react to TBI in a varying time-dependent manner in terms of their spine density (early vs. delayed after injury), could be explained by the circumstance that the neurons imaged in both data-sets came from different cortical layers. In that sense, TCN originated from layer II/III in the cortex, while both CST neurons and neurons analyzed in GFP-animals originated in layer V. Hence, the findings from this thesis as a whole also contribute to a deeper understanding as to how neurons of the contralesional intact cortex may differ in their spine dynamics after TBI, depending on which layer they originate from in the cortex.

Furthermore, this loss of spines seen in two-photon imaging experiments of the contralesional somatosensory cortex at 42dpi, also translated into a reduced pre-synaptic network connectivity at 42dpi, when mono-synaptically tracing pre-synaptic partners of TCN in the intact somatosensory cortex after injury. In contrast, contralesional TCN experienced a significantly decreased pre-synaptic connectivity to the auditory cortex at 7dpi (as compared to controls) that was re-established at 42dpi, showing a potential of synaptic plasticity that may help with functional recovery after TBI. This confirms a capacity of TCN to recover from spine loss caused by TBI, using a compensatory mechanism of re-establishing lost, but pre-existing, connections. As such, these TCN, and thus the anatomically connected contralesional hemisphere, could be crucial in driving functional recovery after TBI. A mechanism which could be responsible for such recovery may be the finding within this dissertation that only TCN had a considerable amount of newly formed spines after injury that were also persistently gained and had an overall longer life-time than CST neurons. Here, lost spines may be compensated by the newly formed spines after TBI and could then re-integrate into their initial circuit as a stable functional synaptic connection.

As a whole my dissertation provides a deeper understanding of how the intact contralesional, and more specifically neurons that are directly connected to the injury, demonstrate a sensitivity to TBI but also possess the capacity to establish plastic compensatory mechanisms to somewhat recover from the damage caused by the lesion. These mechanisms could certainly be used or targeted with regards to therapeutic interventions and help increase the number of possible treatment options for patients suffering from TBI. Nevertheless, further experiments are needed to confirm whether these structural changes also translate into functional changes. For example, one could add behavioural approaches to uncover whether compensatory structural plasticity also manifests as functional recovery of motor and sensory functions.

- REFERENCES -

1. Xiong, Y., Mahmood, A. & Chopp, M. Animal models of traumatic brain injury. *Nat. Rev. Neurosci.* 14, 128–42 (2013).
2. Najem, D. *et al.* Traumatic brain injury: classification, models, and markers. *Biochem. Cell Biol.* 96, 391–406 (2018).
3. Hyder, A. A., Wunderlich, C. A., Puvanachandra, P., Gururaj, G. & Kobusingye, O. C. The impact of traumatic brain injuries: A global perspective. *NeuroRehabilitation* 22, 341–353 (2007).
4. Dewan, M. C. *et al.* Estimating the global incidence of traumatic brain injury. *J. Neurosurg.* 130, 1080–1097 (2019).
5. Rubiano, A. M., Carney, N., Chesnut, R. & Puyana, J. C. Global neurotrauma research challenges and opportunities. *Nature* 527, S193–S197 (2015).
6. Majdan, M. *et al.* *Epidemiology of traumatic brain injuries in Europe: a cross-sectional analysis.* *Articles Lancet Public Health* 1, (2016).
7. Galgano, M. *et al.* Traumatic brain injury: Current treatment strategies and future endeavors. *Cell Transplantation* 26, 1118–1130 (2017).
8. Roozenbeek, B., Maas, A. I. R. & Menon, D. K. Changing patterns in the epidemiology of traumatic brain injury. *Nat. Rev. Neurol.* 9, 231–236 (2013).
9. Schwarzbold, M. *et al.* Psychiatric disorders and traumatic brain injury. *Neuropsychiatric Disease and Treatment* 4, 797–816 (2008).
10. Prins, M., Greco, T., Alexander, D. & Giza, C. C. The pathophysiology of traumatic brain injury at a glance. *DMM Dis. Model. Mech.* 6, 1307–1315 (2013).
11. Nguyen, R. *et al.* The International Incidence of Traumatic Brain Injury: A Systematic Review and Meta-Analysis. *Can. J. Neurol. Sci. / J. Can. des Sci. Neurol.* 43, 774–785 (2016).
12. Mckee, A. C. & Daneshvar, D. H. The neuropathology of traumatic brain injury. in *Handbook of Clinical Neurology* 127, 45–66 (Elsevier B.V., 2015).
13. Pearn, M. L. *et al.* Pathophysiology Associated with Traumatic Brain Injury: Current Treatments and Potential Novel Therapeutics. *Cell. Mol. Neurobiol.* 37, 571–585 (2017).
14. Cernak, I. Animal models of head trauma. *NeuroRx* 2, 410–22 (2005).
15. Nyanzu, M. *et al.* Improving on laboratory traumatic brain injury models to achieve better results. *Int. J. Med. Sci.* 14, 494–505 (2017).
16. Werner, C. & Engelhard, K. Pathophysiology of traumatic brain injury. *Br. J. Anaesth.* 99, 4–9 (2007).
17. Hall, E. D. *et al.* Spatial and temporal characteristics of neurodegeneration after controlled cortical impact in mice: More than a focal brain injury. *J. Neurotrauma* 22, 252–265 (2005).
18. Wiley, C. A. *et al.* Ultrastructure of Diaschisis Lesions after Traumatic Brain Injury. *J. Neurotrauma* 33, 1866–1882 (2016).
19. Harris, N. G. *et al.* Disconnection and hyper-connectivity underlie reorganization after TBI: A rodent functional connectomic analysis. *Exp. Neurol.* 277, 124–138 (2016).
20. Holschneider, D. P., Guo, Y., Wang, Z., Roch, M. & Scremin, O. U. Remote brain network changes after unilateral cortical impact injury and their modulation by acetylcholinesterase inhibition. *J. Neurotrauma* 30, 907–919 (2013).
21. Simon, D. W. *et al.* The far-reaching scope of neuroinflammation after traumatic brain injury. *Nat. Rev. Neurol.* 13, 171–191 (2017).
22. Kraus, M. F. *et al.* White matter integrity and cognition in chronic traumatic brain injury: a diffusion tensor imaging study. *Brain* 130, 2508–2519 (2007).
23. Armstrong, R. C., Mierzwa, A. J., Marion, C. M. & Sullivan, G. M. White matter involvement after TBI: Clues to axon and myelin repair capacity. *Experimental Neurology* 275, 328–333 (2016).
24. Green, R. E. A. *et al.* Scale and pattern of atrophy in the chronic stages of moderate-severe TBI. *Front. Hum. Neurosci.* 8, (2014).
25. Harris, N. G., Carmichael, S. T., Hovda, D. A. & Sutton, R. L. Traumatic brain injury results in disparate regions of chondroitin sulfate proteoglycan expression that are temporally limited. *J. Neurosci. Res.* 87, 2937–2950 (2009).
26. Blennow, K., Hardy, J. & Zetterberg, H. The Neuropathology and Neurobiology of Traumatic Brain Injury. *Neuron* 76, 886–899 (2012).

27. Smith, D. H. & Meaney, D. F. Axonal damage in traumatic brain injury. *Neuroscientist* 6, 483–495 (2000).
28. Johnson, V. E., Meaney, D. F., Cullen, D. K. & Smith, D. H. Animal models of traumatic brain injury. *Handb. Clin. Neurol.* 127, 115–128 (2015).
29. Armstrong, R. C., Mierzwa, A. J., Marion, C. M. & Sullivan, G. M. White matter involvement after TBI: Clues to axon and myelin repair capacity. *Exp. Neurol.* 275, 328–333 (2016).
30. Johnson, V. E., Stewart, W. & Smith, D. H. Axonal pathology in traumatic brain injury. *Exp. Neurol.* 246, 35–43 (2013).
31. Mierzwa, A. J., Marion, C. M., Sullivan, G. M., McDaniel, D. P. & Armstrong, R. C. Components of Myelin Damage and Repair in the Progression of White Matter Pathology After Mild Traumatic Brain Injury. *J. Neuropathol. Exp. Neurol.* 74, 218–232 (2015).
32. Warner, M. A. *et al.* Assessing spatial relationships between axonal integrity, regional brain volumes, and neuropsychological outcomes after traumatic axonal injury. *J. Neurotrauma* 27, 2121–2130 (2010).
33. Namjoshi, D. R. *et al.* Towards clinical management of traumatic brain injury: A review of models and mechanisms from a biomechanical perspective. *DMM Disease Models and Mechanisms* 6, 1325–1338 (2013).
34. Ma, X., Aravind, A., Pfister, B. J., Chandra, N. & Haorah, J. Animal Models of Traumatic Brain Injury and Assessment of Injury Severity. *Mol. Neurobiol.* 56, 5332–5345 (2019).
35. Estrada-Rojo, F. *et al.* Models used in the study of traumatic brain injury. *Rev. Neurosci.* 29, 139–149 (2018).
36. Zweckberger, K. *et al.* Effect of Early and Delayed Decompressive Craniectomy on Secondary Brain Damage after Controlled Cortical Impact in Mice. *J. Neurotrauma* 23, 1083–1093 (2006).
37. Osier, N. D. & Dixon, C. E. The Controlled Cortical Impact Model: Applications, Considerations for Researchers, and Future Directions. *Front. Neurol.* 7, 134 (2016).
38. Lin, G. qing *et al.* Transplanted human neural precursor cells integrate into the host neural circuit and ameliorate neurological deficits in a mouse model of traumatic brain injury. *Neurosci. Lett.* 674, 11–17 (2018).
39. Morganti-Kossmann, M. C., Yan, E. & Bye, N. Animal models of traumatic brain injury: Is there an optimal model to reproduce human brain injury in the laboratory? *Injury* 41, S10–S13 (2010).
40. Pierce, J. E., Smith, D. H., Trojanowski, J. Q. & McIntosh, T. K. Enduring cognitive, neurobehavioral and histopathological changes persist for up to one year following severe experimental brain injury in rats. *Neuroscience* 87, 359–69 (1998).
41. SMITH, D. H. *et al.* Progressive Atrophy and Neuron Death for One Year Following Brain Trauma in the Rat. *J. Neurotrauma* 14, 715–727 (1997).
42. Bramlett, H. & Dietrich, D. Quantitative structural changes in white and gray matter 1 year following traumatic brain injury in rats. *Acta Neuropathol.* 103, 607–614 (2002).
43. Nilsson, P. *et al.* Epileptic seizure activity in the acute phase following cortical impact trauma in rat. *Brain Res.* 637, 227–232 (1994).
44. Chiu, C.-C. *et al.* Neuroinflammation in animal models of traumatic brain injury. *J. Neurosci. Methods* 272, 38–49 (2016).
45. Feeney, D. M., Boyeson, M. G., Linn, R. T., Murray, H. M. & Dail, W. G. Responses to cortical injury: I. Methodology and local effects of contusions in the rat. *Brain Res.* 211, 67–77 (1981).
46. Marmarou, A. *et al.* A new model of diffuse brain injury in rats. *J. Neurosurg.* 80, 291–300 (1994).
47. Thompson, H. J. *et al.* Lateral Fluid Percussion Brain Injury: A 15-Year Review and Evaluation. *J. Neurotrauma* 22, 42–75 (2005).
48. Cernak, I. & Noble-Haeusslein, L. J. Traumatic brain injury: an overview of pathobiology with emphasis on military populations. *J. Cereb. Blood Flow Metab.* 30, 255–66 (2010).
49. LIGHTHALL, J. W. Controlled Cortical Impact: A New Experimental Brain Injury Model. *J. Neurotrauma* 5, 1–15 (1988).
50. Dixon, C. E., Clifton, G. L., Lighthall, J. W., Yaghmai, A. A. & Hayes, R. L. A

- controlled cortical impact model of traumatic brain injury in the rat. *J. Neurosci. Methods* 39, 253–62 (1991).
51. Osier, N. & Dixon, C. E. The Controlled Cortical Impact Model of Experimental Brain Trauma: Overview, Research Applications, and Protocol. *Methods Mol. Biol.* 1462, 177–92 (2016).
 52. SMITH, D. H. *et al.* A Model of Parasagittal Controlled Cortical Impact in the Mouse: Cognitive and Histopathologic Effects. *J. Neurotrauma* 12, 169–178 (1995).
 53. Meaney, D. F. *et al.* Modification of the Cortical Impact Model To Produce Axonal Injury in the Rat Cerebral Cortex. *J. Neurotrauma* 11, 599–612 (1994).
 54. Wang, T. *et al.* Amantadine Improves Cognitive Outcome and Increases Neuronal Survival after Fluid Percussion Traumatic Brain Injury in Rats. *J. Neurotrauma* 31, 370–377 (2014).
 55. Giacino, J. T. *et al.* Placebo-Controlled Trial of Amantadine for Severe Traumatic Brain Injury. *N. Engl. J. Med.* 366, 819–826 (2012).
 56. Kline, A. E., Yan, H. Q., Bao, J., Marion, D. W. & Dixon, C. E. Chronic methylphenidate treatment enhances water maze performance following traumatic brain injury in rats. *Neurosci. Lett.* 280, 163–166 (2000).
 57. Wagner, A. K. *et al.* Chronic methylphenidate treatment enhances striatal dopamine neurotransmission after experimental traumatic brain injury. *J. Neurochem.* 108, 986–997 (2009).
 58. Adelson, P. D. *et al.* Comparison of hypothermia and normothermia after severe traumatic brain injury in children (Cool Kids): A phase 3, randomised controlled trial. *Lancet Neurol.* 12, 546–553 (2013).
 59. Monaco, C. M. *et al.* Environmental enrichment promotes robust functional and histological benefits in female rats after controlled cortical impact injury. *Exp. Neurol.* 247, 410–418 (2013).
 60. Osier, N. D., Korpon, J. R. & Dixon, C. E. *Controlled Cortical Impact Model. Brain Neurotrauma: Molecular, Neuropsychological, and Rehabilitation Aspects* (CRC Press/Taylor & Francis, 2015).
 61. Atkins, C. M., Cepero, M. L., Kang, Y., Liebl, D. J. & Dietrich, W. D. Effects of early rolipram treatment on histopathological outcome after controlled cortical impact injury in mice. *Neuroscience Letters* 532, 1–6 (2013).
 62. Singleton, R. H., Yan, H. Q., Fellows-Mayle, W. & Dixon, C. E. Resveratrol attenuates behavioral impairments and reduces cortical and hippocampal loss in a rat controlled cortical impact model of traumatic brain injury. *J. Neurotrauma* 27, 1091–1099 (2010).
 63. Schaible, E. V. *et al.* Single Administration of Tripeptide α -MSH(11-13) Attenuates Brain Damage by Reduced Inflammation and Apoptosis after Experimental Traumatic Brain Injury in Mice. *PLoS One* 8, (2013).
 64. Dhillon, H. S., Donaldson, D., Dempsey, R. J. & Prasad, M. R. Regional Levels of Free Fatty Acids and Evans Blue Extravasation After Experimental Brain Injury. *J. Neurotrauma* 11, 405–415 (1994).
 65. Glushakova, O. Y., Johnson, D. & Hayes, R. L. Delayed increases in microvascular pathology after experimental traumatic brain injury are associated with prolonged inflammation, blood-brain barrier disruption, and progressive white matter damage. *J. Neurotrauma* 31, 1180–1193 (2014).
 66. Smith, D. H. *et al.* A Model of Parasagittal Controlled Cortical Impact in the Mouse: Cognitive and Histopathologic Effects. *J. Neurotrauma* 12, 169–178 (1995).
 67. Chen, S., Pickard, J. D. & Harris, N. G. Time course of cellular pathology after controlled cortical impact injury. *Exp. Neurol.* 182, 87–102 (2003).
 68. Terpolilli, N. a, Kim, S.-W., Thal, S. C., Kuebler, W. M. & Plesnila, N. Inhaled nitric oxide reduces secondary brain damage after traumatic brain injury in mice. *J. Cereb. Blood Flow Metab.* 33, 311–8 (2013).
 69. Dixon, C. E. *et al.* One-year study of spatial memory performance, brain morphology, and cholinergic markers after moderate controlled cortical impact in rats. *J. Neurotrauma* 16, 109–122 (1999).
 70. Chen, S. F. *et al.* Salidroside Improves Behavioral and Histological Outcomes and Reduces Apoptosis via PI3K/Akt Signaling after Experimental Traumatic Brain Injury. *PLoS One* 7, (2012).
 71. Kaneko, Y. *et al.* Nestin Overexpression Precedes Caspase-3 Upregulation in Rats

- Exposed to Controlled Cortical Impact Traumatic Brain Injury. *Cell Med.* 4, 55–63 (2012).
72. Jiang, X., Huang, Y., Lin, W., Gao, D. & Fei, Z. Protective effects of hydrogen sulfide in a rat model of traumatic brain injury via activation of mitochondrial adenosine triphosphate-sensitive potassium channels and reduction of oxidative stress. *J. Surg. Res.* 184, (2013).
 73. Khan, M. *et al.* S-Nitrosoglutathione reduces oxidative injury and promotes mechanisms of neurorepair following traumatic brain injury in rats. *J. Neuroinflammation* 8, (2011).
 74. Miyamoto, K. *et al.* Therapeutic time window for edaravone treatment of traumatic brain injury in mice. *Biomed Res. Int.* 2013, (2013).
 75. Kochanek, P. M. *et al.* Severe Controlled Cortical Impact in Rats: Assessment of Cerebral Edema, Blood Flow, and Contusion Volume. *J. Neurotrauma* 12, 1015–1025 (1995).
 76. Dempsey, R. J., Bakaya, M. K. & Doğan, A. Attenuation of brain edema, blood-brain barrier breakdown, and injury volume by ifenprodil, a polyamine-site N-methyl-D-aspartate receptor antagonist, after experimental traumatic brain injury in rats. *Neurosurgery* 47, 399–406 (2000).
 77. Kochanek, P. M. *et al.* Cerebral blood flow at one year after controlled cortical impact in rats: Assessment by magnetic resonance imaging. *J. Neurotrauma* 19, 1029–1037 (2002).
 78. Mac Donald, C. L. *et al.* Detection of traumatic axonal injury with diffusion tensor imaging in a mouse model of traumatic brain injury. *Exp. Neurol.* 205, 116–31 (2007).
 79. Lighthall, J. W., Goshgarian, H. G. & Pinderski, C. R. Characterization of Axonal Injury Produced by Controlled Cortical Impact. *J. Neurotrauma* 7, 65–76 (1990).
 80. Sword, J., Masuda, T., Croom, D. & Kirov, S. A. Evolution of neuronal and astroglial disruption in the peri-contusional cortex of mice revealed by in vivo two-photon imaging. *Brain* 136, 1446–1461 (2013).
 81. Zhao, S., Gao, X., Dong, W. & Chen, J. The Role of 7,8-Dihydroxyflavone in Preventing Dendrite Degeneration in Cortex After Moderate Traumatic Brain Injury. *Mol. Neurobiol.* 53, 1884–1895 (2016).
 82. Jones, T. A. *et al.* Use-dependent dendritic regrowth is limited after unilateral controlled cortical impact to the forelimb sensorimotor cortex. *J. Neurotrauma* 29, 1455–1468 (2012).
 83. Winston, C. N. *et al.* Controlled Cortical Impact Results in an Extensive Loss of Dendritic Spines that Is Not Mediated by Injury-Induced Amyloid-Beta Accumulation. *J. Neurotrauma* 30, 1966–1972 (2013).
 84. Pijet, B., Stefaniuk, M. & Kaczmarek, L. MMP-9 contributes to dendritic spine remodeling following traumatic brain injury. *Neural Plast.* 2019, (2019).
 85. Gao, X., Deng, P., Xu, Z. C. & Chen, J. Moderate traumatic brain injury causes acute dendritic and synaptic degeneration in the hippocampal dentate gyrus. *PLoS One* 6, (2011).
 86. Haber, M. *et al.* Minocycline plus N-acetylcysteine synergize to modulate inflammation and prevent cognitive and memory deficits in a rat model of mild traumatic brain injury. *Exp. Neurol.* 249, 169–177 (2013).
 87. Fox, G. B., Fan, L., Levasseur, R. A. & Faden, A. I. Sustained sensory/motor and cognitive deficits with neuronal apoptosis following controlled cortical impact brain injury in the mouse. *J. Neurotrauma* 15, 599–614 (1998).
 88. Washington, P. M. *et al.* The effect of injury severity on behavior: A phenotypic study of cognitive and emotional deficits after mild, moderate, and severe controlled cortical impact injury in mice. *J. Neurotrauma* 29, 2283–2296 (2012).
 89. Bolkvadze, T. & Pitkänen, A. Development of post-traumatic epilepsy after controlled cortical impact and lateral fluid-percussion-induced brain injury in the mouse. *J. Neurotrauma* 29, 789–812 (2012).
 90. Tran, H. T., LaFerla, F. M., Holtzman, D. M. & Brody, D. L. Controlled cortical impact traumatic brain injury in 3xTg-AD mice causes acute intra-axonal amyloid- β accumulation and independently accelerates the development of tau abnormalities. *J. Neurosci.* 31, 9513–9525 (2011).
 91. Sheikhi, S., Saboory, E. & Farjah, G. H. Correlation of nerve fibers in corpus callosum and number of neurons in cerebral cortex: An innovative mathematical model. *Int. J.*

- Neurosci.* 128, 995–1002 (2018).
92. Knott, G. & Holtmaat, A. Dendritic spine plasticity—Current understanding from in vivo studies. *Brain Res. Rev.* 58, 282–289 (2008).
 93. Nimchinsky, E. A., Sabatini, B. L. & Svoboda, K. Structure and Function of Dendritic Spines. *Annu. Rev. Physiol.* 64, 313–353 (2002).
 94. Hering, H. & Sheng, M. Dendritic spines: structure, dynamics and regulation. *Nat. Rev. Neurosci.* 2, 880–888 (2001).
 95. Gipson, C. D. & Olive, M. F. Structural and functional plasticity of dendritic spines - root or result of behavior? *Genes. Brain. Behav.* 16, 101–117 (2017).
 96. Rochefort, N. L. & Konnerth, A. Dendritic spines: from structure to in vivo function. *EMBO Rep.* 13, 699–708 (2012).
 97. Berry, K. P. & Nedivi, E. Spine Dynamics: Are They All the Same? *Neuron* 96, 43–55 (2017).
 98. Grutzendler, J., Kasthuri, N. & Gan, W.-B. Long-term dendritic spine stability in the adult cortex. *Nature* 420, 812–816 (2002).
 99. Bhatt, D. H., Zhang, S. & Gan, W.-B. Dendritic Spine Dynamics. *Annu. Rev. Physiol.* 71, 261–282 (2009).
 100. Lu, J. & Zuo, Y. Clustered structural and functional plasticity of dendritic spines. *Brain Res. Bull.* 129, 18–22 (2017).
 101. Moyer, C. E. & Zuo, Y. Cortical dendritic spine development and plasticity: insights from in vivo imaging. *Curr. Opin. Neurobiol.* 53, 76–82 (2018).
 102. Tjia, M., Yu, X., Jammu, L. S., Lu, J. & Zuo, Y. Pyramidal Neurons in Different Cortical Layers Exhibit Distinct Dynamics and Plasticity of Apical Dendritic Spines. *Front. Neural Circuits* 11, 43 (2017).
 103. Chen, C.-C., Lu, J. & Zuo, Y. Spatiotemporal dynamics of dendritic spines in the living brain. *Front. Neuroanat.* 8, 28 (2014).
 104. Colgan, L. A. & Yasuda, R. Plasticity of dendritic spines: subcompartmentalization of signaling. *Annu. Rev. Physiol.* 76, 365–85 (2014).
 105. Segal, M. Dendritic spines, synaptic plasticity and neuronal survival: activity shapes dendritic spines to enhance neuronal viability. *Eur. J. Neurosci.* 31, 2178–2184 (2010).
 106. Yoshihara, Y., De Roo, M. & Muller, D. Dendritic spine formation and stabilization. *Curr. Opin. Neurobiol.* 19, 146–153 (2009).
 107. Lendvai, B., Stern, E. A., Chen, B. & Svoboda, K. Experience-dependent plasticity of dendritic spines in the developing rat barrel cortex in vivo. *Nature* 404, 876–881 (2000).
 108. Yang, G., Pan, F. & Gan, W. B. Stably maintained dendritic spines are associated with lifelong memories. *Nature* 462, 920–924 (2009).
 109. Zuo, Y., Yang, G., Kwon, E. & Gan, W. B. Long-term sensory deprivation prevents dendritic spine loss in primary somatosensory cortex. *Nature* 436, 261–265 (2005).
 110. Ozcan, A. S. & Ozcan, M. S. Population Dynamics and Long-Term Trajectory of Dendritic Spines. *Front. Synaptic Neurosci.* 10, (2018).
 111. Halpain, S., Spencer, K. & Graber, S. Dynamics and pathology of dendritic spines. *Progress in Brain Research* 147, 29–37 (2005).
 112. Yuste, R., Majewska, A. & Holthoff, K. From form to function: Calcium compartmentalization in dendritic spines. *Nature Neuroscience* 3, 653–659 (2000).
 113. Adrian, M. *et al.* Barriers in the brain: Resolving dendritic spine morphology and compartmentalization. *Frontiers in Neuroanatomy* 8, (2014).
 114. Villa, K. L. *et al.* Inhibitory Synapses Are Repeatedly Assembled and Removed at Persistent Sites In Vivo. *Neuron* 89, 756–769 (2016).
 115. Chen, J. L. *et al.* Clustered Dynamics of Inhibitory Synapses and Dendritic Spines in the Adult Neocortex. *Neuron* 74, 361–373 (2012).
 116. Chiu, C. Q. *et al.* Compartmentalization of GABAergic inhibition by dendritic spines. *Science (80-.)*. 340, 759–762 (2013).
 117. Holtmaat, A. J. G. D. *et al.* Transient and Persistent Dendritic Spines in the Neocortex In Vivo. *Neuron* 45, 279–291 (2005).
 118. Zuo, Y. *et al.* Development of long-term dendritic spine stability in diverse regions of cerebral cortex. *Neuron* 46, 181–189 (2005).
 119. Gan, W. B., Kasthuri, N. & Yang, G. Spine Plasticity. in *Encyclopedia of Neuroscience* 321–327 (Elsevier Ltd, 2009). doi:10.1016/B978-008045046-9.00362-4

120. Zuo, Y., Lin, A., Chang, P. & Gan, W.-B. Development of long-term dendritic spine stability in diverse regions of cerebral cortex. *Neuron* 46, 181–9 (2005).
121. Petanjek, Z. *et al.* Extraordinary neoteny of synaptic spines in the human prefrontal cortex. *Proc. Natl. Acad. Sci. U. S. A.* 108, 13281–13286 (2011).
122. Rakic, P., Bourgeois, J. P., Eckenhoff, M. F., Zecevic, N. & Goldman-Rakic, P. S. Concurrent overproduction of synapses in diverse regions of the primate cerebral cortex. *Science (80-.)*. 232, 232–235 (1986).
123. Lendvai, B., Stern, E. A., Chen, B. & Svoboda, K. Experience-dependent plasticity of dendritic spines in the developing rat barrel cortex in vivo. *Nature* 404, 876–881 (2000).
124. Jung, C. K. E. & Herms, J. Structural dynamics of dendritic spines are influenced by an environmental enrichment: An in vivo imaging study. *Cereb. Cortex* 24, 377–384 (2014).
125. Wilbrecht, L., Holtmaat, A., Wright, N., Fox, K. & Svoboda, K. Structural plasticity underlies experience-dependent functional plasticity of cortical circuits. *J. Neurosci.* 30, 4927–4932 (2010).
126. Keck, T. *et al.* Massive restructuring of neuronal circuits during functional reorganization of adult visual cortex. *Nat. Neurosci.* 11, 1162–1167 (2008).
127. Cruz-Martín, A., Crespo, M. & Portera-Cailliau, C. Delayed stabilization of dendritic spines in fragile X mice. *J. Neurosci.* 30, 7793–7803 (2010).
128. Padmashri, R., Reiner, B. C., Suresh, A., Spartz, E. & Dunaevsky, A. Altered structural and functional synaptic plasticity with motor skill learning in a mouse model of fragile X syndrome. *J. Neurosci.* 33, 19715–23 (2013).
129. Pan, F., Aldridge, G. M., Greenough, W. T. & Gan, W. B. Dendritic spine instability and insensitivity to modulation by sensory experience in a mouse model of fragile X syndrome. *Proc. Natl. Acad. Sci. U. S. A.* 107, 17768–17773 (2010).
130. Penzes, P., Cahill, M. E., Jones, K. A., Vanleeuwen, J. E. & Woolfrey, K. M. Dendritic spine pathology in neuropsychiatric disorders. *Nature Neuroscience* 14, 285–293 (2011).
131. Hutsler, J. J. & Zhang, H. Increased dendritic spine densities on cortical projection neurons in autism spectrum disorders. *Brain Res.* 1309, 83–94 (2010).
132. TAKASHIMA, S., IIDA, K., MITO, T. & ARIMA, M. Dendritic and histochemical development and ageing in patients with Down’s syndrome. *J. Intellect. Disabil. Res.* 38, 265–273 (2008).
133. Cramer, N. & Galdzicki, Z. From abnormal hippocampal synaptic plasticity in down syndrome mouse models to cognitive disability in down syndrome. *Neural Plasticity* 2012, (2012).
134. Sweet, R. A., Henteleff, R. A., Zhang, W., Sampson, A. R. & Lewis, D. A. Reduced dendritic spine density in auditory cortex of subjects with schizophrenia. *Neuropsychopharmacology* 34, 374–389 (2009).
135. Kvajo, M. *et al.* A mutation in mouse *Disc1* that models a schizophrenia risk allele leads to specific alterations in neuronal architecture and cognition. *Proc. Natl. Acad. Sci. U. S. A.* 105, 7076–7081 (2008).
136. Murmu, R. P., Li, W., Holtmaat, A. & Li, J. Y. Dendritic spine instability leads to progressive neocortical spine loss in a mouse model of huntington’s disease. *J. Neurosci.* 33, 12997–13009 (2013).
137. Liebscher, S. *et al.* Chronic γ -secretase inhibition reduces amyloid plaque-associated instability of pre- and postsynaptic structures. *Mol. Psychiatry* 19, 937–46 (2014).
138. Merino-Serrais, P., Knafo, S., Alonso-Nanclares, L., Fernaud-Espinosa, I. & Defelipe, J. Layer-specific alterations to CA1 dendritic spines in a mouse model of Alzheimer’s disease. *Hippocampus* 21, 1037–1044 (2011).
139. Spires, T. L. *et al.* Dendritic spine abnormalities in amyloid precursor protein transgenic mice demonstrated by gene transfer and intravital multiphoton microscopy. *J. Neurosci.* 25, 7278–87 (2005).
140. Winston, C. N. *et al.* Controlled cortical impact results in an extensive loss of dendritic spines that is not mediated by injury-induced amyloid-beta accumulation. *J. Neurotrauma* 30, 1966–1972 (2013).
141. Brown, C. E., Li, P., Boyd, J. D., Delaney, K. R. & Murphy, T. H. Extensive turnover of dendritic spines and vascular remodeling in cortical tissues recovering from stroke. *J. Neurosci.* 27, 4101–9 (2007).

142. Takatsuru, Y. *et al.* Neuronal circuit remodeling in the contralateral cortical hemisphere during functional recovery from cerebral infarction. *J. Neurosci.* 29, 10081–10086 (2009).
143. Xiong, Y., Mahmood, A. & Chopp, M. Remodeling dendritic spines for treatment of traumatic brain injury. *Neural Regeneration Research* 14, 1477–1480 (2019).
144. Fame, R. M., MacDonald, J. L. & Macklis, J. D. Development, specification, and diversity of callosal projection neurons. *Trends Neurosci.* 34, 41–50 (2011).
145. Ramos, R. L., Tam, D. M. & Brumberg, J. C. Physiology and morphology of callosal projection neurons in mouse. *Neuroscience* 153, 654–63 (2008).
146. Restani, L. & Caleo, M. Reorganization of visual callosal connections following alterations of retinal input and brain damage. *Frontiers in Systems Neuroscience* 10, (2016).
147. Peters, A., Payne, B. R. & Josephson, K. Transcallosal non-pyramidal cell projections from visual cortex in the cat. *J. Comp. Neurol.* 302, 124–42 (1990).
148. Gonchar, Y. A., Johnson, P. B. & Weinberg, R. J. GABA-immunopositive neurons in rat neocortex with contralateral projections to S-I. *Brain Res.* 697, 27–34 (1995).
149. Weber, R. *et al.* Early prediction of functional recovery after experimental stroke: Functional magnetic resonance imaging, electrophysiology, and behavioral testing in rats. *J. Neurosci.* 28, 1022–1029 (2008).
150. Zurita, H., Feyen, P. L. C. & Apicella, A. J. Layer 5 Callosal Parvalbumin-Expressing Neurons: A Distinct Functional Group of GABAergic Neurons. *Front. Cell. Neurosci.* 12, (2018).
151. Aboitiz, F. & Montiel, J. One hundred million years of interhemispheric communication: the history of the corpus callosum. *Brazilian J. Med. Biol. Res. = Rev. Bras. Pesqui. médicas e biológicas / Soc. Bras. Biofísica ... [et al.]* 36, 409–20 (2003).
152. Bloom, J. S. & Hynd, G. W. The Role of the Corpus Callosum in Interhemispheric Transfer of Information: Excitation or Inhibition? *Neuropsychol. Rev.* 15, 59–71 (2005).
153. Zhou, J. *et al.* Axon position within the corpus callosum determines contralateral cortical projection. *Proc. Natl. Acad. Sci.* 110, E2714–23 (2013).
154. Nowicka, A. & Tacikowski, P. Transcallosal transfer of information and functional asymmetry of the human brain. *Laterality Asymmetries Body, Brain Cogn.* 16, 35–74 (2011).
155. Owen R. On the structure of the brain in marsupial animals. *Philos. Trans. R. Soc. London* 127, 87–96 (1837).
156. van der Knaap, L. J. & van der Ham, I. J. M. How does the corpus callosum mediate interhemispheric transfer? A review. *Behav. Brain Res.* 223, 211–221 (2011).
157. Suárez, R., Gobijs, I. & Richards, L. J. Evolution and development of interhemispheric connections in the vertebrate forebrain. *Front. Hum. Neurosci.* 8, 497 (2014).
158. Tagawa, Y. & Hirano, T. Activity-dependent callosal axon projections in neonatal mouse cerebral cortex. *Neural Plasticity* 2012, (2012).
159. Fenlon, L. R., Suárez, R. & Richards, L. J. The anatomy, organisation and development of contralateral callosal projections of the mouse somatosensory cortex. *Brain Neurosci. Adv.* 1, 239821281769488 (2017).
160. Walterfang, M. *et al.* Corpus callosum size and shape in first-episode affective and schizophrenia-spectrum psychosis. *Psychiatry Res.* 173, 77–82 (2009).
161. Bersani, G. *et al.* Corpus callosum abnormalities and potential age effect in men with schizophrenia: an MRI comparative study. *Psychiatry Res.* 183, 119–25 (2010).
162. Evangelou, N. *et al.* Regional axonal loss in the corpus callosum correlates with cerebral white matter lesion volume and distribution in multiple sclerosis. *Brain* 123 (Pt 9), 1845–9 (2000).
163. Manson, S. C., Palace, J., Frank, J. A. & Matthews, P. M. Loss of interhemispheric inhibition in patients with multiple sclerosis is related to corpus callosum atrophy. *Exp. Brain Res.* 174, 728–733 (2006).
164. Granberg, T. *et al.* MRI-Defined Corpus Callosal Atrophy in Multiple Sclerosis: A Comparison of Volumetric Measurements, Corpus Callosum Area and Index. *J. Neuroimaging* 25, 996–1001 (2015).
165. Yamauchi, H. *et al.* Comparison of the pattern of atrophy of the corpus callosum in frontotemporal dementia, progressive supranuclear palsy, and Alzheimer's disease. *J.*

- Neurol. Neurosurg. Psychiatry* 69, 623–629 (2000).
166. Meguro, K. *et al.* Corpus callosum atrophy, white matter lesions, and frontal executive dysfunction in normal aging and Alzheimer's disease. A community-based study: The Tajiri Project. *Int. Psychogeriatrics* 15, 9–25 (2003).
 167. Bachman, A. H., Lee, S. H., Sidtis, J. J. & Ardekani, B. A. Corpus callosum shape and size changes in early Alzheimer's disease: a longitudinal MRI study using the OASIS brain database. *J. Alzheimers. Dis.* 39, 71–8 (2014).
 168. Vidal, C. N. *et al.* Mapping corpus callosum deficits in autism: an index of aberrant cortical connectivity. *Biol. Psychiatry* 60, 218–25 (2006).
 169. He, Q., Duan, Y., Karsch, K. & Miles, J. Detecting corpus callosum abnormalities in autism based on anatomical landmarks. *Psychiatry Res.* 183, 126–32 (2010).
 170. Egaas, B., Courchesne, E. & Saitoh, O. Reduced Size of Corpus Callosum in Autism. *Arch. Neurol.* 52, 794–801 (1995).
 171. Hutchinson, A. D., Mathias, J. L. & Banich, M. T. Corpus Callosum Morphology in Children and Adolescents With Attention Deficit Hyperactivity Disorder: A Meta-Analytic Review. *Neuropsychology* 22, 341–349 (2008).
 172. Cao, Q. *et al.* The macrostructural and microstructural abnormalities of corpus callosum in children with attention deficit/hyperactivity disorder: a combined morphometric and diffusion tensor MRI study. *Brain Res.* 1310, 172–80 (2010).
 173. Buchmann, J. *et al.* Disturbed transcallosally mediated motor inhibition in children with attention deficit hyperactivity disorder (ADHD). *Clin. Neurophysiol.* 114, 2036–2042 (2003).
 174. Fenlon, L. R. & Richards, L. J. Contralateral targeting of the corpus callosum in normal and pathological brain function. *Trends Neurosci.* 38, 264–272 (2015).
 175. Sun, Y. F., Lee, J. S. & Kirby, R. Brain imaging findings in dyslexia. *Pediatrics and Neonatology* 51, 89–96 (2010).
 176. Rutgers, D. R. *et al.* Diffusion tensor imaging characteristics of the corpus callosum in mild, moderate, and severe traumatic brain injury. *Am. J. Neuroradiol.* 29, 1730–1735 (2008).
 177. Babikian, T. *et al.* Metabolic levels in the corpus callosum and their structural and behavioral correlates after moderate to severe pediatric TBI. *J. Neurotrauma* 27, 473–481 (2010).
 178. Chovsepian, A., Empl, L., Correa, D. & Bareyre, F. M. Heterotopic transcallosal projections are present throughout the mouse cortex. *Front. Cell. Neurosci.* 11, 36 (2017).
 179. Evans, T. A., Bury, L. A., Huang, A. Y. & Sabo, S. L. Spatio-temporal dynamics of neocortical presynaptic terminal development using multi-photon imaging of the corpus callosum in vivo. *Sci. Rep.* 9, (2019).
 180. De León Reyes, N. S. *et al.* Transient callosal projections of L4 neurons are eliminated for the acquisition of local connectivity. *Nat. Commun.* 10, (2019).
 181. Shatz, C. J. Anatomy of interhemispheric connections in the visual system of Boston Siamese and ordinary cats. *J. Comp. Neurol.* 173, 497–518 (1977).
 182. Wise, S. P. & Jones, E. G. The organization and postnatal development of the commissural projection of the rat somatic sensory cortex. *J. Comp. Neurol.* 168, 313–343 (1976).
 183. Oudega, M. & Perez, M. A. Corticospinal reorganization after spinal cord injury. *Journal of Physiology* 590, 3647–3663 (2012).
 184. Jang, S. H. The corticospinal tract from the viewpoint of brain rehabilitation. *Journal of Rehabilitation Medicine* 46, 193–199 (2014).
 185. Ueno, M. *et al.* Corticospinal Circuits from the Sensory and Motor Cortices Differentially Regulate Skilled Movements through Distinct Spinal Interneurons. *Cell Rep.* 23, 1286–1300.e7 (2018).
 186. Anderson, C. T., Sheets, P. L., Kiritani, T. & Shepherd, G. M. G. Sublayer-specific microcircuits of corticospinal and corticostriatal neurons in motor cortex. *Nat. Neurosci.* 13, 739–744 (2010).
 187. Serradj, N., Agger, S. F. & Hollis, E. R. Corticospinal circuit plasticity in motor rehabilitation from spinal cord injury. *Neurosci. Lett.* 652, 94–104 (2017).
 188. Murphy, T. H. & Corbett, D. Plasticity during stroke recovery: from synapse to behaviour. *Nat. Rev. Neurosci.* 10, 861–872 (2009).
 189. Dodd, K. C., Nair, V. A. & Prabhakaran, V. Role of the contralesional vs. Ipsilesional

- hemisphere in stroke recovery. *Frontiers in Human Neuroscience* 11, (2017).
190. Mostany, R. *et al.* Local hemodynamics dictate long-term dendritic plasticity in peri-infarct cortex. *J. Neurosci.* 30, 14116–14126 (2010).
 191. Brown, C. E., Aminoltejadi, K., Erb, H., Winship, I. R. & Murphy, T. H. In vivo voltage-sensitive dye imaging in adult mice reveals that somatosensory maps lost to stroke are replaced over weeks by new structural and functional circuits with prolonged modes of activation within both the peri-infarct zone and distant sites. *J. Neurosci.* 29, 1719–34 (2009).
 192. Zhang, S., Boyd, J., Delaney, K. & Murphy, T. H. Rapid reversible changes in dendritic spine structure in vivo gated by the degree of ischemia. *J. Neurosci.* 25, 5333–5338 (2005).
 193. Murphy, T. H., Li, P., Betts, K. & Liu, R. Two-photon imaging of stroke onset in vivo reveals that NMDA-receptor independent ischemic depolarization is the major cause of rapid reversible damage to dendrites and spines. *J. Neurosci.* 28, 1756–1772 (2008).
 194. Cramer, S. C. Repairing the human brain after stroke: I. Mechanisms of spontaneous recovery. *Ann. Neurol.* 63, 272–287 (2008).
 195. Carmichael, S. T. *et al.* Growth-associated gene expression after stroke: Evidence for a growth-promoting region in peri-infarct cortex. *Exp. Neurol.* 193, 291–311 (2005).
 196. Oyesiku, N. M. *et al.* Regional changes in the expression of neurotrophic factors and their receptors following acute traumatic brain injury in the adult rat brain. *Brain Res.* 833, 161–72 (1999).
 197. Kobori, N., Clifton, G. L. & Dash, P. Altered expression of novel genes in the cerebral cortex following experimental brain injury. *Brain Res. Mol. Brain Res.* 104, 148–158 (2002).
 198. Benowitz, L. I. & Carmichael, S. T. Promoting axonal rewiring to improve outcome after stroke. *Neurobiol. Dis.* 37, 259–266 (2010).
 199. Emery, D. L. *et al.* Bilateral growth-related protein expression suggests a transient increase in regenerative potential following brain trauma. *J. Comp. Neurol.* 424, 521–31 (2000).
 200. Uryu, K., MacKenzie, L. & Chesselet, M. F. Ultrastructural evidence for differential axonal sprouting in the striatum after thermocoagulatory and aspiration lesions of the cerebral cortex in adult rats. *Neuroscience* 105, 307–16 (2001).
 201. Harris, N. G., Chen, S. F. & Pickard, J. D. Cortical reorganization after experimental traumatic brain injury: A functional autoradiography study. *J. Neurotrauma* 30, 1137–1146 (2013).
 202. Hulsebosch, C. E., DeWitt, D. S., Jenkins, L. W. & Prough, D. S. Traumatic brain injury in rats results in increased expression of Gap-43 that correlates with behavioral recovery. *Neurosci. Lett.* 255, 83–6 (1998).
 203. Harris, N. G., Mironova, Y. A., Hovda, D. A. & Sutton, R. L. Pericontusion axon sprouting is spatially and temporally consistent with a growth-permissive environment after traumatic brain injury. *J. Neuropathol. Exp. Neurol.* 69, 139–154 (2010).
 204. Johnstone, V. P. A., Yan, E. B., Alwis, D. S. & Rajan, R. Cortical Hypoexcitation Defines Neuronal Responses in the Immediate Aftermath of Traumatic Brain Injury. *PLoS One* 8, e63454 (2013).
 205. Ding, M. C., Wang, Q., Lo, E. H. & Stanley, G. B. Cortical excitation and inhibition following focal traumatic brain injury. *J. Neurosci.* 31, 14085–14094 (2011).
 206. Allitt, B. J., Iva, P., Yan, E. B. & Rajan, R. Hypo-excitation across all cortical laminae defines intermediate stages of cortical neuronal dysfunction in diffuse traumatic brain injury. *Neuroscience* 334, 290–308 (2016).
 207. Johnstone, V. P. A., Shultz, S. R., Yan, E. B., O'Brien, T. J. & Rajan, R. The acute phase of mild traumatic brain injury is characterized by a distance-dependent neuronal hypoactivity. *J. Neurotrauma* 31, 1881–1895 (2014).
 208. Binkofski, F. & Seitz, R. J. Modulation of the BOLD-response in early recovery from sensorimotor stroke. *Neurology* 63, 1223–1229 (2004).
 209. Calautti, C., Leroy, F., Guincestre, J. Y. & Baron, J. C. Dynamics of motor network overactivation after striatocapsular stroke: A longitudinal PET study using a fixed-performance paradigm. *Stroke* 32, 2534–2542 (2001).
 210. Fridman, E. A. Reorganization of the human ipsilesional premotor cortex after stroke.

- Brain* 127, 747–758 (2004).
211. Rossini, P. M., Calautti, C., Pauri, F. & Baron, J.-C. Post-stroke plastic reorganisation in the adult brain. *Lancet. Neurol.* 2, 493–502 (2003).
 212. Pineiro, R., Pendlebury, S., Johansen-Berg, H. & Matthews, P. M. Functional MRI detects posterior shifts in primary sensorimotor cortex activation after stroke: Evidence of local adaptive reorganization? *Stroke* 32, 1134–1139 (2001).
 213. Winship, I. R. & Murphy, T. H. In Vivo Calcium Imaging Reveals Functional Rewiring of Single Somatosensory Neurons after Stroke. *J. Neurosci.* 28, 6592–6606 (2008).
 214. Brown, C. E., Wong, C. & Murphy, T. H. Rapid morphologic plasticity of peri-infarct dendritic spines after focal ischemic stroke. *Stroke* 39, 1286–1291 (2008).
 215. Duering, M. *et al.* Incident subcortical infarcts induce focal thinning in connected cortical regions. *Neurology* 79, 2025–2028 (2012).
 216. Takatsuru, Y., Nabekura, J. & Koibuchi, N. Activity of the layer II/III neurons in the somatosensory cortex (SSC) plays a critical role on functional recovery after focal stroke in the contralateral SSC. *Neurosci. Lett.* 543, 168–171 (2013).
 217. Abo, M., Chen, Z., Lai, L. J., Reese, T. & Bjelke, B. Functional recovery after brain lesion - Contralateral neuromodulation: An fMRI study. *Neuroreport* 12, 1543–1547 (2001).
 218. Schaechter, J. D. & Perdue, K. L. Enhanced cortical activation in the contralesional hemisphere of chronic stroke patients in response to motor skill challenge. *Cereb. Cortex* 18, 638–647 (2008).
 219. Reinecke, S., Dinse, H. R., Reinke, H. & Witte, O. W. Induction of bilateral plasticity in sensory cortical maps by small unilateral cortical infarcts in rats. *Eur. J. Neurosci.* 17, 623–627 (2003).
 220. Pruitt, D. T. *et al.* Traumatic Brain Injury Occludes Training-Dependent Cortical Reorganization in the Contralesional Hemisphere. *J. Neurotrauma* 34, 2495–2503 (2017).
 221. Axelson, H. W. *et al.* Plasticity of the contralateral motor cortex following focal traumatic brain injury in the rat. *Restor. Neurol. Neurosci.* 31, 73–85 (2013).
 222. Jones, T. A., Kleim, J. A. & Greenough, W. T. Synaptogenesis and dendritic growth in the cortex opposite unilateral sensorimotor cortex damage in adult rats: a quantitative electron microscopic examination. *Brain Res.* 733, 142–148 (1996).
 223. Luke, L. M., Allred, R. P. & Jones, T. A. Unilateral ischemic sensorimotor cortical damage induces contralesional synaptogenesis and enhances skilled reaching with the ipsilateral forelimb in adult male rats. *Synapse* 54, 187–199 (2004).
 224. Li, N. *et al.* Optogenetic-guided cortical plasticity after nerve injury. *Proc. Natl. Acad. Sci. U. S. A.* 108, 8838–8843 (2011).
 225. Allred, R. P., Cappellini, C. H. & Jones, T. A. The ‘Good’ Limb Makes the ‘Bad’ Limb Worse: Experience-Dependent Interhemispheric Disruption of Functional Outcome After Cortical Infarcts in Rats. *Behav. Neurosci.* 124, 124–132 (2010).
 226. Han, Y., Li, N., Zeiler, S. R. & Pelled, G. Peripheral nerve injury induces immediate increases in layer v neuronal activity. *Neurorehabil. Neural Repair* 27, 664–672 (2013).
 227. Le Priault, F., Thal, S. C., Engelhard, K., Imbrosci, B. & Mittmann, T. Acute Cortical Transhemispheric Diaschisis after Unilateral Traumatic Brain Injury. *J. Neurotrauma* 34, 1097–1110 (2017).
 228. Imbrosci, B. & Mittmann, T. Functional consequences of the disturbances in the GABA-mediated inhibition induced by injuries in the cerebral cortex. *Neural Plasticity* 2011, (2011).
 229. Verley, D. R. *et al.* Remote Changes in Cortical Excitability after Experimental Traumatic Brain Injury and Functional Reorganization. *J. Neurotrauma* 35, 2448–2461 (2018).
 230. Maggiolini, E., Viaro, R. & Franchi, G. Suppression of activity in the forelimb motor cortex temporarily enlarges forelimb representation in the homotopic cortex in adult rats. *Eur. J. Neurosci.* 27, 2733–2746 (2008).
 231. Carron, S. F., Alwis, D. S. & Rajan, R. Traumatic brain injury and neuronal functionality changes in sensory cortex. *Frontiers in Systems Neuroscience* 10, (2016).
 232. Touvykine, B. *et al.* The effect of lesion size on the organization of the ipsilesional and contralesional motor cortex. *Neurorehabil. Neural Repair* 30, 280–292 (2016).
 233. Kim, S. Y. & Jones, T. A. Lesion size-dependent synaptic and astrocytic responses in cortex contralateral to infarcts in middle-aged rats. *Synapse* 64, 659–671 (2010).

234. Grzybowski, A. & Pietrzak, K. Maria Goeppert-Mayer (1906-1972): two-photon effect on dermatology. *Clin. Dermatol.* 31, 221–225 (2013).
235. So, P. T. Two-photon Fluorescence Light Microscopy. in *eLS* 1–5 (John Wiley & Sons, Ltd, 2001). doi:10.1038/npg.els.0002991
236. Sheppard, C. J. R. & Kompfner, R. Resonant scanning optical microscope. *Appl. Opt.* 17, 2879 (1978).
237. Denk, W., Strickler, J. H. & Webb, W. W. Two-photon laser scanning fluorescence microscopy. *Science* (80-.). 248, 73–76 (1990).
238. Feng, G. *et al.* Imaging neuronal subsets in transgenic mice expressing multiple spectral variants of GFP. *Neuron* 28, 41–51 (2000).
239. Zuo, Y., Yu, X., Tennant, K. & Jones, T. In Vivo Imaging of Synapse Plasticity in the Mouse Motor Cortex. in 45–57 (2013). doi:10.1007/978-1-62703-411-1_4
240. Sadakane, O. *et al.* In vivo two-photon imaging of dendritic spines in marmoset neocortex. *eNeuro* 2, 1–10 (2015).
241. Holtmaat, A. & Svoboda, K. Experience-dependent structural synaptic plasticity in the mammalian brain. *Nat. Rev. Neurosci.* 10, 647–658 (2009).
242. Hofer, S. B., Mrcic-Flogel, T. D., Bonhoeffer, T. & Hübener, M. Experience leaves a lasting structural trace in cortical circuits. *Nature* 457, 313–317 (2009).
243. Fu, M., Yu, X., Lu, J. & Zuo, Y. Repetitive motor learning induces coordinated formation of clustered dendritic spines in vivo. *Nature* 483, 92–96 (2012).
244. Della Sala, G. *et al.* Dendritic Spine Instability in a Mouse Model of CDKL5 Disorder Is Rescued by Insulin-like Growth Factor 1. *Biol. Psychiatry* 1–10 (2014). doi:10.1016/j.biopsych.2015.08.028
245. Tsai, J., Grutzendler, J., Duff, K. & Gan, W.-B. Fibrillar amyloid deposition leads to local synaptic abnormalities and breakage of neuronal branches. *Nat. Neurosci.* 7, 1181–3 (2004).
246. Crowe, S. E. & Ellis-Davies, G. C. R. Longitudinal in vivo two-photon fluorescence imaging. *J. Comp. Neurol.* 522, 1708–1727 (2014).
247. Dorand, R. D., Barkauskas, D. S., Evans, T. A., Petrosiute, A. & Huang, A. Y. Comparison of intravital thinned skull and cranial window approaches to study CNS immunobiology in the mouse cortex. *IntraVital* 3, e29728 (2014).
248. Holtmaat, A. *et al.* Imaging Neocortical Neurons through a Chronic Cranial Window. *Cold Spring Harb. Protoc.* 2012, pdb.prot069617-pdb.prot069617 (2012).
249. Holtmaat, A. *et al.* Long-term, high-resolution imaging in the mouse neocortex through a chronic cranial window. *Nat. Protoc.* 4, 1128–44 (2009).
250. Lichtman, J. W. & Conchello, J. A. Fluorescence microscopy. *Nature Methods* 2, 910–919 (2005).
251. Helmchen, F. & Denk, W. Deep tissue two-photon microscopy. *Nature* 2, 932–940 (2005).
252. Wilt, B. A. *et al.* Advances in Light Microscopy for Neuroscience. *Annu. Rev. Neurosci.* 32, 435–506 (2009).
253. Svoboda, K. & Yasuda, R. Principles of Two-Photon Excitation Microscopy and Its Applications to Neuroscience. *Neuron* 50, 823–839 (2006).
254. Mostany, R., Miquelajauregui, A., Shtrahman, M. & Portera-Cailliau, C. Two-photon excitation microscopy and its applications in neuroscience. *Methods Mol. Biol.* 1251, 25–42 (2014).
255. Mittmann, W. *et al.* Two-photon calcium imaging of evoked activity from L5 somatosensory neurons in vivo. *Nat. Neurosci.* 14, 1089–1093 (2011).
256. Köbbert, C. *et al.* Current concepts in neuroanatomical tracing. *Prog. Neurobiol.* 62, 327–351 (2000).
257. Lanciego, J. L. & Wouterlood, F. G. A half century of experimental neuroanatomical tracing. *Journal of Chemical Neuroanatomy* 42, 157–183 (2011).
258. Schofield, B. R. Retrograde axonal tracing with fluorescent markers. *Curr. Protoc. Neurosci.* 1–24 (2008). doi:10.1002/0471142301.ns0117s43
259. Schofield, B. R., Schofield, R. M., Sorensen, K. A. & Motts, S. D. On the use of retrograde tracers for identification of axon collaterals with multiple fluorescent retrograde tracers. *Neuroscience* 146, 773–783 (2007).
260. Naumann, T., Härtig, W. & Frotscher, M. Retrograde tracing with Fluoro-Gold: Different methods of tracer detection at the ultrastructural level and neurodegenerative changes of back-filled neurons in long-term studies. *J. Neurosci.*

- Methods* 103, 11–21 (2000).
261. Schmued, L. C. & Fallon, J. H. Fluoro-Gold: a new fluorescent retrograde axonal tracer with numerous unique properties. *Brain Res.* 377, 147–54 (1986).
 262. Yao, F. *et al.* Did you choose appropriate tracer for retrograde tracing of retinal ganglion cells. the differences between cholera toxin subunit B and Fluorogold. *PLoS One* 13, (2018).
 263. Vercelli, A., Repici, M., Garbossa, D. & Grimaldi, A. Recent techniques for tracing pathways in the central nervous system of developing and adult mammals. *Brain Res. Bull.* 51, 11–28 (2000).
 264. Veenman, C. L. L., Reiner, A. & Honig, M. G. Biotinylated dextran amine as an anterograde tracer for single- and double-labeling studies. *J. Neurosci. Methods* 41, 239–254 (1992).
 265. Reiner, A. *et al.* Pathway tracing using biotinylated dextran amines. *J. Neurosci. Methods* 103, 23–37 (2000).
 266. Aschauer, D. F., Kreuz, S. & Rumpel, S. Analysis of Transduction Efficiency, Tropism and Axonal Transport of AAV Serotypes 1, 2, 5, 6, 8 and 9 in the Mouse Brain. *PLoS One* 8, e76310 (2013).
 267. Tervo, D. G. R. *et al.* A Designer AAV Variant Permits Efficient Retrograde Access to Projection Neurons. *Neuron* 92, 372–382 (2016).
 268. Betley, J. N. & Sternson, S. M. Adeno-associated viral vectors for mapping, monitoring, and manipulating neural circuits. *Hum. Gene Ther.* 22, 669–677 (2011).
 269. Hollis, E. R., Kadoya, K., Hirsch, M., Samulski, R. J. & Tuszynski, M. H. Efficient retrograde neuronal transduction utilizing self-complementary AAV1. *Mol. Ther.* 16, 296–301 (2008).
 270. Rotherme, M., Brunert, D., Zabawa, C., Diaz-Quesada, M. & Wachowiak, M. Transgene expression in target-defined neuron populations mediated by retrograde infection with adeno-associated viral vectors. *J. Neurosci.* 33, 15195–15206 (2013).
 271. Ginger, M., Haberl, M., Conzelmann, K.-K., Schwarz, M. K. & Frick, A. Revealing the secrets of neuronal circuits with recombinant rabies virus technology. *Front. Neural Circuits* 7, 2 (2013).
 272. Ugolini, G. *Rabies Virus as a Transneuronal Tracer of Neuronal Connections. Advances in Virus Research* 79, (2011).
 273. Osakada, F. *et al.* New rabies virus variants for monitoring and manipulating activity and gene expression in defined neural circuits. *Neuron* 71, 617–631 (2011).
 274. Callaway, E. M. Transneuronal circuit tracing with neurotropic viruses. *Curr. Opin. Neurobiol.* 18, 617–623 (2008).
 275. Callaway, E. M. & Luo, L. Monosynaptic Circuit Tracing with Glycoprotein-Deleted Rabies Viruses. *J. Neurosci.* 35, 8979–85 (2015).
 276. Wickersham, I. R. *et al.* Monosynaptic Restriction of Transsynaptic Tracing from Single, Genetically Targeted Neurons. *Neuron* 53, 639–647 (2007).
 277. Wickersham, I. R., Finke, S., Conzelmann, K.-K. & Callaway, E. M. Retrograde neuronal tracing with a deletion-mutant rabies virus. *Nat. Methods* 4, 47–49 (2007).
 278. Kim, E. J., Jacobs, M. W., Ito-Cole, T. & Callaway, E. M. Improved Monosynaptic Neural Circuit Tracing Using Engineered Rabies Virus Glycoproteins. *Cell Rep.* 15, 692–699 (2016).
 279. Luo, P. *et al.* Whole Brain Mapping of Long-Range Direct Input to Glutamatergic and GABAergic Neurons in Motor Cortex. *Front. Neuroanat.* 13, (2019).
 280. Hafner, G. *et al.* Mapping Brain-Wide Afferent Inputs of Parvalbumin-Expressing GABAergic Neurons in Barrel Cortex Reveals Local and Long-Range Circuit Motifs. *Cell Rep.* 28, 3450–3461.e8 (2019).
 281. Ährlund-Richter, S. *et al.* A whole-brain atlas of monosynaptic input targeting four different cell types in the medial prefrontal cortex of the mouse. *Nat. Neurosci.* 22, 657–668 (2019).
 282. Watabe-Uchida, M., Zhu, L., Ogawa, S. K., Vamanrao, A. & Uchida, N. Whole-Brain Mapping of Direct Inputs to Midbrain Dopamine Neurons. *Neuron* 74, 858–873 (2012).
 283. Bareyre, F. M., Haudenschild, B. & Schwab, M. E. Long-Lasting Sprouting and Gene Expression Changes Induced by the Monoclonal Antibody IN-1 in the Adult Spinal Cord. *J. Neurosci.* 22, (2002).
 284. Bareyre, F. M. *et al.* The injured spinal cord spontaneously forms a new intraspinal

- circuit in adult rats. *Nat. Neurosci.* 7, 269–77 (2004).
285. Jacobi, A. *et al.* FGF22 signaling regulates synapse formation during post-injury remodeling of the spinal cord. *EMBO J.* 34, 1231–1244 (2015).
 286. Jacobi, A., Schmalz, A. & Bareyre, F. M. Abundant expression of guidance and synaptogenic molecules in the injured spinal cord. *PLoS One* 9, (2014).
 287. Jacobi, A. *et al.* FGF22 signaling regulates synapse formation during post-injury remodeling of the spinal cord. *EMBO J.* 34, 1231–1243 (2015).
 288. Yu, F. *et al.* Posttrauma cotreatment with lithium and valproate: reduction of lesion volume, attenuation of blood-brain barrier disruption, and improvement in motor coordination in mice with traumatic brain injury. *J. Neurosurg.* 119, 766–73 (2013).
 289. Lein, E. S. *et al.* Genome-wide atlas of gene expression in the adult mouse brain. *Nature* 445, 168–176 (2007).
 290. Schindelin, J. *et al.* Fiji: an open-source platform for biological-image analysis. *Nat. Methods* 9, 676–82 (2012).
 291. Yang, W. Y., Cao, W., Chung, T.-S. & Morris, J. *Applied Numerical Methods Using MATLAB®*. (John Wiley & Sons, Inc., 2005). doi:10.1002/0471705195
 292. Paxinos, G. & Watson, C. *The Mouse Brain in Stereotaxic Coordinates*. (Gulf Professional Publishing, 1998).
 293. Falkner, S. *et al.* Transplanted embryonic neurons integrate into adult neocortical circuits. *Nature* 539, 248–253 (2016).
 294. Motulsky, H. J. & Brown, R. E. Detecting outliers when fitting data with nonlinear regression - A new method based on robust nonlinear regression and the false discovery rate. *BMC Bioinformatics* 7, 123 (2006).
 295. Holtmaat, A. J. G. D. G. D. *et al.* Transient and persistent dendritic spines in the neocortex in vivo. *Neuron* 45, 279–291 (2005).
 296. Oswald, M. J., Tantirigama, M. L. S., Sonntag, I., Hughes, S. M. & Empson, R. M. Diversity of layer 5 projection neurons in the mouse motor cortex. *Front. Cell. Neurosci.* 7, 174 (2013).
 297. Wall, N. R., Wickersham, I. R., Cetin, A., De La Parra, M. & Callaway, E. M. Monosynaptic circuit tracing in vivo through Cre-dependent targeting and complementation of modified rabies virus. *Proc. Natl. Acad. Sci. U. S. A.* 107, 21848–53 (2010).
 298. Petreanu, L., Huber, D., Sobczyk, A. & Svoboda, K. Channelrhodopsin-2-assisted circuit mapping of long-range callosal projections. *Nat. Neurosci.* 10, 663–668 (2007).
 299. Mitchell, B. D. & Macklis, J. D. Large-scale maintenance of dual projections by callosal and frontal cortical projection neurons in adult mice. *J. Comp. Neurol.* 482, 17–32 (2005).
 300. Wahl, M. *et al.* Variability of homotopic and heterotopic callosal connectivity in partial agenesis of the corpus callosum: A 3T diffusion tensor imaging and Q-Ball tractography study. *Am. J. Neuroradiol.* 30, 282–289 (2009).
 301. Schüz, A., Chaimow, D., Liewald, D. & Dortenman, M. Quantitative aspects of corticocortical connections: a tracer study in the mouse. *Cereb. Cortex* 16, 1474–86 (2006).
 302. Ertürk, A. *et al.* Interfering with the chronic immune response rescues chronic degeneration after traumatic brain injury. *J. Neurosci.* 36, 9962–9975 (2016).
 303. Huang, S.-Y., Chang, C.-H., Hung, H.-Y., Lin, Y.-W. & Lee, E.-J. Neuroanatomical and electrophysiological recovery in the contralateral intact cortex following transient focal cerebral ischemia in rats. *Neurol. Res.* 40, 130–138 (2018).
 304. Takatsuru, Y., Koibuchi, N. & Nabekura, J. Unilateral infarction of the visual cortex (VC) induced an increase in dendritic spine turnover in contralateral VC. *Neurosci. Lett.* 488, 97–100 (2011).
 305. Johnston, D. G., Denizet, M., Mostany, R. & Portera-Cailliau, C. Chronic in vivo imaging shows no evidence of dendritic plasticity or functional remapping in the contralesional cortex after stroke. *Cereb. Cortex* 23, 751–762 (2013).
 306. Evanko, D. Windows on the brain. *Nat. Methods* 4, 474–474 (2007).
 307. Xu, H.-T., Pan, F., Yang, G. & Gan, W.-B. Choice of cranial window type for in vivo imaging affects dendritic spine turnover in the cortex. *Nat. Neurosci.* 10, 549–551 (2007).
 308. Sajo, M., Ellis-Davies, G. & Morishita, H. Lynx1 limits dendritic spine turnover in the adult visual cortex. *J. Neurosci.* 36, 9472–9478 (2016).

309. Alexander, B. H. *et al.* Stable density and dynamics of dendritic spines of cortical neurons across the estrous cycle while expressing differential levels of sensory-evoked plasticity. *Front. Mol. Neurosci.* 11, (2018).
310. Trachtenberg, J. T. *et al.* Long-term in vivo imaging of experience-dependent synaptic plasticity in adult cortex. *Nature* 420, 788–794 (2002).
311. Ma, L. *et al.* Experience-dependent plasticity of dendritic spines of layer 2/3 pyramidal neurons in the mouse cortex. *Dev. Neurobiol.* 76, 277–286 (2016).
312. Lee, S., Ueno, M. & Yamashita, T. Axonal remodeling for motor recovery after traumatic brain injury requires downregulation of γ -aminobutyric acid signaling. *Cell Death Dis.* 2, e133 (2011).
313. Schubert, V., Lebrecht, D. & Holtmaat, A. Peripheral deafferentation-driven functional somatosensory map shifts are associated with local, not large-scale dendritic structural plasticity. *J. Neurosci.* 33, (2013).
314. Zhang, S. *et al.* Whole-brain mapping of monosynaptic afferent inputs to cortical crh neurons. *Front. Neurosci.* 13, (2019).
315. Wall, N. R. *et al.* Brain-Wide Maps of Synaptic Input to Cortical Interneurons. *J. Neurosci.* 36, 4000–9 (2016).
316. DeNardo, L. A., Berns, D. S., DeLoach, K. & Luo, L. Connectivity of mouse somatosensory and prefrontal cortex examined with trans-synaptic tracing. *Nat. Neurosci.* 18, 1687–1697 (2015).
317. Douglas, R. J. & Martin, K. A. C. NEURONAL CIRCUITS OF THE NEOCORTEX. *Annu. Rev. Neurosci.* 27, 419–451 (2004).
318. Harris, K. D. & Shepherd, G. M. G. The neocortical circuit: themes and variations. *Nat. Neurosci.* 18, 170–181 (2015).
319. Rock, C. & Apicella, A. Callosal projections drive neuronal-specific responses in the mouse auditory cortex. *J. Neurosci.* 35, 6703–6713 (2015).
320. Carrasco, A. *et al.* Influence of core auditory cortical areas on acoustically evoked activity in contralateral primary auditory cortex. *J. Neurosci.* 33, 776–789 (2013).

- ACKNOWLEDGMENTS -

First and foremost I would like to express my great gratitude to my supervisor PD Dr. Florence Bareyre. Thank you for always being hopeful & helpful no matter what new direction the project took us, for being supportive, for providing valuable scientific advice and for giving me this opportunity to work in your lab and learn many things about the craft of research and myself.

Another big thank you goes to Prof. Dr. Martin Kerschensteiner and Prof. Dr. Thomas Misgeld for being a part of my TAC committee. Your scientific guidance and advice, as well as your positive outlook were extremely helpful and valued.

Moreover I would like to thank all my colleagues in both Florence and Martins lab (especially the two-photon gang that always stuck together and helped each other out on good and less optimal imaging days) for creating an enjoyable working environment. A special thank you goes to Delph for standing by me with moral support, as well as Minh Schumacher, Christoph Mahler and Giuseppe Locatelli for teaching me all the necessary techniques for in vivo two-photon imaging from the ground up and always providing technical/scientific support at any time of day or night. Your humour and wit while doing so, was more than greatly appreciated. In addition I want to specifically thank Maryam Chahin for being such a trooper and helping me image as well as analyze some of the final data of this thesis.

Furthermore I would like to extend my immense thanks to Alexandra Chovsepian. As a colleague, her tireless work and efforts were an indispensable part of this project and without her, it could not have been materialized the way it is now. Most importantly though an even bigger thank you goes to her as a friend and person, as well as to my other new found friends (4 laiiiiif): Almir, Carmen and Mehrnoosh. Without your positive spirit, our laughing flashes, talks and musical performances (I'm looking at you Alex) it wouldn't have been the same and I can't thank you enough for being there. I actually don't think words can describe how much your presence, you guys as people, your support, your scientific and life advice have meant to me during this time. Through thick and thin you were always there, and I am a happier, more knowledgeable and an all around better version of myself for it.

Last but most certainly not least, a gigantic and special chunk of gratitude goes out to my family, Mama, Papa, Max and Michael and my friends, Vicky and Kathi. Without your unconditional love and patience through the ups and downs, the way you could always somehow make me laugh/lift me up and your moral (and scientific) support I could not have done this! Same shout out to you, Margie! Aaand you, Mateja, #Teamsoupero :) Σας αγαπώ!

- LIST OF PUBLICATIONS -

Chovsepian A*, **Empl L***, Correa D and Bareyre FM (2017): Heterotopic transcallosal projections are present throughout the mouse cortex. *Front Cell Neurosci* 11:36. (* shared first authorship)

Klein C, Rasińska J, **Empl L**, Sparenberg M, Poshtiban A, Hain EG, Iggena D, Rivalan M, Winter Y, Steiner B (2016): Physical exercise counteracts MPTP-induced changes in neural precursor cell proliferation in the hippocampus and restores spatial learning but not memory performance in the water maze. *Behav Brain Res*, 307:227–238.

Klein C, Jonas W, Iggena D, **Empl L**, Rivalan M, Wiedmer P, Spranger J, Hellweg R, Winter Y, Steiner B (2016): Exercise prevents high-fat diet-induced impairment of flexible memory expression in the water maze and modulates adult hippocampal neurogenesis in mice. *Neurobiol Learn Mem* 131:26–35.

Ebinger M, Ipsen N, Leonards CO, **Empl L**, Hanne L, Liman T, Mai K, Straburger CJ, Spranger J, Endres M (2015): Circulating insulin-like growth factor binding protein-3 predicts one-year outcome after ischemic stroke. *Exp Clin Endocrinol Diabetes* 123:461–465.

Edemann-Callesen H, Voget M, **Empl L**, Vogel M, Wieske F, Rummel J, Heinz A, Mathé AA, Hadar R, Winter C (2015): Medial forebrain bundle deep brain stimulation has symptom-specific anti-depressant effects in rats and as opposed to ventromedial prefrontal cortex stimulation interacts with the reward system. *Brain Stimul* 8:714–723.

- EIDESTATTLICHE VERSICHERUNG/ AFFIDAVIT -

Hiermit versichere ich an Eides statt, dass ich die vorliegende Dissertation „Spine dynamics and circuit connectivity of transcallosal neurons in the intact contralesional cortex after traumatic brain injury“ selbstständig angefertigt habe, mich außer der angegebenen keiner weiteren Hilfsmittel bedient und alle Erkenntnisse, die aus dem Schrifttum ganz oder annähernd übernommen sind, als solche kenntlich gemacht und nach ihrer Herkunft unter Bezeichnung der Fundstelle einzeln nachgewiesen habe.

I hereby confirm that the dissertation „Spine dynamics and circuit connectivity of transcallosal neurons in the intact contralesional cortex after traumatic brain injury“ is the result of my own work and that I have only used sources or materials listed and specified in the dissertation.

München, den 14. April 2020

Munich, 14.04.2020

LAURA EMPL

.....

(Unterschrift/Signature)

- DECLARATION OF AUTHOR & RESULTS CONTRIBUTIONS -

Publication 1: Chovsepian A*, Empl L*, Correa D, and Bareyre FM: Heterotopic transcallosal Projections Are Present throughout the Mouse Cortex. *Front Cell Neurosci*; 11:36, (2017)

F. Bareyre conceived the study design, supervised work and contributed to writing the manuscript. A. Chovsepian and L. Empl contributed equally to this publication, performing surgical procedures, histological staining, imaging and analyzing data on TCN distribution. Both also revised the manuscript and contributed to figure design. They were helped by D. Correa, who performed clearing experiments (not shown in this thesis) and imaging of fixed tissue.

Unpublished content of thesis:

F. Bareyre conceived study design and supervised experiments.

L. Empl helped with conception of study design and performed all in vivo imaging experiments from surgery to analysis in GFP-M animals as well as in animals, where TCN were specifically labelled. For animals in which CST neurons were traced, L. Empl performed all surgical procedures and then assisted M. Chahin with imaging procedures. After thorough training by L. Empl, M. Chahin analyzed results of spine dynamics in CST neurons. Survival fraction and longevity of single spines was analyzed by F. Bareyre (CST neurons) and L. Empl (TCN). For experiments of circuit reconstruction using a mono-synaptic rabies virus tracing technique L. Empl and A. Chovsepian contributed equally in terms of surgical procedures. A. Chovsepian took over imaging of pre-synaptic cells, while L. Empl imaged all data for starter cells. S. Abdulsalaam helped with imaging of pre-synaptic cells and executed interpolation of starter cells. Data analysis presented in this thesis was performed by L. Empl. All illustrations in this thesis were made by L. Empl.

I hereby certify that all the information provided in this declaration of thesis contributions is true, factual and correct.

Munich, 14.04.2020

Laura Empl

Alexandra Chovsepian
(Co-first author)

Florence Bareyre
(Supervisor)